



저작자표시-비영리-동일조건변경허락 2.0 대한민국

이용자는 아래의 조건을 따르는 경우에 한하여 자유롭게

- 이 저작물을 복제, 배포, 전송, 전시, 공연 및 방송할 수 있습니다.
- 이차적 저작물을 작성할 수 있습니다.

다음과 같은 조건을 따라야 합니다:



저작자표시. 귀하는 원 저작자를 표시하여야 합니다.



비영리. 귀하는 이 저작물을 영리 목적으로 이용할 수 없습니다.



동일조건변경허락. 귀하가 이 저작물을 개작, 변형 또는 가공했을 경우에는, 이 저작물과 동일한 이용허락조건하에서만 배포할 수 있습니다.

- 귀하는, 이 저작물의 재이용이나 배포의 경우, 이 저작물에 적용된 이용허락조건을 명확하게 나타내어야 합니다.
- 저작권자로부터 별도의 허가를 받으면 이러한 조건들은 적용되지 않습니다.

저작권법에 따른 이용자의 권리는 위의 내용에 의하여 영향을 받지 않습니다.

이것은 [이용허락규약\(Legal Code\)](#)을 이해하기 쉽게 요약한 것입니다.

[Disclaimer](#)



공학박사학위논문

실속 조건에서 Synthetic Jet 능동 유동 제어에  
관한 실험적 연구

Experimental Study on Active Flow Control  
of Synthetic Jet in Stalled Condition

2014년 2월

서울대학교 대학원  
기계항공공학부  
이 병 현

## Abstract

This paper presents experimental investigations of the characteristics of synthetic jets with a circular exit array. The flow characteristics of piezoelectrically driven synthetic jets with a circular exit array were investigated under various flow conditions. Step-by-step experiments were conducted to find an improved configuration of a circular exit array while some parameters were held constant, in this case the oscillation frequency, input voltage, and exit area. Comparative studies were conducted to compare a quiescent condition, a forced separated flow, and separated flows over high angles of attack. For the quiescent condition, jet characteristics depending on the hole perimeter and oscillation frequency were compared by measuring velocity profiles by means of hot-wire anemometry. For the forced separated flow, pressure distributions on an inclined flat plate were examined while changing the parameters of the hole diameter, hole gap, type of synthetic jet array, and oscillation phase. Experimental results were then analyzed with a help of the computed vortical structures in the quiescent and forced separated-flow conditions. Based on the comparisons, a proper range of design parameters for an improved circular exit array was obtained, showing that the circular exit array based on the design parameters provided better performance in terms of separation control. For separated flows over an airfoil and a blended wing body configuration at high angles of attack, the flow control performance of the proposed synthetic jets was verified by measuring the aerodynamic coefficients. Based on various comparisons, synthetic jets with the improved circular exit array were found to be effective for control of the flow separation phenomenon.

---

**Keyword** : Synthetic jet, Active flow control, Circular exit array, Flow separation

**Student number** : 2011 – 30789

**Name** : Lee, Byunghyun

## Table of Contents

<b>ABSTRACT .....</b>	<b>I</b>
<b>TABLE OF CONTENTS .....</b>	<b>III</b>
<b>LIST OF FIGURES .....</b>	<b>VI</b>
<b>LIST OF TABLES.....</b>	<b>XI</b>
<b>NOMENCLATURE .....</b>	<b>XII</b>
<b>I. INTRODUCTION .....</b>	<b>1</b>
<b>    1.1 Literature Review .....</b>	<b>1</b>
1.1.1 Flow Separation.....	1
1.1.2 Flow Separation Control .....	2
1.1.3 Traditional Boundary Layer Control .....	3
1.1.4 Synthetic Jet .....	5
1.1.5 Piezoelectrically-driven Synthetic Jet.....	6
<b>    1.2 Research Motivation .....</b>	<b>7</b>
<b>    1.3 Objectives and Contribution .....</b>	<b>10</b>
1.3.1 Synthetic Jet Design .....	11
1.3.2 Key Design Parameters of a Circular Exit Array .....	11
1.3.3 Efficient Flow Control on a Leading-edge Stalled Airfoil.....	12
1.3.4 Efficient Flow Control on a Blended Wing Body .....	12
<b>    1.4 Organization of Thesis.....</b>	<b>13</b>

<b>II. EXPERIMENTAL SETUP .....</b>	<b>14</b>
<b>2.1 Hot-wire Anemometer .....</b>	<b>14</b>
<b>2.2 Low Speed Wind Tunnel.....</b>	<b>15</b>
<b>2.3 Data Acquisition System .....</b>	<b>16</b>
<b>2.4 Function Generator .....</b>	<b>17</b>
<b>2.5 Voltage Amplifier .....</b>	<b>18</b>
<b>2.6 Pressure Measurement .....</b>	<b>18</b>
<b>III. EXPERIMENTAL PROCEDURE .....</b>	<b>20</b>
<b>3.1 Quiescent Condition .....</b>	<b>20</b>
<b>3.2 Separated-flow condition.....</b>	<b>20</b>
3.2.1 Design Parameters of a Circular Exit Array .....	21
3.2.2 Effects of Synthetic Jet Array .....	22
3.2.3 Verification of Separation Control Capability on an Airfoil .....	23
3.2.4 Verification of Separation Control Capability on a Wing .....	25
<b>IV. RESULTS AND DISCUSSIONS.....</b>	<b>28</b>
<b>4.1. Synthetic Jet Design.....</b>	<b>28</b>
<b>4.2 Flow Characteristics in a Quiescent Condition .....</b>	<b>30</b>

<b>4.3 Flow Characteristics in a Separated-flow Condition .....</b>	<b>32</b>
4.3.1 Design Parameters of Circular Exit Array .....	32
4.3.2 Separation Control Capability on an Airfoil.....	39
4.3.3 Flow Characteristics on a 3-D wing configuration .....	47
<b>V. CONCLUDING REMARKS .....</b>	<b>59</b>
<b>5.1. Summary.....</b>	<b>59</b>
<b>5.2. Future Works .....</b>	<b>62</b>
<b>FIGURES .....</b>	<b>64</b>
<b>TABLES .....</b>	<b>144</b>
<b>국문초록 .....</b>	<b>154</b>

## List of Figures

**Fig. 1.1 Schematic view of laminar boundary layer separation at a curved surface [4]**

**Fig. 1.2 Interrelation between flow-control goals [5]**

**Fig. 1.3 Requirement for future aircraft**

**Fig. 1.4 Comparison with the existing slat application [26]**

**Fig. 1.5 Types of piezoelectric disk [8]**

**Fig. 1.6 Flow control strategy on a 2-D airfoil**

**Fig. 1.7 Flow control strategy on a 3-D wing**

**Fig. 2.1 Circuit diagram of CTA**

**Fig. 2.2 I-Type hot wire anemometer**

**Fig. 2.3 Subsonic wind tunnel at Seoul National University**

(test section of 200 mm × 200 mm × 1000 mm)

**Fig. 2.4 Subsonic wind tunnel at Seoul National University**

(test section of 1350 mm × 950 mm × 2440 mm)

**Fig. 2.5 Subsonic wind tunnel at Korea Aerospace Research Institute**

(test section of 4 m × 3 m)

**Fig. 2.6 Labview display (front panel)**

**Fig. 2.7 Labview display (block diagram)**

**Fig. 3.1 Data acquisition setup in the quiescent condition**

**Fig. 3.2 Data acquisition setup in the cross flow condition**

**Fig. 3.3 Inclined flat plate setup for the design parameters of circular exit array**

**Fig. 3.4 Inclined flat plate setup for the synthetic jet array and oscillation phase**

**Fig. 3.5 Computed results and synthetic jet location [64]**

- Fig. 3.6 NACA 64A210 airfoil test setup**
- Fig. 3.7 Schematic of NACA 64A210 airfoil model**
- Fig. 3.8 Methods for pressure data acquisition**
- Fig. 3.9 Computed results and synthetic jet location [64]**
- Fig. 3.10 Wind tunnel test setup of 3-D wing configuration**
- Fig. 3.11 Location of pressure taps of 3-D wing configuration**
- 
- Fig. 4.1 Synthetic jet performance test (exit type 1-1)**
- Fig. 4.2 Synthetic jet performance test (exit type 1-1)**
- Fig. 4.3 RMS jet velocity (exit types 1-1, 1-2, and 1-3)**
- Fig. 4.4 Viscous area of exit wall surface**
- Fig. 4.5 Effect of synthetic jet actuation ( $U_\infty = 10$  m/s,  $f = 120$  Hz)**
- Fig. 4.6 Aerodynamic forces depending on oscillation frequency ( $f = 50\text{-}300$  Hz )**
- Fig. 4.7 Lift coefficient on the rear plate (exit types 1-1, 1-2, and 1-3)**
- Fig. 4.8  $C_p$  distribution on the rear plate (exit types 2-1, 2-2, and 2-3)**
- Fig. 4.9 Validation of numerical simulation [64]**
- Fig. 4.10 Result of numerical simulation (synthetic jet-off) [64]**
- Fig. 4.11 Result of numerical simulation ( $G = 0.75$  mm,  $D=1.5$  mm) [64]**
- Fig. 4.12 Result of numerical simulation ( $G = 1.5$  mm,  $D=1.5$  mm) [64]**
- Fig. 4.13 Result of numerical simulation ( $G = 3$  mm,  $D=1.5$  mm) [64]**
- Fig. 4.14 Phase-averaged vorticity magnitude contours at jet exit and vortex formation schematics (Exit type 2-1 with  $G = 0.75$  mm and  $D=1.5$ mm) [64]**
- Fig. 4.15 Phase-averaged vorticity magnitude contours at jet exit and vortex formation schematics (Exit type 2-2 with  $G = 1.5$  mm and  $D=1.5$ mm) [64]**
- Fig. 4.16 Phase-averaged vorticity magnitude contours at jet exit and vortex formation schematics (Exit type 2-3 with  $G = 3$  mm,  $D=1.5$ mm ) [64]**
- Fig. 4.17 Jet velocity in the quiescent condition (exit type 2-2 and 3)**
- Fig. 4.18  $C_p$  distribution on the rear plate (exit types 2-2 and 3)**

- Fig. 4.19**  $C_p$  distribution on the rear plate (1<sup>st</sup> single array,  $x = 8$  mm)
- Fig. 4.20**  $C_p$  distribution on the rear plate (2<sup>nd</sup> single array,  $x = 21$  mm)
- Fig. 4.21**  $C_p$  distribution on the rear plate (2<sup>nd</sup> single array,  $x = 50$  mm)
- Fig. 4.22**  $C_p$  distribution on the rear plate (dual array, 13 mm gap)
- Fig. 4.23**  $C_p$  distribution on the rear plate (dual array, 42 mm gap)
- Fig. 4.24** Slopes of  $C_p$  curves (m)
- Fig. 4.25** Mean  $C_p$  on the upper surface of NACA 64A210 (synthetic jet-off)
- Fig. 4.26**  $C_p$  distribution near the leading-edge of NACA64A210 ( $\alpha = 12$  degrees,  $Re\# = 6.67 \times 10^5$ )
- Fig. 4.27** Standard deviation of  $C_p$  on the upper surface of NACA 64A210 (synthetic jet-off)
- Fig. 4.28** Wake survey of NACA 64A210 (synthetic jet-off)
- Fig. 4.29** Lift coefficient curve of NACA 64A210 (synthetic jet-off) [84]
- Fig. 4.30** Effects of oscillation frequency ( $Re\# = 6.67 \times 10^5$ , 1<sup>st</sup> array actuation)
- Fig. 4.31** Effects of oscillation frequency ( $Re\# = 6.67 \times 10^5$ , 1<sup>st</sup> array actuation)
- Fig. 4.32** Increment of lift according to the angle of attack (1<sup>st</sup> array actuation)
- Fig. 4.33** Wake region depending on oscillation frequency (1<sup>st</sup> array actuation)
- Fig. 4.34** Wake region depending on oscillation frequency (1<sup>st</sup> array actuation)
- Fig. 4.35** Increment of lift-to-drag ratio depending on the angle of attack (1<sup>st</sup> array actuation)
- Fig. 4.36** Lift coefficient depending on array type ( $Re\# = 6.67 \times 10^5, f = 120$  Hz)
- Fig. 4.37** Lift increment depending on array type ( $Re\# = 6.67 \times 10^5, f = 120$  Hz)
- Fig. 4.38**  $C_p$  distribution depending on array type ( $Re\# = 6.67 \times 10^5, f = 120$  Hz)
- Fig. 4.39**  $C_p$  distribution depending on array type ( $Re\# = 6.67 \times 10^5, f = 120$  Hz)
- Fig. 4.40** Drag polar curve of NACA 64A210 ( $f = 120$  Hz)
- Fig. 4.41** Tuft visualization of flow separation control ( $\alpha = 12$  degrees,  $Re\# = 6.67 \times 10^5, f = 120$  Hz)
- Fig. 4.42** Schematic of closed-loop control
- Fig. 4.43** Pressure gradient according to AOA (synthetic jet-off)

- Fig. 4.44 Pressure gradient according to frequency (synthetic jet-on)**
- Fig. 4.45 Flow structure on a delta wing**
- Fig. 4.46 spatial location of the vortex core and the vortex breakdown location**
- Fig. 4.47 Lift coefficient curve of 3-D wing**
- Fig. 4.48 Drag coefficient curve of 3-D wing**
- Fig. 4.49 Lift-to-drag ratio curve of 3-D wing**
- Fig. 4.50 Tufts visualization ( $\alpha = 8$  degrees)**
- Fig. 4.51 Tufts visualization ( $\alpha = 10$  degrees)**
- Fig. 4.52 Tufts visualization ( $\alpha = 12$  degrees)**
- Fig. 4.53 Spanwise  $C_p$  distribution (1<sup>st</sup> line)**
- Fig. 4.54 Spanwise  $C_p$  distribution (2<sup>nd</sup> line)**
- Fig. 4.55 Spanwise  $C_p$  distribution (3<sup>rd</sup> line)**
- Fig. 4.56 Spanwise  $C_p$  distribution across a delta wing [89]**
- Fig. 4.57 Chordwise  $C_p$  distribution on the blended wing body (1<sup>st</sup> – 4<sup>th</sup> line)**
- Fig. 4.58 Chordwise  $C_p$  distribution on the blended wing body (5<sup>st</sup> – 8<sup>th</sup> line)**
- Fig. 4.59 Tuft visualization of flow separation control ( $\alpha = 12$  degrees,  $Re\# = 1.59 \times 10^6$ ,  $f = 200$  Hz)**
- Fig. 4.60 Increment of  $C_l$  and decrement of  $C_d$  in the stall regime**
- Fig. 4.61 Comparison of  $C_l/C_d$  curve and increment of  $C_l/C_d$**
- Fig. 4.62 Qualitative effect of synthetic jet ( $\alpha = 10$  degrees)**
- Fig. 4.63 Spanwise  $C_p$  distribution ( $\alpha = 10$  degrees)**
- Fig. 4.64 Chordwise  $C_p$  distribution ( $\alpha = 10$  degrees)**
- Fig. 4.65 Qualitative effect of synthetic jet ( $\alpha = 12$  degrees)**
- Fig. 4.66 Spanwise  $C_p$  distribution ( $\alpha = 12$  degrees)**
- Fig. 4.67 Chordwise  $C_p$  distribution ( $\alpha = 12$  degrees)**
- Fig. 4.68 Total increment of  $C_l/C_d$**
- Fig. 4.69 Increment of  $C_l/C_d$  per module**
- Fig. 4.70 Spanwise  $C_p$  distribution ( $\alpha = 10$  degrees)**
- Fig. 4.71 Chordwise  $C_p$  distribution ( $\alpha = 10$  degrees)**

**Fig. 4.72 Spanwise  $C_p$  distribution ( $\alpha = 12$  degrees)**

**Fig. 4.73 Chordwise  $C_p$  distribution ( $\alpha = 12$  degrees)**

**Fig. 4.74 Baseline flow field and synthetic jet location ( $\alpha = 10$  degrees)**

**Fig. 4.75 Baseline flow field and synthetic jet location ( $\alpha = 12$  degrees)**

**Fig. 4.76 Possible future research topics**

## **List of Tables**

**Table 3.1 Exit configuration and diaphragm actuation mode**

**Table 3.2 Types of synthetic jet array**

**Table 3.3 Types of synthetic jet oscillation**

**Table 4.1 Quantitative comparison of flow control performance**

## Nomenclature

$\alpha$	= angle of attack
$C_d$	= sectional drag coefficient estimated from wake velocity deficit
$C_l$	= sectional lift coefficient estimated from airfoil surface pressure distribution
$C_p$	= pressure coefficient ( $\Delta P / (1/2 \rho_\infty U_\infty^2)$ )
$C_\mu$	= momentum coefficient by the jet velocity ( $(\rho_\infty \bar{u}_j^2 h) / (1/2 \rho_\infty U_\infty^2 L)$ )
$c$	= chord length
$D$	= hole diameter
$f$	= oscillation frequency of diaphragm
$F^+$	= reduced frequency ( $f L / U_\infty$ )
$G$	= hole gap
$h$	= slot width (hole diameter)
$L$	= characteristic length (chord length)
$m$	= slope of pressure coefficient distribution ( $(C_p - \text{constant}) / \ln(x/L)$ )
$\Delta P$	= difference between measured pressure and reference pressure
$\Delta C_l$	= percentage of lift coefficient increase ( $((C_{l \text{ jet-off}} - C_{l \text{ jet-on}}) / C_{l \text{ jet-off}}) \times 100$ )
$\Delta C_l/C_d$	= percentage of lift-to-drag ratio increase $((C_l/C_{d \text{ jet-off}} - C_l/C_{d \text{ jet-on}}) / (C_l/C_{d \text{ jet-off}}) \times 100)$
$Re^\#$	= Reynolds number
$U_\infty$	= freestream velocity

$\overline{u_j}$	= root mean square velocity of the issuing synthetic jet ( $\sqrt{\overline{u_j^2}}$ )
$V_{pp}$	= positive peak voltage and negative peak voltage
$x$	= chordwise distance from the leading-edge
$y$	= spanwise distance from center line
$z$	= normal distance from wall
$\rho_\infty$	= freestream density

# I. Introduction

## 1.1 Literature Review

### 1.1.1 Flow Separation

Flow separation is almost always associated with losses of some kind, including loss of lift, drag increase, pressure losses, etc. Flow separation is generally accepted to be the breakaway or detachment of fluid from a solid space [1, 2]. Fluid particles in the boundary layer are slowed down by wall friction as well as adverse pressure gradient. If the external potential flow is sufficiently slowed down due to the presence of adverse pressure gradient, the momentum of those particles will be consumed by both the wall shear and the pressure gradient [3]. A schematic view of the area where the boundary layer separates is depicted in Fig. 1.1, showing the effect of the adverse pressure gradient on the velocity profiles [4]. The velocity gradient is zero at the separation point. This implies that there is no skin friction. While downstream of it there is a rapidly growing region of reverse flow into the dead air region. The boundary layer transforms into a wake at the edge of the separated region. Flow separation and reattachment process are highly sensitive to Reynolds number, pressure gradient, and flow disturbance [5]. Transition and separation play a critical role in determining the development of the boundary layer on the airfoil which affects the overall performance of the air vehicles [6, 7]. Aforementioned separation phenomena can be found in the flow past aircraft parts. The shape of major aircraft components (fuselage, wing empennage, nacelles) is usually chosen so that in most flight conditions the adverse pressure gradient is gradual, the flow

separates in a thin dead air region or wake and the associated drag is small [4]. In the development of aircraft, one of leading concerns is the desire to obtain better performance for air vehicles. It has been reported that flow control can lead to saving millions of dollars in fuel costs each year by making an aircraft more efficient [8].

### **1.1.2 Flow Separation Control**

Of all the various types of shear flow control now extent, control of flow separation, historically referred to as boundary-layer control (BLC), is probably the oldest and most economically important [5]. Generally it is desired to postpone separation so that form drag is reduced, stall is delayed, lift is enhanced, and pressure recovery is improved. However, in some instances it may be beneficial to provoke separation. For example, to improve the subsonic high-lift performance of an airfoil optimized for supersonic flight, a flap may be used to initiate leading-edge separation followed by reattachment [9]. Figure 1.2 represents the main objectives of flow control. If the boundary layer around the wing becomes turbulent, its resistance to flow separation is enhanced and more lift can be obtained at increased incidence [10]. On the other hand, the skin friction drag for a laminar boundary layer can be as much as an order of magnitude less than that for a turbulent one. If transition is delayed, lower skin friction as well as lower flow-induced noise is achieved. However, the laminar boundary layer can only support very small adverse pressure gradient without separation, and subsequent loss of lift and increase in form drag occur [11]. Once the laminar boundary layer separates, a free-shear layer forms, and for moderate Reynolds numbers transition to turbulence takes place. Increased

entrainment of high-speed fluid due to the turbulent mixing may result in reattachment of the separated region and formation of a laminar separation bubble [12]. At higher incidence, the bubble breaks down, either separating completely or forming a longer bubble. In either case, the form drag increases, and the lift-curve's slope decreases. The ultimate goal of all this is to improve the airfoil's performance by increasing the lift-to-drag ratio. However, induced drag is caused by the lift generated on a lifting surface with a finite span. Moreover, more lift is generated at higher incidence, but form drag also increases at these angles [5].

### **1.1.3 Traditional Boundary Layer Control**

Prandtl [13] introduced the concept of the boundary layer phenomena and proposed how to control its attachment to a solid surface, such as suction through a slot. The next ten years saw little progress in boundary layer research [14], but the race for air superiority, spawned universal research and development efforts in which BLC studies were given high priority. The importance of international research up to the early 1960s is apparent from the two volumes edited by Lanchmann [15], which provided exhaustive treatment of theoretical, experimental application of BLC methods. The contributions indicated that steady blowing or suction from various locations on the wing surface, and on various configurations, could produce significant lift increment as well as drag reductions. Boundary layer control, as a means of preventing separation, has traditionally been associated with the injection of fluid to, or the removal of a fluid from, a boundary layer; or the motion of a surface in the general direction of stream [16]. Historically,

suction is viewed as the first method ever proposed for the control of separation. The basic principle of flow separation control is to remove decelerated fluid near a surface and deflect the high-momentum free-stream fluid towards the surface. The remarkable effects of suction were demonstrated on a variety of wind tunnel models as well as experimental aircrafts. But, this suction method has not been applied to the wings or control surfaces of aircraft. Due to the mechanical complexity and additional weight, any aerodynamic gains made by suction are offset by the power required to operate the suction device [17]. On the other hand, the main principle of steady blowing is to directly impart additional momentum to retarded fluid within the boundary near the surface and thus delay flow separation [18]. Blowing is usually achieved by an auxiliary blower or compressor bleed, but can also be achieved passively by diverting fluid from the freestream to the surface [19]. Steady blowing has been investigated for a variety of different locations on wings, but the most successful application was observed in the case of the shoulder of a deflected flap [20]. While there has been some progress toward identifying suitable actuator concepts for application on commercial transport aircraft, there is still considerable uncertainty as to the nature of the systems architectures that are needed to support the generation, management and distribution of power to these actuators [21]. In particular, the choice between distributing power electrically or pneumatically is still an open question, despite significant historical development of boundary layer control techniques using compressed air [22] and progress towards the development of the more electric aircraft [23]. In other words, existing high-lift generation system does not satisfy the strict design requirements for a higher-efficiency

and higher-performance aircraft, as shown in Fig. 1.3. Until now, the direction of a fluid jet has mainly been controlled by mechanical devices which alter a jet flow to a desired direction. For example, aircraft engines often use mechanical protrusions which are disposed in jet exhaust in order to eject the flow out of the exhaust nozzle. These mechanical protrusions used to drive a flow, which are usually require complex and powerful actuators to move them [24]. Recently, promising approaches of separation control using synthetic jets have received a great attention. Among the flow control devices, synthetic jet has become one of the most actively studied subjects, because it has a potential to be implemented in actual flow control system [25]. As shown in Fig. 1.4, recent research indicates that it is possible to realistically design a synthetic jet flow control system within the aircraft performance limits [26].

#### **1.1.4 Synthetic Jet**

Synthetic jets periodically transport momentum flux from a jet exit to an outside region to enhance mixing with external flow field [27]. With the ability to control separated-flow regions with less energy consumption, synthetic jets have been regarded as a promising method for increasing aerodynamic performances of future aircrafts. Synthetic jets have been studied by both experimental and numerical methods. Flow control by oscillation was firstly proposed by Schubauer and Skramstad [28]. They introduced periodic perturbations into a laminar boundary layer to trigger flow instability. Seifert *et al.* [29] demonstrated that airfoil stall can be delayed by an oscillatory blowing

jet. Glezer [30] studied the dimensionless parameters that determine the jet vortex structure using LDV (Laser Doppler Velocimetry) system. Amitay and Cannelle [31] studied the evolution and transitory behavior of finite span synthetic jets using hot-wire anemometry and PIV (Particle Image Velocimetry) system. Subsequently, more detailed studies have been carried out for applications. Kim and Kim [25] numerically investigated the frequency-dependent flow control mechanisms of synthetic jets on an airfoil, and proposed multi-location synthetic jets to mitigate the unstable flow structures of a high-frequency jet. Kim *et al.* [32] demonstrated that flow control using synthetic jets improves the aerodynamic performance of tilt-rotor UAV (Unmanned-Aerial-Vehicle) airfoils under various flight conditions.

### **1.1.5 Piezoelectrically-driven Synthetic Jet**

Example applications have shown that many types of synthetic jet can control the separated-region include airfoil and bluff bodies [33, 34]. The oscillating diaphragm used in the synthetic jet cavity is usually driven by using electrical or mechanical power. When driven with AC (Alternating Current) signal, piezoelectric disks oscillate in the same manner as a piston or a shaker, and they also require the reduced number of moving parts which are prone to failure [8]. Because of these advantages, several investigators have adopted piezoelectric disks in synthetic jets to attempt to make the systems lighter, increase efficiency and save resource [35-38]. Although, these piezoelectric disks have been

successful in generating high velocities capable of altering the flow fields, the devices operate at high frequencies, consequently requiring high amounts of power [8]. In this study, piezoelectric diaphragm is used as active membrane in the jet cavity. These composites have the ability to produce microscale displacement and provide a wide bandwidth response as well as being lightweight. Such advantages make them suitable for flow control purposes, as demonstrated by Mossi *et al.* [39-41]. Aforementioned studies provide a chief characteristics of a piezoelectric-diaphragm actuator, but a detailed description for the practical application of a this type of actuator is not available. Researchers have been found several drive types of piezoelectric component, which can be applied to a practical synthetic jet actuator, as shown in Fig. 1.5. Thus, several types of piezoelectric diaphragms were selected as candidates, and suitable one was appraised by means of synthetic jet performance tests. More detailed result on the synthetic jet design is discussed in Chap. IV-4-1.

## 1.2 Research Motivation

The previous studies up to now have revealed many interesting flow characteristics of synthetic jets, and showed the potential of synthetic jets for improving aerodynamic performance [42, 43]. At the same time, however, detailed flow characteristics for a strategy of flow separation control have not been fully understood and several issues are still being studied. Exit configuration, oscillation phase, and jet injection location are reported as critical

problem among the unsolved issues.

The exit configuration of synthetic jets strongly affects the vortex development process at exit, which, in turn, determines the net momentum transfer to external flow field [44]. Thus, the dependence of jet performance on the jet exit configuration is a key parameter for jet performance. Until recently, most studies on the jet exit configuration have focused on the rectangular slot, which is relatively easy to install. However, studies on the rectangular slot exit revealed insufficient jet velocity at mid-span at high aspect ratio [45]. To overcome this weakness, some researchers studied other exit configurations. Oren *et al.* [46] investigated the flow characteristics of various exit configurations using PIV system, such as a circular, a square, and an equilateral triangle configuration. Among these configurations, a circular hole turned out to be advantageous in generating high turbulence at jet exit, but the effective area of a single circular hole is not large enough to control a widely separated-flow region. Kim *et al.* [44] demonstrated that a sufficient jet momentum can be produced by a circular exit array, using less power than the rectangular slot, indicating that the circular exit array is an efficient way to control the widely separated-flow region. The gap between orifices was studied by Riazi and Ahmed [47], who suggested that a minimum distance between adjacent holes is required to maintain the circulation of each hole. At the same time, type of oscillations for airfoil separation control was also studied. Seifert *et al.* [29, 48] found that three-dimensional oscillation can yield a beneficial interaction

between adjacent actuators. Holl *et al.* [49] numerically studied the flow characteristics of two-segmented slots. It was observed that the phase shift of two-segmented slots can increase fluid mixing along the spanwise direction. From these perspectives, the circular exit array configuration and the three-dimensional oscillation of synthetic jets are promising for flow separation control. The proper location of jet injection for separation control is known to be at or close to the separation point. Studies of various airfoils report that  $x/c < 10\%$  is an effective location for flow separation control [1, 50]. However, three-dimensional boundary layers are more common in practical flow condition than two-dimensional ones. The point of boundary-layer separation from a three-dimensional body does not necessarily coincide with the point of vanishing wall shear [5]. A necessary condition for the occurrence of flow separation is the convergence of skin-friction lines onto a particular line [51]. Thus, the proper location of synthetic jet-on a wing is more complicated than that of airfoil.

In this paper, further investigations are carried out to identify the key design parameters determining the performance of the synthetic jet with a circular exit array. The flow characteristics of piezoelectrically driven synthetic jets with a circular exit array are studied under various flow conditions. To find an improved flow control strategy, step-by-step experimental studies were conducted. Firstly, synthetic jet actuators were investigated by hot-wire measurement under a quiescent condition. Comparative studies were performed according to the design parameters, such as hole diameter, hole gap, and

oscillation frequency. Experimental results were examined with computational result of fellow researcher, which indicates the jet characteristics under a quiescent condition. Secondly, the flow control capability was compared under a forced separated-flow condition. Pressure distributions on an inclined flat plate were investigated according to the design parameters, such as hole diameter, hole gap, type of synthetic jet array, and oscillation phase. Two types of inclined flat plates were used depending on the design parameters. Experimental results were also compared with the computational result of fellow researcher, which indicates the jet characteristics under a separated-flow condition. Thirdly, the improved design parameters of synthetic jets were applied to flow separation control on NACA 64A210 airfoil. The flow control capability of synthetic jets for separated flows at a high angle of attack was then verified by measuring aerodynamic coefficients, such as surface pressure coefficient, lift coefficient, and drag coefficient. Finally, the improved design parameters of synthetic jets were applied to flow separation control on a blended wing body configuration. For the practical flow condition of three-dimensional boundary layers, the flow control capability of synthetic jets at a high angle of attack was verified by measuring pressure distribution and separated-flow region on the wing surface.

### **1.3 Objectives and Contribution**

The objective of this paper is to develop the improved flow control strategy of synthetic jets with a circular exit array. More enhanced flow control techniques

not covered by aforementioned studies were applied to a stalled condition. The main contribution of this paper is summarized as follows.

### **1.3.1 Synthetic Jet Design**

Piezoelectrically driven synthetic jet, besides being lightweight, has the ability to produce microscale displacement and provide a wide bandwidth response. However, a detailed description for the practical application of this type of actuator is not available. To make flow control device smaller, lighter, and more efficient, synthetic jet design process was performed. Through jet performance test in both quiescent and separated-flow condition, appropriate synthetic jet actuator was designed to apply predetermined platform. As a result, manufactured synthetic jet demonstrates efficient flow control capability on the platform in a stalled condition.

### **1.3.2 Key Design Parameters of a Circular Exit Array**

Aforementioned study [44] demonstrated that a sufficient jet momentum can be produced by a circular exit array, using less power than the rectangular slot, indicating that the circular exit array is an efficient way to control the widely separated-flow region. However, detailed design parameters of circular exit array have yet been reported. In this paper, key design parameters determining the performance of the circular exit array under various flow conditions are studied in detail. As a result, hole diameter and hole gap are found to be key design parameters for flow control performance.

### **1.3.3 Efficient Flow Control on a Leading-edge Stalled Airfoil**

The main purpose of flow control on two-dimensional airfoil is to delay flow separation on the leading-edge, as shown in Fig. 1.6. In order to delay separated-flow, the location of jet oscillation should be properly designed at or close to the separation point. A decrease of the separated-flow area is identified by the recovery of chordwise  $C_p$  slope. Though previous studies [1,5,6] have shown the potential feasibility of synthetic jet, flow control on a massive separated-flow is still a challenging task. Flow control effectiveness of synthetic jet was often verified at small  $\alpha$  [52]. In addition, synthetic jet is mostly installed at trailing-edge or aileron to assist conventional control surface [53]. In this paper, the leading-edge stall of an airfoil is targeted to demonstrate the flow control capability. Massive flow separation is effectively suppressed by using compact synthetic jet actuator at the leading-edge. As a result, aerodynamic performance of leading-edge stalled airfoil is greatly improved.

### **1.3.4 Efficient Flow Control on a Blended Wing Body**

The main purpose of flow control on blended wing body is to suppress suction peak and to delay separated-flow on the wing, as shown in Fig. 1.7. In order to achieve these purposes, the location of jet oscillation should be properly designed. However, the point of boundary-layer separation from a three-dimensional body does not necessarily coincide with the point of vanishing wall shear stress. For these reasons, the proper location of synthetic jet-on a wing is

more complicated than that of airfoil. Delay of leading-edge vortex breakdown can be captured by suppression of spanwise suction peak. A decrease of the separated-flow area is identified by the recovery of chordwise  $C_p$  slope. As already mentioned, flow control by synthetic jet-on a massive separated-flow is still a challenging task. Moreover, proven cases of flow control performance on the three-dimensional wing are still rather rare and in demand for a future aircraft design. Among considerations for aerodynamically efficient platform, blended wing body configuration demonstrated an advanced concept of future aircraft [54]. However, its flow characteristics are known to be more complicated than that of a conventional wing. If the aircraft is unstable and dependent upon active flight control, the secondary power required may be prohibitive [55]. In this paper, efficient and effective flow control technique on a blended wing body configuration is studied. As a result, selective-actuator-on technique according to vortex breakdown point on blended wing body is found to be more effective and efficient than those of traditional control method.

## **1.4 Organization of Thesis**

This paper is organized as follows. The experimental setups are presented in Section II. Section III explains the detailed experimental procedure depending on each research purpose. Section IV covers the experimental result under various flow conditions and the analysis on the flow characteristics. Finally, the concluding remarks are given in Section V.

## **II. Experimental Setup**

### **2.1 Hot-wire Anemometer**

Hot-wire anemometer was used to measure jet velocity of synthetic jet actuator in a quiescent condition. The hot-wire is a fine wire with very small diameter attached between two supporting needles on the probe, and is made of platinum or tungsten [56]. Hot-wire anemometer is often called CTA (constant temperature anemometer). CTA works on the basis of convective heat transfer from a heated sensor to the surrounding fluid, the heat transfer being primarily related to the fluid velocity. Main principle of CTA is shown in Fig. 2.1. Calibration establishes a relation between the CTA output and the flow velocity. It is performed by exposing the probe to a set of known velocities ( $U$ ), and then records the voltages ( $E$ ). A curve fit through the points  $(E,U)$  represents the transfer function to be used when converting data records from voltages into velocities. Calibration may either be carried out in a dedicated probe calibrator, which normally is a free jet, or in a wind-tunnel with for example a pitot-static tube as the velocity reference [57]. In subsonic flows where the density is high and the flow temperature is low and constant, the problem of heat transfer through the supporting needle and radiation effects can be ignored, and the hot-wire's response is basically a function of velocity alone [56]. Under these conditions, mean and turbulent (fluctuating) velocities are usually obtained by King's Law.

The equation is as follows.

$$E^2 = A + BU^n \quad (2.1)$$

Where E is voltage of CTA, U is a fluid velocity, and A, B, and n are constants.

In this paper, the oscillating velocity of synthetic jet was acquired by using the hot-wire (see Fig. 2.2), which is a single normal type with 5  $\mu\text{m}$  tungsten under a constant temperature mode. The CTA model is KANOMAX 1011 series. A static calibration based on King's Law was carried out by placing the hot-wire in the freestream of the wind tunnel. In order to maintain the accuracy of hot-wire, the calibration has been performed in every experiment. Hot-wire probe was placed onto the 3-axis auto traverse system with 0.1 mm accuracy in order to move measurement position. The maximum error of hot-wire was less than 5% over the range of the considered velocity. Obtained velocity data were recalculated by the mean, the RMS (root mean square), the maximum, and the minimum value by using Labview software.

## 2.2 Low Speed Wind Tunnel

Flow control experiments were conducted in low speed wind tunnel in Wind Tunnel Laboratory of Seoul National University and Korea Aerospace Research Institute. Wind tunnel types were adopted according to the experimental purposes. As shown in Fig. 2.3, the inclined flat plate experiments for improved circular exit array were conducted using a subsonic wind tunnel with a test section of 200 mm  $\times$  200 mm  $\times$  1000 mm at the Wind Tunnel Laboratory of

Seoul National University. The velocity variations were within 1 %, and the turbulence intensity was less than 1 %. Freestream velocity was measured by a pitot tube linked with a differential pressure transducer (MKS Instruments). The pitot tube was installed on the ceiling of the test section in front of the model. Freestream velocity was 10 m/s. As shown in Fig. 2.4, flow control experiments for the effect of synthetic jet array, oscillation phase, and NACA 64A210 airfoil were conducted by using the subsonic wind tunnel with a test section of 1350 mm × 950 mm × 2440 mm at the Wind Tunnel Laboratory of Seoul National University. The velocity variation was within 1 %, and the turbulence intensity was less than 1 %. End plates were installed on both sides of the inclined flat plate to maintain a two-dimensional condition. Pitot tube was installed on the ceiling of the test section in front of the model. Freestream velocity was 20 m/s and 30 m/s. Finally, as shown in Fig. 2.5, experiments on the three-dimensional wing were conducted by using the subsonic wind tunnel with a test section of 4 m × 3 m at the Korea Aerospace Research Institute. The turbulence intensity was less than 0.1 %. Freestream velocity was 20 m/s.

### **2.3 Data Acquisition System**

The data acquisition system used for this study is based on National Instrument system. All processes of controlling output signal are performed by Labview software as shown in Figs. 2.6 and 2.7. The DAQ (Data Acquisition Board) is NI USB-6251, which is connected to IBM PC for acquiring physical

data by using Labview software (National Instruments Inc.). The NI USB-6251 board has 16 analog inputs with 16-bit, 2 output channels, 24 digital I/O, and high speed sampling rates with 1.25 mega-samples per second [58]. The NI USB-6251 board having high sample rate is used for measuring jet velocity, free stream velocity, static pressures and controlling the Net scanner 9116. NI USB-6251 board was linked to BNC-2120 connecting the physical output signal lines.

## **2.4 Function Generator**

Function generators used for this study are two types. One is the stand-alone type (DDS function generator, 9205 series), and the other is a PC-based type (NI myDAQ Device). The DDS (direct digital synthesis) function generator is used for the synthetic jet performance test in the quiescent condition. The DDS function generator has the high performance indexes and numerous function characteristics which are necessary for the fast completion of measuring. The simple and clear front panel design and the display interface of number and indicator light are convenient for the users to operate and observe [59]. NI myDAQ device is used for the flow control experiment in the cross-flow condition. Aerodynamic data in cross-flow condition are ultimately used for the closed-loop system, which is to operate the flow control system autonomously using actuators, sensors, and a feedback controller. Therefore, the function generator in the cross-flow experiments should be connected with PC, which determines the onset of flow separation. The NI myDAQ platform includes a

data acquisition engine that users can use to measure two differential analog input and analog output channels (200 kS/s, 16 bits,  $\pm 10$  V). NI myDAQ supplies enough power for simple circuits and sensors with +5 V, +15 V, and -15 V power supply outputs (up to 500 mW of power) [60].

## 2.5 Voltage Amplifier

Voltage amplifier for this study is the E-481 high-power piezoelectric amplifier/controller [61], which is specifically designed for dynamic operation of high-capacitance piezoelectric actuators. The E-481 is based on a novel design combining pulse width modulation and energy recovery. Instead of dissipating the reactive power in heat sinks, this energy is temporarily stored in inductive elements. Only the active power used by the piezoelectric actuator has to be delivered. The energy not used by the actuator is returned to the amplifier and reused as supply voltage via a step-up transforming process. A peak sink and source current of up to 2000 mA is possible.

## 2.6 Pressure Measurement

The static pressure was measured through the static pressure taps distributed over the wind tunnel model surface. The 9116 net scanner with the 16 output channels [62] is used for the flow control experiment in Seoul National University. The 9116 can sample using up to three concurrent scan lists at continuous rates up to 500 measurements per channel per second in engineering

units. Pressure data in engineering units is output through an auto-negotiating 10 or 100 Mbit Ethernet interface supporting both TCP (transmission control protocol) and UDP (user datagram protocol). The DTC (digital temperature compensation) Initium with the 64 output channels [63] is used for the flow control experiment in Korea Aerospace Research Institute. This system integrates an advanced analog circuit design with the DTC technology to maintain optimal accuracy without requiring online span calibration of the pressure scanners. The DTC Initium supports software and hardware triggering of data sets, data packet ID stamping for time correlation, and data throughput to the host computer at rates as high as 1200 Hz per channel in engineering units.

### **III. Experimental Procedure**

#### **3.1 Quiescent Condition**

Synthetic jet performance test was conducted in a quiescent condition, as shown in Fig. 3.1. The jet velocity issued from the exit was measured by an I-type single hot-wire. A single hot-wire anemometry with a 5  $\mu\text{m}$  tungsten wire (KANOMAX model 1011) was used in the constant temperature mode. A static calibration of the hot-wire was carried out by placing a probe in the freestream of subsonic wind tunnel. The relation between voltage and velocity was calculated based on the King's law. The instrumental uncertainty in velocity measurement was found to be less than 0.2 m/s. Taking into account that the jet velocity oscillates, all velocity data were time-averaged with a period of over 30s. A hot-wire probe was installed on an autotraverse system with an accuracy of 0.1 mm. The hot-wire was set at a minimum height of 3 mm from the central point of the exit hole to prevent the suction effect near the exit. The I-type hot-wire was then used for measurements only during the blowing phase due to the directional ambiguity.

#### **3.2 Separated-flow condition**

Figure 3.2 shows the overall experimental setup in the separated-flow condition. Several wind tunnel setups were adopted for each experimental purpose.

### **3.2.1 Design Parameters of a Circular Exit Array**

In order to study an improved exit configuration of synthetic jets, comparative experiments were conducted under a forced separated flow. The separation location usually moves back and forth depending on the flow condition. A two-dimensional inclined flat plate was selected to simplify the separated-flow condition. Figure 3.3 shows the setup of the inclined flat plate for a wind tunnel test. An inclined flat plate made of acrylic material was assembled to create a separated-flow region on the rear plate. The plate angle and the freestream velocity were determined by numerical computations [64]. The rear plate is 150 mm long and 200 mm wide. The incidence angle of the rear plate to create a separated-flow at the leading-edge of the rear plate is 20 degrees. A single synthetic jet module was then installed near the starting point of flow separation. Due to the thickness of the synthetic jet module, the synthetic jet exit is located at about 8 mm from the leading-edge of the rear plate. Table 3.1 presents the exit configuration types for the purpose of the experiment. Exit types 1-1, 1-2, and 1-3 were used to investigate the effect of the hole (or orifice) diameter under the same exit area condition. Exit types 2-1, 2-2, and 2-3 were used to investigate the effect of the hole gap under the same exit area and hole diameter condition. Exit type 3 was used to verify a sufficient flow control area along the spanwise direction after determining the ratio of the hole diameter (D) to the hole gap (G). Static pressure taps were installed along the center of the rear plate. Static pressure was then obtained using a net pressure scanner (Pressure Systems).

Experiments were conducted using a subsonic wind tunnel with a test section of 200 mm × 200 mm × 1000 mm at the Wind Tunnel Laboratory of Seoul National University. The velocity variations were within 1 %, and the turbulence intensity was less than 1 %. The freestream velocity was measured by a pitot tube linked with a differential pressure transducer (MKS Instruments). The pitot tube was installed on the ceiling of the test section in front of the model. The freestream velocity was 10 m/s. Real-time pressure data were acquired by a 16-bit-A/D board and were processed by Labview 8.5 software. All pressure data (100 samples per second) were time-averaged with a period exceeding 30s.

### **3.2.2 Effects of Synthetic Jet Array**

Comparative experiments were conducted again under a forced separated-flow to investigate an improved array of synthetic jets. Figure 3.4 shows a typical wind tunnel test setup. The test setup is similar to that of the previous experiment, except for the plate size and the wind tunnel type. An inclined flat plate made of acrylic material was installed to create a separated-flow region on the rear plate. Like the previous experiment, the inclined angle of each plate and the freestream velocity were determined by detailed numerical computations [64]. The rear plate is 400 mm long and 400 mm wide, and the incidence angle is 22 degrees. Table 3.2 shows two types of synthetic jet arrays (single- and dual-array types) with different locations and array gaps. Each array is operated by three jet actuators. As in the single-array synthetic jet in Section III-2-1, the first array is located about 8 mm

from the leading-edge of the rear plate, and the second array jet modules are installed 13 mm and 42 mm behind the first array to examine the effect of multi-location synthetic jets [25]. As will be explained in Section IV-4-3, the performance of exit type 3 was better than that of exit type 1 or 2. Therefore, this type was used in all experiments for the study of the jet array. In addition, employing the jet oscillation types shown in Table 3.3, an experiment on the three-dimensional effect (or the effect of the oscillation phase) was conducted. All actuators were operated with the same voltage amplitude ( $V_{pp} = \pm 180$  V) but the oscillation phase was changed. Static pressure taps were installed along the plate center as shown in Fig. 3.4, and spanwise pressure taps were located at 60 mm and 260 mm from the leading-edge of the rear plate. Experiments were then conducted using a subsonic wind tunnel with a test section of 1350 mm  $\times$  950 mm  $\times$  2440 mm at the Wind Tunnel Laboratory of Seoul National University. The velocity variation was within 1 %, and the turbulence intensity was less than 1 %. End plates were installed on both sides of the inclined flat plate to maintain a two-dimensional condition. A pitot tube was installed on the ceiling of the test section in front of the model. The freestream velocity was 20 m/s. Other data acquisition instruments were identical to those of the previous experimental condition.

### **3.2.3 Verification of Separation Control Capability on an Airfoil**

Through experiments on a forced separated-flow with an inclined flat plate, optimized design parameters were obtained and the effect of the oscillation phase

along the spanwise direction was identified. Based on these results, experiments were conducted on an airfoil at a high angle of attack to verify the flow control capability of the improved exit configuration and the synthetic jet array. The leading-edge stall of an airfoil was targeted to demonstrate the flow control capability. According to previous research on the NACA 64A210 airfoil, flow separation is suddenly initiated near the leading-edge at the stall angle, and it evolves on the downstream side as the angle of attack increases [65, 66]. The proper location of jet oscillation for separation control is known to be at or close to the separation point. Studies of various airfoils report that  $x/c < 10\%$  is an effective location for flow separation control [1, 50]. Extensive numerical computations were carried out by a well-validated flow solver [25, 67] to predict the separation point accurately. Based on the computed results of baseline condition (Fig. 3.5) [64], the location of the synthetic jets was determined. Figure 3.6 shows the wind tunnel setup using a NACA 64A210 airfoil with a 500 mm chord and 500 mm span. A detailed schematic of the experimental model is shown in Fig. 3.7. Two arrays of synthetic jet modules were installed near the leading-edge to control leading-edge separation [68]. The first array of synthetic jets was located very close to the leading-edge ( $x/c = 0.004$ ), and the second array was located 48 mm behind the leading-edge, reflecting the experimental result of the inclined flat plate. Each jet array was operated by six actuators. Based on the performance tests in Sections III-2-1 and III-2-2, exit type 3 in Table 3.1 and oscillation type 3 in Table 3.3 were chosen. Static pressure taps were located along the upper surface of the airfoil, and

spanwise pressure taps were located 149 mm and 325 mm from the leading-edge. Based on the measured surface pressure distribution, the sectional lift coefficient was calculated. A wake survey experiment was conducted to identify changes in the drag according to the flow control. As shown in Fig. 3.8, a wake survey system was used to measure the velocity deficit from the total pressure difference. Each probe was connected to a net pressure scanner (Pressure Systems). The wake survey was done along the mid-span location at  $x/c = 1$  from the trailing edge, and the sectional drag coefficient was calculated from the velocity deficit. The oscillation frequency range and actuation waveform were determined from the experimental results obtained from the inclined flat plate. Experiments with the NACA 64A210 airfoil were conducted using the same subsonic wind tunnel with a test section of 1350 mm  $\times$  950 mm  $\times$  2440 mm at the Wind Tunnel Laboratory of Seoul National University. End plates were installed on both sides of the airfoil to maintain a two-dimensional flow condition, and a stepper motor system was installed to change the angle of attack. The freestream velocities were 20 m/s and 30 m/s. Other data acquisition instruments were identical to those used in the previous experiments.

### **3.2.4 Verification of Separation Control Capability on a Wing**

Through experiments on a separated-flow with NACA 64A210 airfoil, the effect of the synthetic jet array and oscillation phase along the spanwise direction were identified. As already mentioned earlier, three-dimensional boundary layers

are more common in practical flow condition than two-dimensional ones and the point of boundary-layer separation from a three-dimensional body does not necessarily coincide with the point of vanishing wall shear stress. For these reasons, the proper location of synthetic jet-on a wing is more complicated than that of airfoil. Thus, extensive numerical computations were carried out by a well-validated flow solver [25, 67] to predict the separation point accurately. Based on the computed results of baseline condition (Fig. 3.9) [69], the location of the synthetic jets was determined. In order to verify the flow control capability of the synthetic jet, comparative experiments were conducted in a stalled condition. Figure 3.10 shows the wind tunnel setup using the blended wing body model with a 1.184 m chord and 2 m span. Synthetic jet actuators (7 modules on each wing) were installed to prevent leading-edge stall at high angles of attack. All actuators were operated with the same voltage amplitude ( $V_{pp} = \pm 180$  V) and oscillation frequency ( $f = 200$  Hz). Static pressure tap arrays were located along the upper surface on the wing. The experiments were then conducted in a subsonic wind tunnel that had a test section of  $4\text{ m} \times 3\text{ m}$  at the KARI (Korea Aerospace Research Institute). The turbulence intensity was less than 0.1 %. And the freestream velocity was 20 m/s. Because the pressure field surrounding the vortex is a key factor in the occurrence of breakdown [70]. Static pressure taps were installed on the different wing sections with the forces and moments acquired via an external six-component balance. Since flow fluctuations were in separated regions, all pressure data (4 samples per second) were time-averaged

over a period of 10 seconds. The strong suction effect on the top surface created by leading-edge vortices were analyzed by experimental data, like pressure distribution along the spanwise direction and lift coefficient, as shown in Fig. 3.11.

## IV. Results and Discussions

### 4.1. Synthetic Jet Design

The characteristics of a synthetic jet are usually determined by a few dimensionless parameters related to the periodic jet velocity. Among several parameters, the jet momentum coefficient and the reduced frequency are considered as the most critical parameters in relation to control of the flow. The jet momentum coefficient is defined as follows [1],

$$c_\mu = \frac{\rho_\infty \overline{u_j^2} h}{1/2 \rho_\infty U_\infty^2 L} \quad (4.1)$$

and the reduced frequency is given by

$$F^+ = \frac{f L}{U_\infty} \quad (4.2)$$

Here,  $h$  is the slot width (or hole diameter),  $L$  is the characteristic length (or chord length),  $U_\infty$  is the freestream velocity, and  $\overline{u_j}$  is the RMS (root mean square) jet velocity. The optimal range of the jet momentum coefficient is not narrowly specified, as it depends on many factors, such as the flow conditions, characteristic length of the experimental model, the actuator type, and other factors [56]. Greenblatt and Wygnanski [1] reported that the optimal range of jet momentum coefficients was approximately  $0.01 \% \leq c_\mu \leq 3 \%$ . The optimal range of the

reduced frequency was identified as  $0.3 \leq F^+ \leq 4.0$  for separation control over an airfoil [71-73]. These results were used as a guideline for a baseline design of the proposed synthetic jets.

A schematic of piezoelectrically driven actuators is shown in Fig. 4.1. Jet momentum is produced by the volume change of a cavity by two piezoelectric diaphragms, as shown in Fig. 4.1. The manufactured synthetic jet module is presented in Fig. 4.1b. The basic outer components consist of acrylic parts, and the piezoelectric diaphragm is installed on both sides of the cavity. The outer acrylic components are fixed by screws and nuts to allow an easy change of the exit configuration. The piezoelectric diaphragm used in this actuator is made of a thin material. Its displacement is very small and its operating condition is greatly influenced by the range of the oscillating frequency. To overcome this drawback and to increase the volume change in the cavity, some researchers have investigated a dual-diaphragm actuator [74]. Several studies provide a brief schematic of a dual-diaphragm actuator, but a detailed description for the practical application of a this type of actuator is not available. Several types of piezoelectric diaphragms were selected as candidates [8], and the bimorph-type piezoelectric disk manufactured by Piezo Systems was chosen based on performance tests. A piezoceramic material is coated onto the two layers of a circular metal plate whose diameter is 63.5 mm, as shown in Fig. 4.1c. The maximum free deflection of the disk is reported as  $\pm 476 \mu\text{m}$  when the disk is vibrated at its resonance frequency. Performance tests with changes of the input voltage were conducted to determine a

suitable range of input voltage. Experiments showed that the diaphragm displacement became larger as the input voltage increased. Considering that voltage amplitude greater than  $V_{pp} = \pm 200$  V caused cracks on the surface of the piezoceramic material,  $V_{pp} = \pm 180$  V was determined as the input voltage amplitude. The mechanical response of the diaphragm according to the input waveform can be found in the literature. Though a sawtooth waveform is reported to produce a higher peak velocity than the sinusoidal type [8], the durability to maintain the peak velocity is strictly limited. For this reason, a sinusoidal waveform was chosen.

## 4.2 Flow Characteristics in a Quiescent Condition

Figure 4.2a demonstrates the relationship between the input voltage and the velocity profile, confirming that the jet velocity profile follows a sinusoidal waveform. Figure 4.2b shows the time-averaged jet velocity according to the number of piezoelectric diaphragms. Both single and dual diaphragms were activated, and laser displacement sensors (LB-70 series) were used to measure the deflection of each diaphragm. At the same voltage, the diaphragm deflection grew as the oscillation frequency increased. A greater amount of deflection induced a higher volume change in the cavity. As the oscillation frequency (and thus the volume change) increased, the peak velocity at the exit became high. This trend continued until the frequency was close to the resonant frequency. The maximum allowable frequency of the piezoelectric disk was found to  $f = 300$  Hz. On the other

hand, the RMS jet velocity became nearly stagnant after  $f = 200$  Hz because the duration of the peak velocity decreased substantially. Considering the structural safety of the piezoelectric diaphragm and the jet momentum flux, the adequate frequency range of the synthetic jet was about  $f = 50 \sim 200$  Hz. Figure 4.2b also compares the jet velocity depending on the diaphragm type. The jet velocity was higher in the dual diaphragm, as reported in the literature; thus, the dual diaphragm was adopted for all experiments.

Figure 4.3 shows the RMS jet velocities of exit types 1-1 ( $D = 1$  mm), 1-2 ( $D = 1.5$  mm), and 1-3 ( $D = 2$  mm), measured at a height of  $z = 3$  mm. The frequency-dependent behavior of the jet velocity is somewhat similar to that shown in Fig. 4.2b. In particular, the jet velocity of exit type 1-3 is higher than that of the others over the entire frequency range. As shown in Table 3.1, all of the exit configurations have the same cross-sectional area and orifice depth. The viscous area of the jet exit wall, which is shown in Fig. 4.4, is proportional to the total hole perimeter. Exit type 1-3 has the smallest perimeter among the three types; therefore, its RMS jet velocity is higher than the others. At the same time, however, the effective area covered by the vortex ring produced from the jet shrinks as the perimeter of the jet exit decreases (or as the RMS velocity increases). Because the vortex ring plays an important role in enhancing the degrees of mixing [75-77], both the jet momentum (or the RMS velocity) and the effective area of the vortex ring (or the hole perimeter) should be taken into account simultaneously. For this perspective, the effects of the RMS velocity and the hole perimeter are discussed

again in a separated-flow condition.

### 4.3 Flow Characteristics in a Separated-flow Condition

#### 4.3.1 Design Parameters of Circular Exit Array

##### 4.3.1.1 Effect of hole diameter and oscillation frequency

The flow characteristics of each exit configuration in a fully separated condition were investigated to examine the flow control effect depending on the exit configuration. A simple tuft visualization process was utilized for the rear plate surface, and the pressure coefficient ( $C_p$ ) was obtained by a net scanner. Figure 4.5 shows the flow control effect of the synthetic jets. The images at the top represent the real-time  $C_p$  distribution in a Labview screen. The two images at the bottom show the flow direction according to the tufts. When the synthetic jet is off, a large dead-air region with oppositely directed tufts is created by flow separation. The  $C_p$  distribution is flat over the entire rear plate, indicating a large dead-air region on the rear plate. When the synthetic jet is on, the tufts maintain the freestream direction, and the  $C_p$  slope along the chordwise direction confirms a substantial degree of pressure recovery. Judging from the  $C_p$  distribution and the tuft directions, the synthetic jet with a circular exit array satisfies the required flow control capabilities.

The flow control capability depending on the oscillation frequency was investigated by comparing the  $C_p$  distributions. Figure 4.6a shows the time-averaged  $C_p$  distributions on the rear plate. This experiment was performed under

the same exit type condition (exit type 1-1 of Table 3.1). The  $C_p$  slope indicates the pressure recovery level on the rear plate. The higher the slope of the pressure coefficient curve is, the more the rear plate recovers the pressure gradient. Figure 4.6b shows the lift coefficient obtained by integrating the  $C_p$  distribution on the rear plate. Good control performance was obtained with  $f = 50 \sim 150$  Hz. An appropriate range of the jet parameters relies on the following values:  $0.75 \leq F^+ \leq 2.25$  and  $0.110 \% \leq C_\mu \leq 0.543 \%$ , which are consistent with the results in Ref. 1.

Based on the experimental observation in the quiescent condition, comparative experiments were conducted to find an adequate hole diameter that yields better flow control performance. As a flow control index, the lift coefficient ( $C_l$ ) by exit types 1-1, 1-2, and 1-3 in Table 3.1 are compared in Fig. 4.7. The lift coefficient was obtained by numerically integrating the  $C_p$  distribution on the rear plate when  $f = 50$  Hz at 100 Hz. Exit type 1-3 ( $D = 2$  mm), which has the smallest hole perimeter, produced the highest RMS velocity in the quiescent condition (see Fig. 4.3). As mentioned previously, this indicates that it provides the largest jet momentum but that the effective area covered by the vortex ring is the smallest. On the other hand, exit type 1-1 ( $D = 1$  mm), which has the lowest RMS velocity and the largest hole perimeter, provides the smallest jet momentum and the largest effective area of the vortex ring. For the purpose of better flow control, the jet momentum should be higher and the effective area of the vortex ring should be larger. From this perspective, exit type 1-2 ( $D = 1.5$  mm) is a reasonable trade-off. Indeed, exit type 1-2 yields the highest lift coefficient, as shown in Fig. 4.7.

#### **4.3.1.2 Effect of hole gap**

With exit type 1-2, the effect of the hole gap was investigated. Exit types 2-1, 2-2, and 2-3 of Table 3.1 were considered. The  $C_p$  distributions on the plate at  $f = 50$  Hz and 100 Hz are shown in Fig. 4.8. Exit type 2-2 with  $G, D = 1.5$  mm provided the highest  $C_p$  slope, indicating that  $G = 1.5$  mm (or the ratio of  $D$  to  $G = 1$ ) is adequate. In order to understand the associated flow field, a computational result analysis was carried out by fellow researcher [64] and the vortex structures produced by exit types 2-1, 2-2, and 2-3 were examined. In this case, 3-D unsteady Reynolds-averaged Navier-Stokes (URANS) computations were performed with an in-house code, which was extensively validated by Kim *et al.* [25, 67, 78]. The governing equations were solved in a time-accurate manner by the method of pseudo-compressibility. For the convective term, a third-order accurate upwind differencing scheme based on the flux-difference splitting and MUSCL approach was used. The viscous flux was centrally differenced by the second-order spatial accuracy, and the flow variables were updated by the LU-SGS time integration scheme. The effect of turbulence was taken into account by the Menter's shear stress transport two-equation model. Also, the jet boundary condition proposed by Kral *et al.* [79] was adopted. Numerical results were validated by comparing the  $C_p$  distributions along the downstream direction of the slot center. With exit type 2-3, a grid refinement study was carried out by employing three grid densities. From the comparison of the computed results depicted in Fig. 4.9a, the difference between the fine and the medium mesh is less than 2%, which is adequate for reliable and

efficient computations. Thus, a medium mesh system of 6.4 million grid points was adopted. As shown in Fig. 4.9b, the computed results show reasonable agreement with experimental data for exit types 2-1, 2-2, and 2-3.

Figure 4.10-13 represents the computed results of each exit configuration under the forced separated-flow condition [64]. The pictures on the left represent the iso-vorticity contours, which compare the persistency of the vortical structure depending on the hole gap. For exit types 2-1 and 2-2, the vortical structure from the jet exit is well preserved along the downstream (Figs. 4.11a and 4.12a). However, the jet vortex of exit type 2-3 is mixed with the freestream, and the vortex structure is quickly diffused along the downstream (Fig. 4.13a). The images on the right show the velocity magnitude contour. The separated-flow region is the blue-colored area, indicating that the streamwise velocity magnitude is nearly zero. When the synthetic jet is off, a large dead-air region by flow separation is observed (Fig. 4.10b). When the synthetic jet is on, the dead-air region on the rear plate is substantially eliminated and the flow is attached onto the plate surface (Figs. 4.11b-4.13b). However, the degrees of flow control performance depends on the hole gap. For exit type 2-1 and exit type 2-2 (Figs. 4.11b and 4.12b), the separated-flow region existing at the end of the plate is relatively small. For exit type 2-3 (Fig. 4.13b), the separated-flow region is somewhat larger. Considering the persistence of the jet vortex and the size of the separated-flow region, exit type 2-1 and exit type 2-2 are better than exit type 2-3.

To examine the interaction between adjacent holes, the phase-averaged vorticity

magnitude contours at each jet exit are compared. The images in Figs. 4.14a-4.16a represent a cross-sectional view of the vorticity magnitude. The strength of the jet vortex is displayed from red to green. The images in Figs. 4.14b-4.16b indicate a simple schematic of the vortex interaction between adjacent holes depending on the hole gap. For exit type 2-1, the vortices generated from each hole actively interact near the hole gap, and a jet vortex with a high strength is observed (Fig. 4.14a). Afterwards, counter-rotating vortices in the mixed area cancel each other out to produce weaker vortices, as shown in Fig. 4.14a. For exit type 2-3, there is no noticeable interaction between two adjacent vortices and thus the initial vortex is largely unchanged (Fig. 4.16a). Exit type 2-2 was found to be a reasonable trade-off in terms of the strength and sustainability of the jet vortex (Fig. 4.15a). Thus, exit type 2-2 (or the case with a  $D/G = 1$ ) is an adequate choice for flow control.

From Figs. 4.10-4.16, we observe that the vortex ring generated by the jet exit needs to be maintained longer for effective flow control. Moreover, more vortex rings are necessary to provide a sufficient flow control area along the spanwise direction. From this perspective, Fig. 4.17 compares exit type 2-2 and exit type 3 to examine the maximum allowable number of exit holes for each jet module. With the synthetic jet module shown in Fig. 4.1b, exit type 3 has the maximum number of exit holes (14 holes), while the ratio of D to G is identical to that shown in exit type 2-2. As expected, both the peak jet velocity and the RMS jet velocity decrease slightly as the number of exit holes increases, as shown in Fig. 4.17. However, the net flow control capability of exit type 3 is better than that of exit type 2-2 because

it provides more vortices for mixing, as shown in Fig. 4.18. Thus, exit type 3 is finally adopted to study the effect of the synthetic jet array and the oscillation phase.

#### **4.3.1.3 Effect of synthetic jet array and oscillation phase difference**

Inclined flat-plate experiments were performed under a fully separated-flow to examine the effects of the synthetic jet array type and an oscillation phase on the flow control capability. The range of the oscillation frequency was  $f = 50 \sim 200$  Hz, and exit type 3 in Table 3.1 was adopted for this experiment. Figure 4.19 shows the time-averaged  $C_p$  distributions on the rear plate using the first single array of actuators (array type 1 in Table 3.2). The slope of the  $C_p$  curve, as an index of the flow control capability, changes according to the oscillation frequency and phase difference. For the in-phase condition, a frequency range of  $f = 120 \sim 140$  Hz is good for control. For a case with a 180-degrees phase difference along the spanwise direction, a frequency range for good performance is  $f = 120 \sim 190$  Hz. This result indicates that the phase difference widens the available frequency range for better flow control. It has been also reported that the phase shift of two-segmented slots can increase the separation control capability by enhancing fluid mixing along the spanwise direction [49, 75, 77, 80, 81]. As shown in Fig. 4.20 and 4.21, the second single array of actuators (array types 2 and 3 in Table 3.2) did not have any visible effect over the entire frequency range regardless of the oscillation phase difference. These results show again the significance of the synthetic jet

location for separation control. As reported in earlier work, the proper location of the synthetic jet is crucial for flow control, and it should be close to the separation point to deliver the jet momentum at the region where the separation bubble begins to grow.

A multi-location synthetic jet was found to be effective as a means of providing more stable flows on a suction surface [25, 82]. Flow control experiments with dual arrays were performed to examine the effect of multiple locations along the chordwise direction. One is the minimum gap (the second single array is 21 mm behind the separation point) due to the thickness of the synthetic jet module, and the other is a 42mm gap (the second single array is 50 mm behind the separation point). Figure 4.23 shows the time-averaged  $C_p$  distributions on the rear plate using a dual array of actuators (array type 5 in Table 3.2). As shown in Fig. 4.22, the  $C_p$  distribution does not improve regardless of the frequency range and phase difference with a 13 mm gap array. The multi-location synthetic jet with the 13 mm gap array is far less efficient than the first single array shown in Fig. 4.19. For the multi-location synthetic jet with the 42 mm gap array (Fig. 4.23), the  $C_p$  distribution is much more improved. This indicates that the flow control capability can be greatly improved by properly controlling the distance between the synthetic jet arrays. The performance of dual-array synthetic jets is examined again in airfoil experiments in Section IV-3-2.

In an effort to understand the flow control capability quantitatively, the slope of the  $C_p$  curve ( $m$ ) on the rear plate is compared, as shown in Fig. 4.24.

Regressions of all  $C_p$  curves were performed using a power equation. The  $x$ -axis is the normalized value of the momentum coefficient ( $C_\mu$ ) and the  $y$ -axis is the  $C_p$  slope ( $m$ ) distribution. The table on the right side explains the oscillation phase, and high-performance cases are highlighted. The pressure recovery slope is adopted as an index of flow control. A higher  $C_p$  slope means a higher pressure recovery. Comparing the curves in Fig. 4.24, the single-array actuator with a 180-degrees phase difference represents the best performance throughout the range of actuating frequencies. In addition, the dual-array actuators with a proper choice of array distance demonstrate stable performance over most frequencies regardless of the phase difference. Thus, the first single array of actuators (type 1 in Table 3.2), the dual-array actuator (type 5 in Table 3.2), and a 180-degrees phase difference (type 3 in Table 3.3) were finally adopted to verify the separation control capability on a stalled airfoil.

### **4.3.2 Separation Control Capability on an Airfoil**

#### **4.3.2.1 Synthetic jet-off**

Before verifying the flow control performance of the synthetic jets with improved design parameters on the NACA 64A210 airfoil, basic flow characteristics were undertaken by changing the angle of attack. The purpose of experiments in this chapter is to investigate the stall characteristics of NACA 64A210 and the proper location of synthetic jets. As already mentioned, the proper location of jet oscillation for separation control is known to be at or close to the

separation point. Thus, synthetic jet location for separation control was predicted by the result of computational analysis [83], as stated in Chapter IV-3-2-3. Baseline aerodynamic data were measured under the condition of a smooth airfoil surface. In other words, all synthetic jet exits were closed to avoid turbulence induced by the hole array configuration.

Figure 4.25 presents the mean  $C_p$  distributions on the airfoil upper surface according to the angle of attack. When  $\alpha = 12 \sim 13$  degrees, a constant pressure region starts to appear near the leading-edge, implying that a separation bubble begins to grow over the stall angle [4, 84]. A higher angle of attack makes the region of separation bubble larger, leading to a flat  $C_p$  distribution along the chord. The time traces of  $C_p$  near the leading-edge are analyzed to examine the separation bubble in detail when the airfoil stall starts ( $\alpha = 12$  degrees). In Fig. 4.26b, the irregular pattern of  $C_p$  indicates that a laminar-turbulent transition is immediately initiated near the stagnation point. When the transition process is complete, the downstream flow becomes fully turbulent and the regular wave pattern disappears [16]. The flow on the upper surface becomes fully turbulent after the stall angle ( $\alpha = 12$  degrees). Figure 4.27 represents the standard deviation of  $C_p$  on the upper surface according to the angle of attack. The standard deviation of  $C_p$  becomes suddenly larger when the stall angle is imminent, indicating that the flow becomes unstable before the separation bubble starts to grow near the leading-edge. The wake velocity survey was performed at a location of  $x/c = 1$  downstream of the trailing edge. As shown in Fig. 4.28, the wake region is narrow before the stall

angle but it suddenly increases after the stall angle. Figure 4.29 shows the lift coefficient curve. Experimental data were calculated by integrating the  $C_p$  distribution over the airfoil surface and the wake velocity deficit. Figure 4.29 also shows the comparison of computed aerodynamic coefficients with experimental data [83]. To examine the grid sensitivity, three grid densities ( $405 \times 121$ ,  $305 \times 118$ , and  $195 \times 114$ ) were considered for the uncontrolled cases. From the comparison of the computed results depicted in Fig. 4.29, the differences between  $405 \times 121$  and  $305 \times 118$  are less than 2%, which is thought to be adequate for reliable computations. The computed results agree fairly well with the experimental data except near the region of stall. However, the general behavior near the post-stall region is captured accurately, which is enough to understand the main physics of flow separation. Judging from the lift behavior across the stall angle [85, 86], the flows over NACA 64A210 show the characteristics of the leading-edge stall.

#### **4.3.2.2 Synthetic jet-on**

In order to control the leading-edge stall on the NACA 64A210 airfoil, a strategy for flow separation control was established. Experiments for flow separation control were conducted by applying the design parameters obtained from previous experiments. These were the oscillation frequency, exit configuration, phase difference, and jet array type. The range of the oscillation frequency was  $f = 50 \sim 200$  Hz. Exit type 3 with a 180 degrees phase difference in Tables 3.1 and 3.3 was adopted, and the first single array and the dual array were

selectively operated. All flow control experiments in the stall regime were carried out in a turbulent boundary-layer state, as shown in Fig. 4.26. Flow control characteristics according to the design parameters of synthetic jets were compared with the baseline data in Section IV-3-2-1.

Figure 4.30 and 4.31 shows the  $C_p$  distributions along the chordwise direction when the first single array of synthetic jets operates (see Fig. 4). Figures 4.30a and 4.31a are cases when  $\alpha = 12$  degrees, which is the case for which the airfoil stall begins. Figures 4.30b and 4.31b are the results for  $\alpha = 20$  degrees, which is a fully separated condition. The mean  $C_p$  indicates the overall quantity of flow control and the standard deviation of  $C_p$  refers to the level of flow fluctuation (or flow stability). As shown in Figs. 4.30, a higher oscillation frequency yields more pressure recovery at the leading-edge. However, if the oscillation frequency increases,  $C_p$  fluctuation likewise increases, as shown in Fig. 4.31. Greater  $C_p$  fluctuation is unfavorable in terms of flow control stability. Thus, it is noted that a proper range of the oscillation frequency is  $f = 100 \sim 200$  Hz, which provides sufficient jet momentum and flow stability for control of the leading-edge stall.

When the 1<sup>st</sup> single-array of synthetic jets operates, the flow control performance according to the oscillation frequency and Reynolds number are shown in Figs. 4.32~4.35. Aerodynamic performance is compared in terms of the increment of  $C_l$  (Fig. 4.32), the change in the wake region (Fig. 4.33 and 4.34), and the variation of the lift-to-drag ratio (Fig. 4.35). As shown in Figs. 4.32 and 4.33, the flow control performance at both Reynolds numbers is substantially improved

at the high oscillation frequency. Comparing to the control-off case in Fig. 4.28, the wake region is narrow below the stall angle, but it increases drastically above the stall angle. For the case of  $\alpha = 12$  degrees (Figs. 4.33a and 4.34a), the velocity deficit is small and the wake region is narrow, so the control effect is also small. In the case of  $\alpha = 20$  degrees (Figs. 4.33b and 4.34b), the velocity deficit is large and the wake region is wide; thus, the control effect is more apparent than that of  $\alpha = 12$  degrees. These results are similar to the trend of the lift curve according to the angle of attack. Drag force is obtained from the integration of the wake velocity profile, and the lift-to-drag ratio is increased by 10 ~ 70 % above the stall angle, as shown in Fig. 4.35. This confirms that synthetic jet is effective above the stall angle by reducing massive flow separation.

Comparative studies were performed to investigate the effect of the synthetic jet array type along the chordwise direction. The effect of the synthetic jet array was examined by comparing the  $C_l$  curve (Fig. 4.36), the increment of lift (Fig. 4.37), and the  $C_p$  distribution (Figs. 4.38 and 4.49). As shown in Figs. 4.36 and 4.37, the synthetic jet-only for the case of the second single-array actuation is not effective. This is associated with the location of the synthetic jet exit. It is well known that a synthetic jet close to a flow separation point is effective for flow control [2, 23]. The second single-array synthetic jet is far behind the separation point; thus, when it is actuated, it acts as a source of roughness near the leading-edge, having a negative effect on the  $C_l$  curve.

For dual-array actuation, the aerodynamic performances overall are similar to

those of the first single-array actuation. The benefits of dual-array actuation can be found in terms of the stability of the flow. Figures 4.38 and 4.39 show the  $C_p$  distribution according to the synthetic jet array type. In terms of the mean  $C_p$  distribution, both the first single array and the dual array show similar flow control performance levels, as shown in Figs. 4.38a and 4.38b. However, the dual array is more favorable for reducing flow fluctuation near the leading-edge at high angles of attack, as shown in Fig. 4.39b. This indicates that multi-location synthetic jets have a beneficial effect of mitigating the unstable flow structure of a high-frequency jet. Both the improvement in the aerodynamic coefficient ( $C_l$  and  $C_d$ ) and the stability of the flow fluctuation (standard deviation of  $C_p$ ) are important for flow separation control. Thus, the first single-array actuation and the dual-array actuation should be operated selectively by reflecting the flow states according to the angle of attack.

Figure 4.40 shows the drag polar of the NACA 64A210 airfoil when  $f = 120$  Hz. Though not presented here, the results for other frequencies show a similar trend in terms of the aerodynamic performance. By operating the synthetic jets above the stall angle, the drag polar curve is favorably shifted. These results confirm, together with all of the preceding comparisons, that the synthetic jet system with enhanced design parameters is an effective method for controlling separated-flow regions. Figure 4.41 demonstrates the flow control effect of the synthetic jets in a separated-flow region. Tufts are installed on the upper surface along the streamwise direction. Referring to the baseline data in Fig. 4.25, a separation bubble near the leading-

edge arises after the stall angle ( $\alpha = 12$  degrees). When the synthetic jet is off, tufts in the separation region vibrate randomly and their direction is opposite to the freestream direction. When synthetic jet is on, the flow becomes attached noticeably because the dead-air region near the leading-edge is eliminated. As a result, the tufts follow the streamwise direction. These results confirm again that the synthetic jets with the improved circular exit array perform effectively when used to control the separated region of the NACA 64A210 airfoil.

#### **4.3.2.3 Flow separation parameter for closed-loop control**

Based on aerodynamic data in Chapter IV-3-2-1 and IV-3-2-2, a strategy for flow separation control on the airfoil was established. To investigate the performance of closed-loop control more clearly, the 1<sup>st</sup> single array jet was operated for the flow control. The angles of attack were  $\alpha = 12$  degrees, which is the angle of attack when the airfoil stall starts, and  $\alpha = 20$  degrees, which is the fully separated condition. The range of oscillation frequency was  $f = 100\text{-}200$  Hz. The closed-loop control objective is to operate the flow control system autonomously using actuators, sensors, and a feedback controller, as shown Fig. 4.42. The control strategy is based on the flow separation state on the upper surface. When the flow separation is detected by separation parameters, synthetic jet actuators receive an operating signal.

To perform the closed-loop experiments, the preliminary tests were performed to obtain the control parameters which describe the degrees of separation, such as

an angle of attack, a pressure fluctuation near leading-edge, and a gradient of mean  $C_p$  along the chordwise direction. When the stall angle is imminent ( $\alpha = 12\text{-}13$  degrees), the constant pressure region starts to appear near the leading-edge (see Fig. 4.25) and the standard deviation of  $C_p$  becomes substantially larger (see Fig. 4.27). The pressure gradient ( $dC_p/dx$ ), which is calculated from the difference of mean  $C_p$  between  $x/c = 0.02387$  and  $x/c = 0.75063$ , was selected as a control parameter for closed-loop control algorithm of fellow researcher [87]. Figure 4.43 shows the pressure gradient with varying the angle-of-attack for two freestream velocities (20 and 30 m/s). Comparing the lift coefficient curve, the pressure gradient ( $dC_p/dx$ ) increases until near the stall angle and decreases at post-stall angles of attack due to the expansion of the separation region. The pressure gradient is a criterion of flow reattachment and pressure recovery parameter on the airfoil surface. An increase of the pressure gradient can be regarded as the recovery of the pressure on the airfoil. As shown in Fig. 4.44, the pressure gradient was recovered by the effect of the synthetic jet actuator in overall oscillation frequency range. The higher the oscillation frequency is, the more the pressure recovery can increase on the airfoil. From these reasons, the flow separation is confirmed by analyzing the angle of attack, the pressure fluctuation, and pressure gradient. Accordingly, the optimal control parameters could be autonomously identified and utilized as the flow conditions change. When these control parameters are qualified, the flow separation is assumed to be detected, and closed-loop control system is designed to initiate automatically.

### **4.3.3 Flow Characteristics on a 3-D wing configuration**

#### **4.3.3.1 Synthetic jet-off**

Through experiments on a separated-flow with NACA 64A210 airfoil, the effect of the synthetic jet array and oscillation phase along the spanwise direction were identified. As already mentioned, proven cases of flow control performance on the three-dimensional wing are still in demand for a future aircraft design. In this study, flow control performance was verified on a blended wing body configuration among a few candidates for future aircraft platform. However, the flow features on the three-dimensional wing is so complicated that more cautious approach is needed. According to previous studies [54, 55], flow characteristics of blended wing body configuration are quite similar to the case of delta wing with sharp leading-edge. Therefore, flow control strategies for blended wing body configuration have much in common with those of conventional delta wing.

In three-dimensional flows, boundary layer separation leads to the formation of vortical structures [70]. Such vortices play a dominant role in the overall flow properties. The vortical structures on the wing surface may contain more than one separation line. Figure 4.45 illustrates the visualized vortex structure on a wing [88]. The picture on the top represents the flow visualization (dye emission) over a slender delta wing in a water tunnel. The picture on the bottom shows the schematic of subsonic flow field over the top of a delta wing [89]. The primary vortex comes from the rolling up of the separation surface sustained by the main separation line coincident with the leading-edge. The primary vortex steadily

increases with the angle of attack, until brutal disorganization of the structure occurs. In this case, the critical points associated with the flow pattern are located in the immediate vicinity of the wing apex where their detection is difficult [70, 90]. A phenomenon of special importance to vortical flows is vortex breakdown. Before the occurrence of breakdown, the vortex flow is organized into a nearly cylindrical and stable structure with well-defined axial, radial velocity distributions [88]. The slowly evolving rotating flow suddenly expands into a highly fluctuating structure in which both the swirling and longitudinal velocities are drastically reduced in the central part of the structure. This is known as vortex breakdown and can thus be seen as an abrupt transition between two states during which the flow organization is dramatically changed [91]. Since vortex breakdown can be viewed as a brutal amplification of disturbances leading to an expansion of the flow structure, a promising way to introduce well-defined perturbations into the flow field by implementing unsteady blowing techniques [88]. The vortex phenomena can be manipulated by altering the characteristics of the flow field such as pressure gradient, local velocity, swirl angle and effective angle of attack. Some of earliest vortical flow control studies revealed the importance of the vortex core flow with respect to the stability and controllability of the vortical flow field [92].

Based on the aforementioned flow features of a conventional delta wing, a flow separation mechanism on a blended wing body can be predicted. Figure 4.46 shows the spatial location of the vortex core and the vortex breakdown

location. Leading-edge vortex core initially shows a stable low-pressure region. This vortex core shortly develops into leading-edge vortex breakdown. When vortex breakdown take place, the vortex core suddenly expands. Vortex breakdown accelerates the flow separation at outboard region. As the angle of attack is increased, the vortex breakdown location moves upstream over the blended wing body.

To examine aforementioned flow features of blended wing body configuration, baseline experiment was performed when the synthetic jet was off. Figures 4.47-4.49 present aerodynamic forces, which were acquired by six-component external balance. The  $C_l$  curve increases linearly before the stall angle ( $\alpha = 10$  degrees) while the lift gradient begins to decrease. The  $C_d$  curve remains low before the stall angle and increases drastically after it. Figures 4.50-4.52 present the flow field using tufts visualization. Before the stall angle, there is mostly attached flow on the wing surface except at the wing tip (Fig. 4.50). At the initial stall angle, a vortex breakdown occurs along the leading-edge and tufts in that region vibrate irregularly (Fig. 4.51). At the deeper stall angle, the vortex breakdown region and the separated-flow region are merged into each other (Fig. 4.52). Though not presented here, the separated-flow region expanded greatly as the angle of attack increased. Finally, most of the wing became fully separated at  $\alpha = 20$  degrees.

Figures 4.53-4.55 present the spanwise  $C_p$  distribution near the leading-edge. The initiation of vortex breakdown can be identified by a suction peak in the

spanwise  $C_p$  distribution. As shown in Fig. 4.56, the leading-edge vortices are known to be a source of high energy, relatively high-vorticity flow [89]. Therefore, the static pressure on the top surface is reduced near the leading-edge. Spanwise  $C_p$  distributions in this experiment have much in common with the result of conventional delta wing. Before the stall angle ( $\alpha = 8$  degrees in Figs. 4.51 and 4.52),  $C_p$  distribution along the spanwise direction is nearly constant so that the suction peak is not seen, which means that the spanwise flow near leading-edge is weak. At stall angle ( $\alpha = 10$  degrees in Fig. 4.53 and 4.54), a noticeable suction peak is seen near the leading-edge. By the same token, the leading-edge vortex breakdown starts to occur, as shown in Fig. 4.49. After a deeper stall ( $\alpha = 12\text{-}16$  degrees in Figs. 4.53-4.55), the suction peak moves toward the inboard area and its range is expanded to the third line. From the aforementioned results, the vortex breakdown near the leading-edge can be explained by the strength and the position of the suction peak. Figures 4.57-4.58 present the chordwise  $C_p$  distribution on the blended wing body, which shows a separated-flow region near the leading-edge similar to the airfoil section. As already mentioned Chapter IV-3-2-1, the separated-flow region is normally observed by a constant  $C_p$  region in two-dimensional flow. The variations of  $C_p$  slope according to angles of attack mainly appear at #5<sup>st</sup> -7<sup>th</sup> lines. This is because the separated-flow region develops along the streamwise direction after leading-edge vortex breakdown, as already shown in Figs. 4.51-4.52.

#### **4.3.3.2 All-actuators-on**

Referring to the results in Chapter IV-3-3-1, the flow separation characteristics on a blended wing body are closely related to the leading-edge vortex breakdown. As already mentioned, the point of boundary-layer separation from a three-dimensional body does not necessarily coincide with the point of vanishing wall shear. For these reasons, the proper location of synthetic jet-on a wing was predicted by the computed results of baseline condition [69]. It is known that the leading-edge vortices create a strong suction on the top surface near the leading-edges. The suction effect of the leading-edge vortices, acting to increase the normal force, consequently increases the lift on the delta wing. The main objective of flow separation control in this study is to get a high lift-to-drag in the post stall regime, so the handling of leading-edge vortices is the key point for the flow control technique on the blended wing body configuration. Delay of leading-edge vortex breakdown can be captured by suppression of spanwise suction peak. A decrease of the separated - flow area is identified by the recovery of chordwise  $C_p$  slope. In this chapter, all synthetic jet modules near the leading-edge were operated in the post-stall regime to examine the overall flow control performance of a synthetic jet.

Figure 4.59 demonstrates the flow control effect of the synthetic jets in a separated-flow region. When the synthetic jet is off, tufts in the separation region vibrate randomly and their direction is opposite to the freestream direction. When synthetic jet is on, the flow becomes attached noticeably because the dead-

air region near the leading-edge is eliminated. As a result, the tufts follow the streamwise direction. These results confirm again that the synthetic jets with the improved circular exit array perform effectively on the separated region of blended wing body. Figure 4.60 shows the increment of lift and drag coefficient in the post-stall regime. The flow control performance mainly contributed to the decrement of drag, as shown in Fig. 4.60. As a result, the lift-to-drag ratio is substantially improved above the stall angle, as stated in Fig. 4.61. Since both lift and drag are increased by the suction effect caused by the leading-edge vortex, the leading-edge vortex has to be treated carefully to increase the overall performance in the post-stall regime.

The flow control mechanism in the post-stall regime is analyzed by using the flow field and  $C_p$  distribution. Among the post-stall angles,  $\alpha = 10$  and 12 degrees are selected by flow control performance.  $\alpha = 10$  degrees is the stall initiation angle, and  $\alpha = 12$  degrees is the angle which shows the best increment of  $C_l/C_d$ . Figure 4.62 represents the qualitative effect of the synthetic jet at  $\alpha = 10$  degrees. When the synthetic jet is off (Fig. 4.62a), tufts near the leading-edge vibrate somewhat irregularly and so their direction spanwise. The tuft's direction near the leading-edge implies the direction of leading-edge vortex. The leading-edge vortex breakdown is shown by the irregular motion of tufts. When the synthetic jet is on (Fig. 4.62b), the spanwise flow and the separated-flow near the leading-edge are eliminated. As a result, the tuft direction is recovered so that it is in the streamwise direction. This means that the leading-edge vortex breakdown is

suppressed by the effect of the synthetic jet momentum. Figure 4.63 presents the spanwise  $C_p$  distribution at  $\alpha = 10$  degrees. Referring to the baseline data in Figs. 4.53 and 4.54, a noticeable suction peak is seen at the stall angle. When the synthetic jet is on, the suction peak is suppressed. The weakness of the suction peak is consistent with the flow field in Fig. 4.62b. Figure 4.64 shows a chordwise  $C_p$  distribution  $\alpha = 10$  degrees. As already mentioned in Figs. 4.57-4.58, the separated-flow region is normally observed by a constant  $C_p$  region similar to the airfoil. Like the two-dimensional flow, the elimination of separated-flow region on each chordwise section is observed by the recovery of the  $C_p$  slope. The flow control effect mainly appears at the outboard region of the jet exit (#1<sup>st</sup> –6<sup>th</sup> lines), because the leading-edge vortex and mixed-jet momentum flow inboard to outboard. The leading-edge area in the #5<sup>th</sup> line has an especially high recovery for pressure loss. On the other hand, the synthetic jet merely affects the inboard area (#7<sup>th</sup> –8<sup>th</sup> lines). However, the synthetic jet has a negative influence on the #3<sup>rd</sup> and #4<sup>th</sup> lines whose  $C_p$  slopes are lower than that in the baseline case. This means that the uniform supply of jet momentum near the leading-edge may reduce the flow control performance at specific areas. From this perspective, it is observed that more efficient flow control technique is needed to solve a local degradation of the synthetic jet.

Figure 4.65 shows tuft visualization in the case of  $\alpha = 12$  degrees. The separated-flow region is not completely removed by the synthetic jet as compared to the result of  $\alpha = 10$  degrees that is shown in Fig. 4.62. Instead, the location of the

leading-edge vortex breakdown moves outboard and the separated-flow area is reduced. Figure 4.66 presents a spanwise  $C_p$  distribution at  $\alpha = 12$  degrees. The suction peak is not completely eliminated, compared to the result of  $\alpha = 10$  degrees as shown in Fig. 4.63. Instead, its strength is reduced and its position moves outboard. Figure 4.67 shows the chordwise  $C_p$  distribution at  $\alpha = 12$  degrees. Comparing this to the results of  $\alpha = 10$  degrees (Fig. 4.64), the synthetic jet positively affects it through a wide area, where the  $C_p$  slopes are generally recovered throughout the #1<sup>st</sup> – 5<sup>th</sup> lines. However, the  $C_p$  slope at the #6<sup>th</sup> line is decreased by the synthetic jet. The flow characteristics of all-actuators-on experiment demonstrate that the synthetic jet is effective at controlling the leading-edge vortex breakdown near the leading-edge. These results are caused by the changing position of the leading-edge vortex breakdown and jet momentum of the synthetic jet. As the angle of attack increases, the position of the leading-edge vortex breakdown moves inboard and its strength increases (Figs. 4.53-4.55). The leading-edge vortex breakdown happens at the inner inboard region and the separated-flow region becomes larger as the angle of attack increases. Thus, the synthetic jet affects through a wide area (#1<sup>st</sup> – 5<sup>th</sup> lines) at  $\alpha = 12$  degrees. However, the jet momentum of the synthetic jet is fixed at  $f = 200$  Hz, so the same amount of jet momentum as  $\alpha = 10$  degrees condition is not enough to eliminate the suction peak at that. Thus, the flow control performance of  $\alpha = 10$  degrees is shown more clearly than that of  $\alpha = 12$  degrees. From the overall results of  $C_l/C_d$  curve and  $C_p$  distributions, it is observed that the synthetic jets with the improved circular

exit array perform effectively on the separated region of blended wing body configuration. However, at the same time, more efficient flow control technique is needed to enhance the performance of synthetic jet.

#### **4.3.3.3 Selective-actuators-on**

Aforementioned experiment shows overall performance of synthetic jet-on a blended wing body configuration. At the same time, it is observed that a uniform supply of jet momentum near the leading-edge has a limitation because the jet momentum adversely affects some areas. Therefore, the selective supply of jet momentum experiment was designed to overcome the traditional method of uniform supply at the leading-edge. In order to find an effective flow control method according to the leading-edge vortex breakdown position, the flow control experiments were performed by changing the number of synthetic jet modules. Figures 4.68 and 4.69 show the increment of  $C_l/C_d$  depending on the number of synthetic jet modules. Figure 4.68 (total increment of  $C_l/C_d$ ) indicates the overall quantity of flow control and Fig. 4.69 (increment of  $C_l/C_d$  per module) refers to the flow control efficiency. When the flow control performance is the highest at the lowest power consumption, there is efficient flow control. Therefore, the selective operating technique is important in considering the practical use and power consumption of synthetic jet modules. As shown in Fig. 4.68, the more synthetic jet module operates the higher overall flow control performance. However, as the number of synthetic jet modules increases, the efficiency is generally reduced, as

shown in Fig. 4.69. Furthermore, as we focus on the results of two-modules in Fig. 4.69, the relationship between the synthetic jet positions and the leading-edge vortex breakdown is identified. Table 4.1 quantitatively compares the flow control performance according to the number of synthetic modules. The first and second cases of synthetic jet module numbers are summarized in Table 4.1 When  $\alpha = 10$  degrees, the first case commonly includes #5 and #6 modules, while the second case has #4 and #5 modules. When  $\alpha = 12$  degrees, even though the first and second cases are shifted a small quantity of  $C_l/C_d$  increment, all cases include #1 and #2 or #6 and #7 modules. From this perspective, the relationship between the leading-edge vortex breakdown position and synthetic jet modules is analyzed. Figures 4.70-4.73 show the chordwise and spanwise  $C_p$  distributions. The results of the two-module cases in Table 4.1 and the result of all-module case in Chapter IV-3-3-2 are compared to one another. When  $\alpha = 10$  degrees, the locations of suction peak at the #1<sup>st</sup> line are moved outboard by the two-module actuation (Fig 4.70). This movement of the suction peak is inferior to the elimination of the suction peak in an all-actuators-on case, but the strength of the suction peak is equally suppressed at the #2<sup>nd</sup> line. Moreover, the chordwise  $C_p$  distribution (Fig. 4.71) indicates that the recovery of the  $C_p$  slope can be achieved by two-module case. When  $\alpha = 12$  degrees, the results of the #6 and #7 modules and the results of #1 and #2 modules are similar with respect of the amount of  $C_l/C_d$  increment (Fig. 4.69). However, the flow control mechanisms of those cases are different, as shown in Fig. 4.72. Because the #6 and #7 modules are located near the leading-edge

vortex breakdown, these modules contribute to the suction peak movement toward outboard at the first line (Fig. 4.72). On the other hand, the #1 and #2 modules in the separated-flow region do not directly affect the movement of the suction peak, and cause pressure recovery at the outboard area instead ( $y/b = 0.75 - 0.85$  in the #1<sup>st</sup> line, Fig. 4.72). The chordwise  $C_p$  distribution (Fig. 4.73) also compares the characteristics of flow control according to the synthetic jet position. In the case of the #6 and #7 modules, the pressure recovery level at the 5<sup>th</sup> line is similar to an all-actuators-on case. On the other hand, in the case of the #1 and #2 modules, the pressure recovery level at the #5<sup>th</sup> line is lower than that of the all-actuators-on case. However, a beneficial effect is shown considering the pressure loss at the #6<sup>th</sup> line that is observed in an all-actuator-on case. From these results it is possible to note that the flow control mechanism is changed by the position of synthetic jet, or the supply of jet momentum. When there is initial stall (Fig. 4.74), the leading-edge vortex breakdown starts mildly and the separated-flow region is small. Thus, the direct supply of jet momentum at the leading-edge vortex breakdown is effective. Therefore, as the further synthetic jet modules are away from the leading-edge vortex breakdown (suction peak), the less likely synthetic jet control on the separated-flow region is identified. When there is deeper stall (Fig. 4.75), the leading-edge vortex breakdown happens strongly at the inner inboard region and the separated-flow region is large. Thus, the direct supply of jet momentum at the suction peak contributes to the movement and suppression of the leading-edge vortex breakdown. The supply of jet momentum at the separated-flow region of

outboard brings about pressure recovery at the outboard region. These results confirm that the synthetic jets with efficient flow control technique perform effectively when used to control the separated region of the blended wing body configuration.

## V. Concluding Remarks

### 5.1. Summary

The flow characteristics of piezoelectrically driven synthetic jets with a circular exit array were investigated using experimental methods under various flow conditions. Step-by-step experiments were conducted to find an improved configuration of a circular exit array while some parameters were held constant, specifically the oscillation frequency, input voltage, and exit area. For the quiescent condition, the jet characteristics depending on the overall hole perimeter and the oscillation frequency were compared by measuring the jet velocity profiles by means of hot-wire anemometry. For the same exit area, the jet velocity decreased as the total hole perimeter increased. Thus, the hole diameter should be optimized to increase the momentum flux under a constant exit area condition. For the forced separated-flow condition, the  $C_p$  distributions on an inclined flat plate were compared for an improved exit configuration by changing the design parameters of the hole diameter, hole gap, synthetic jet array type, and oscillation phase. Experimental results were compared with computational results of reference papers in order to understand flow characteristics of synthetic jet in detail. The hole diameter affects the peak jet velocity and the hole perimeter, which are closely related to the jet momentum and the effective jet area. In addition, the hole gap determines the vortex

interaction between adjacent exit holes. Thus, the hole diameter and the hole gap should be properly designed to provide an adequate amount of jet momentum as well as an adequate effective area and to obtain a relatively strong and more sustainable vortical structure. Regarding the jet array type and oscillation phase, the dual array was found to be more effective for reducing flow fluctuation near the leading-edge at high angles of attack, and phase difference oscillation of 180 degrees was shown to improve the flow control performance for a wide range of actuating frequencies. For the separated-flow condition on the NACA 64A210 airfoil, it was verified that the synthetic jet system with the improved design parameters showed desirable flow control capability. Through separation control experiments at high angles of attack, the lift-to-drag ratio notably increased. It is, therefore, concluded that flows over an airfoil configuration at high angles of attack can be properly controlled by applying piezoelectrically driven synthetic jets with improved design parameters. For the separated-flow condition over a blended wing body configuration, it was also verified that the synthetic jet system with the improved design parameters showed desirable flow control capability. Through various aerodynamic data and flow visualization, the leading-edge vortex breakdown was observed to mainly affect the separated-flow physics in the post-stall regime. For the case of all-actuators-on condition, the full operation of synthetic jet modules near the leading-edge effectively suppressed the development of the leading-vortex breakdown and considerably reduced the separated-flow region at the initial stall stage. At the same time, a

uniform supply of jet momentum showed the limitation of local pressure loss at the leading-edge. For the case of selective-actuators-on condition, a selective operation of the jet module was investigated to enhance the efficiency of synthetic jet. At the initial stall stage, a pinpoint operation of the synthetic jet effectively controlled the strength of the leading-edge vortex breakdown, even though a relatively small amount of jet momentum was supplied. For deeper stall, a direct supply of jet momentum at separated-flow region was also effective at controlling the starting point of the leading-edge vortex breakdown. From these results, it was concluded that the strategic operation of the synthetic jet over a blended wing body was an efficient alternative to controlling the separated-flow region in a post-stall regime while considering power consumption.

## **5.2. Future Works**

In present studies, it was verified that the synthetic jet system with the improved design parameters showed a desirable flow control capability at high angles of attack. This work has yielded an improved understanding of the fluid mechanism of synthetic jets with circular exit array in a separated-flow region, and the conditions for producing effective flow control for delaying separated-flow region have been established. However, at the same time, it is noted that more realistic flow control technique is needed for real-flight condition. The more jet momentum is needed to control massive flow separation caused by high-speed flight. In addition, the separation location usually moves variously in a real-flight condition depending on the aircraft posture. Thus, flow control by synthetic jet-on a massive separated-flow is still a challenging task because designed synthetic jet system should meet constraints of volume installation and power consumption. In order to develop enhanced synthetic jet system, both experimental and numerical method under various conditions should be studied continuously. Full-scale aircraft for the wind tunnel test is so expensive to operate that extensive numerical computations are carried out by a well-validated flow solver to predict the flow control mechanism. Based on the computed results of baseline condition, synthetic jet system can be designed according to the required performance. Furthermore, in practical synthetic jet design, more various design parameters should be considered for full-scale flight condition. Figure 4.76 shows possible future research topics.

First, the effects of actuator technology and associated power systems architecture on the mass cost and power consumption of synthetic jet system should be studied in the future. Because a power source of aircraft is predetermined by design stage, a trade-off exists between system power efficiency and the system hardware mass required to achieve this efficiency. Second, it is possible that individual closed-loop control system based on selective-actuators-on condition is developed. Flow control system is autonomously operated by the information of spanwise and chordwise  $C_p$  distributions. Separated-flow region on the wing is efficiently suppressed by the minimum synthetic jet actuators in the critical area.

## Figures

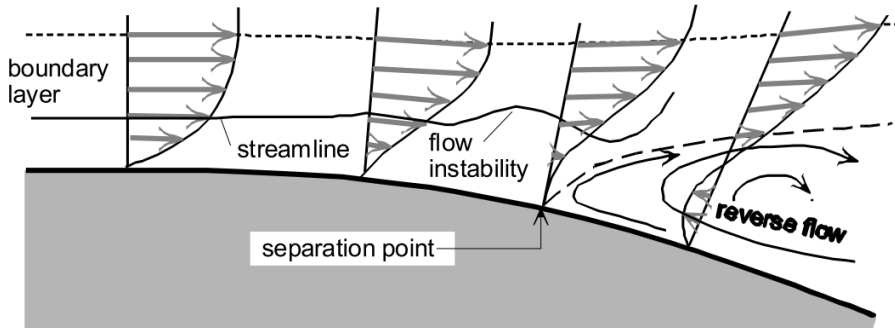


**Fig. 1.1 Schematic view of laminar boundary layer separation at a curved surface [4]**

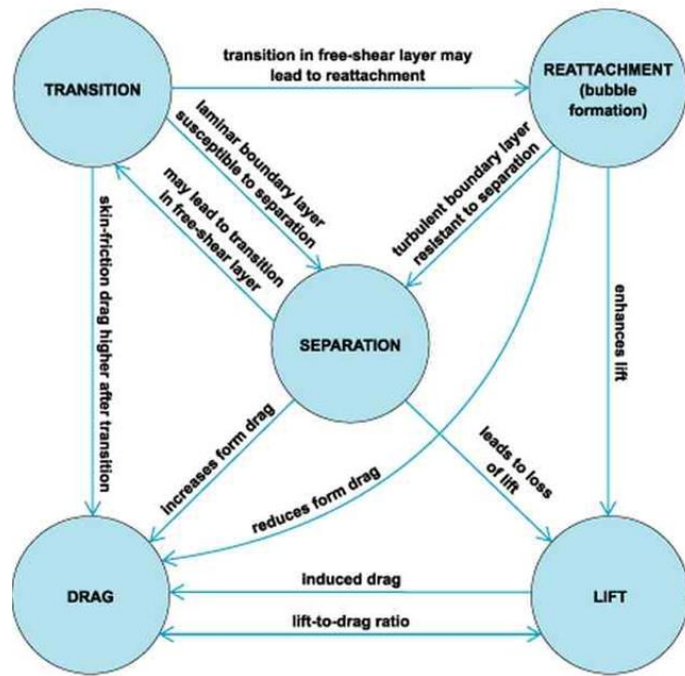


**Fig. 1.2 Interrelation between flow-control goals [5]**



Fig. 1.3 Requirement for future aircraft

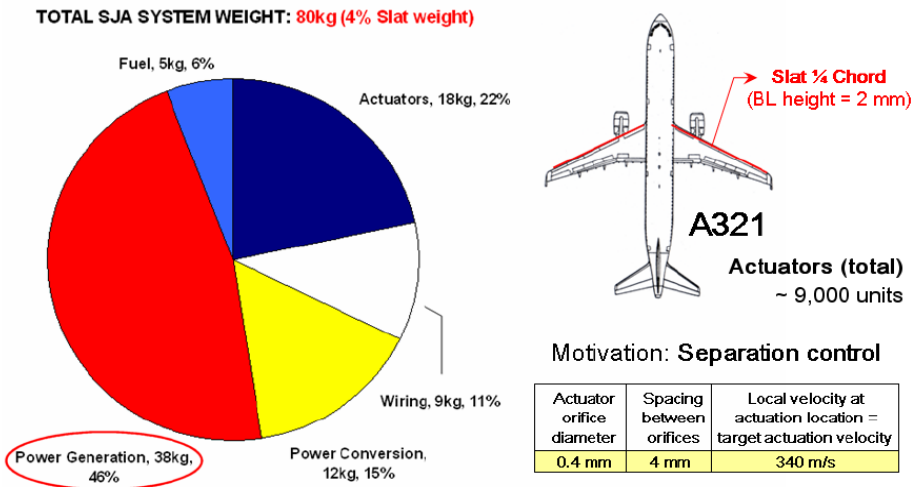
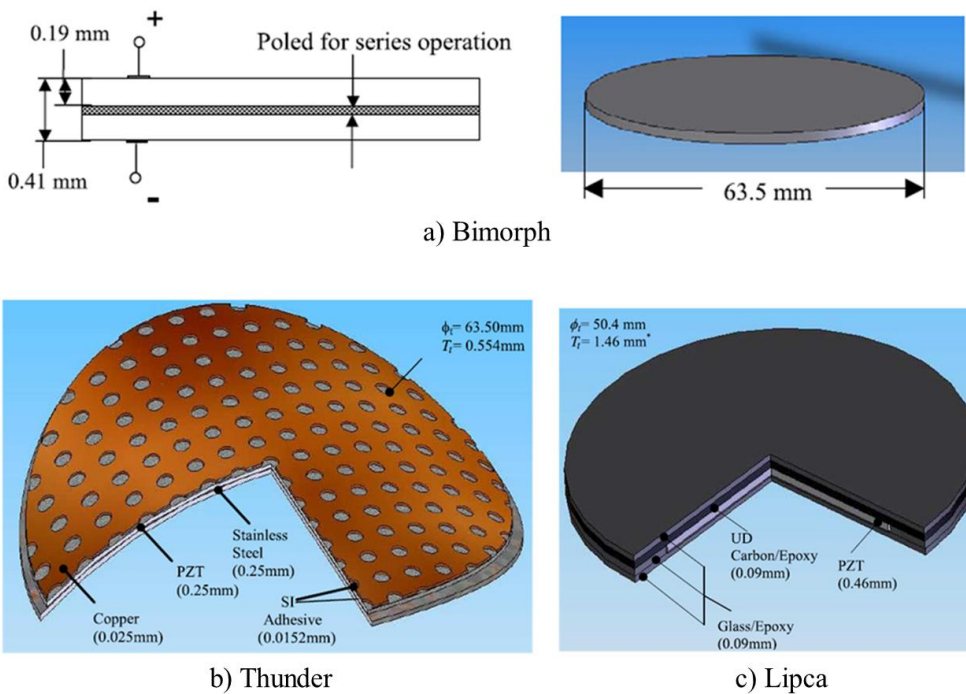
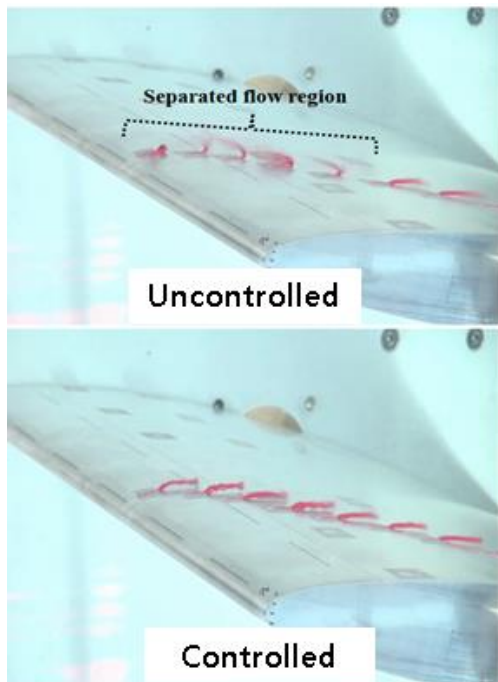


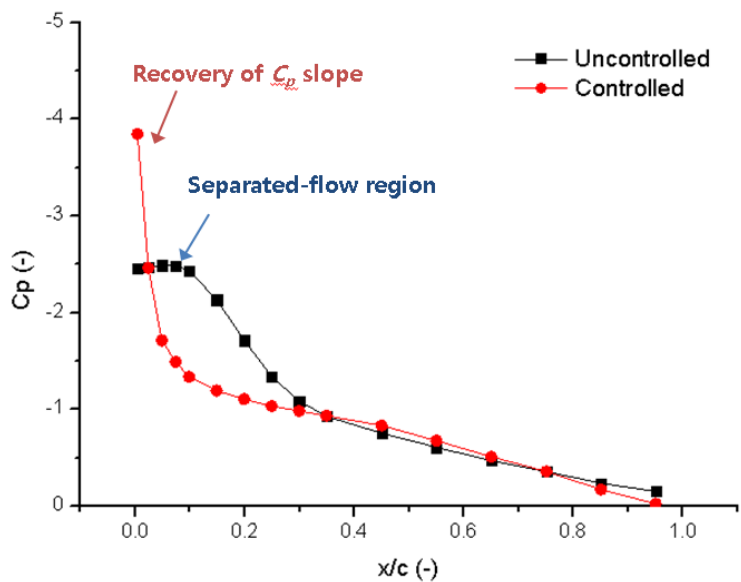
Fig. 1.4 Comparison with the existing slat application [26]



**Fig. 1.5 Types of piezoelectric disk [8]**

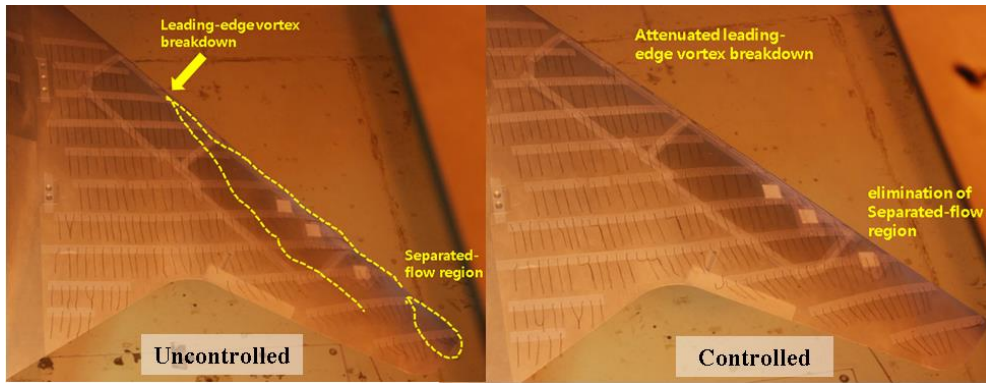


a) Flow visualization

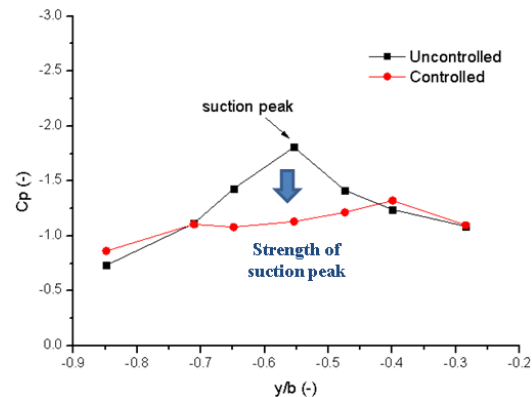


b) Chordwise  $C_p$  slope

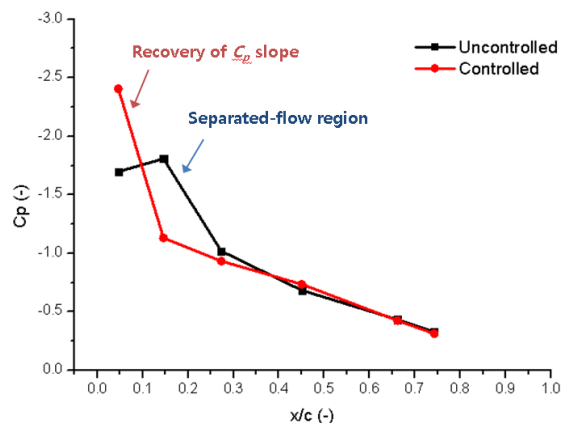
Fig. 1.6 Flow control strategy on a 2-D airfoil



a) Flow visualization



b) Spanwise  $C_p$  distribution



c) Chordwise  $C_p$  distribution

Fig. 1.7 Flow control strategy on a 3-D wing

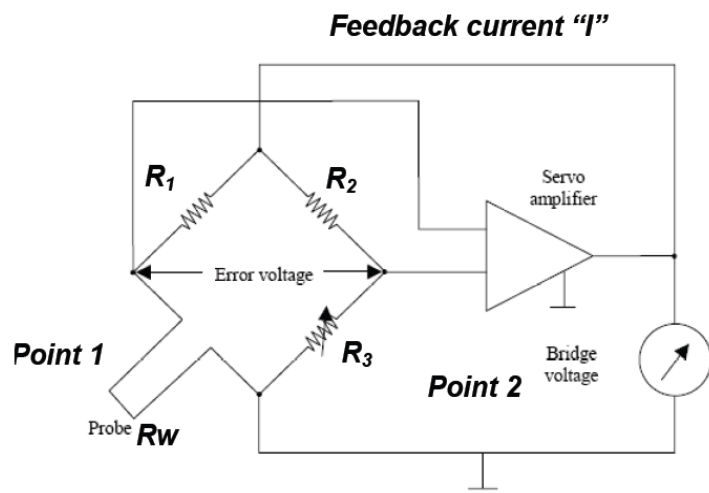


**Fig. 2.1 Circuit diagram of CTA**

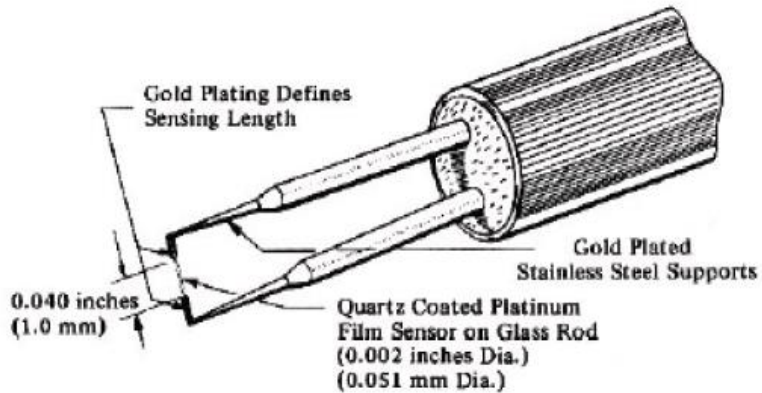


**Figure 2: Cylindrical Hot Film Sensor and Support Needles-  
0.002" Dia. (0.051 mm)**

**Fig. 2.2 I-Type hot wire anemometer**

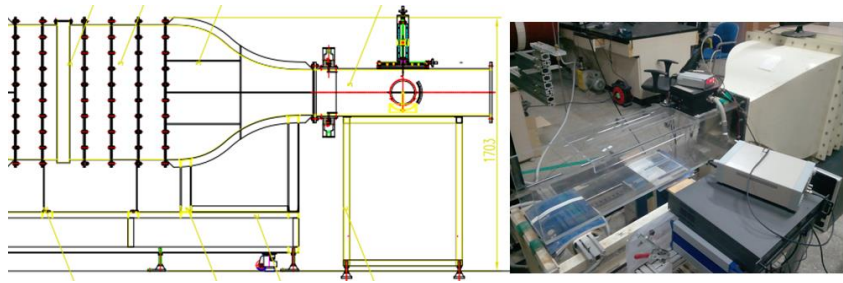


**Fig. 2.3 Subsonic wind tunnel at Seoul National University  
(test section of 200 mm × 200 mm × 1000 mm)**

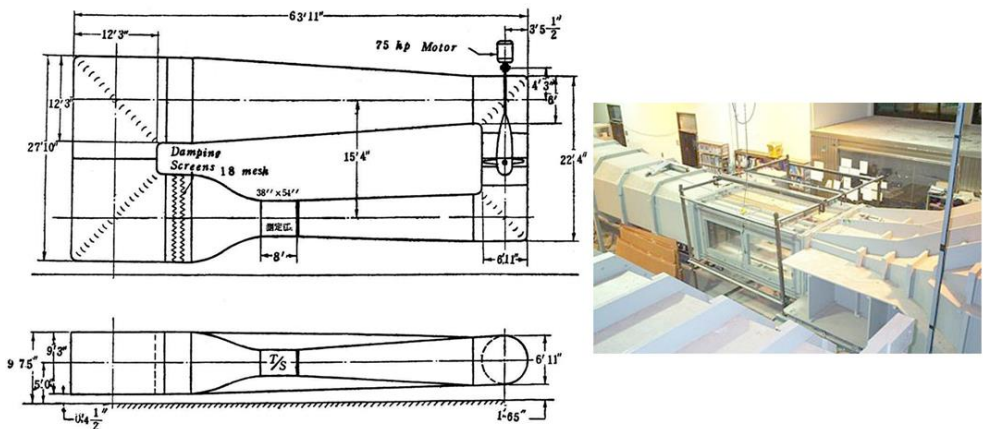


**Fig. 2.4 Subsonic wind tunnel at Seoul National University  
(test section of 1350 mm × 950 mm × 2440 mm)**

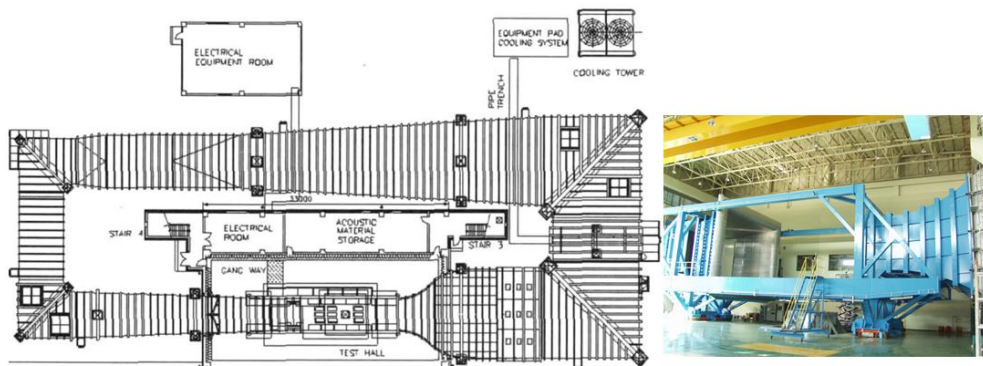


**Fig. 2.5 Subsonic wind tunnel at Korea Aerospace Research Institute  
(test section of 4 m × 3 m)**

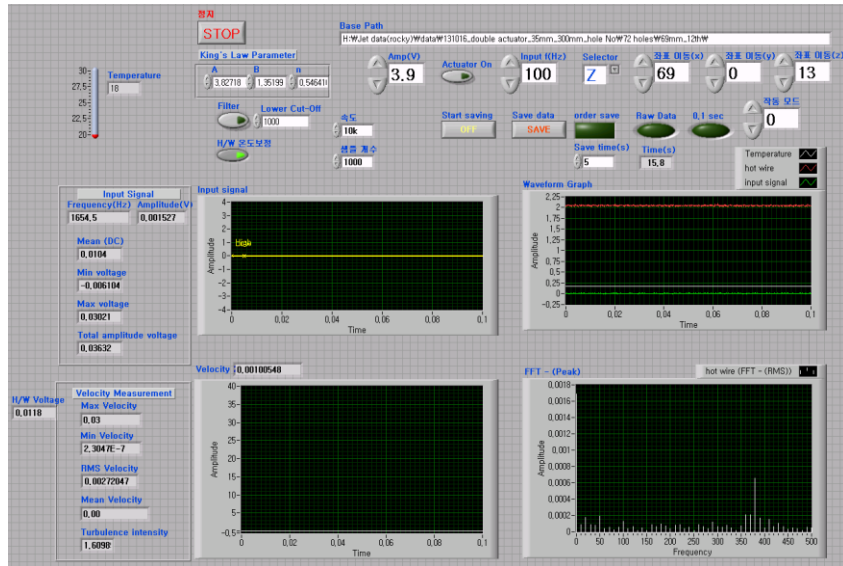


Fig. 2.6 Labview display (front panel)

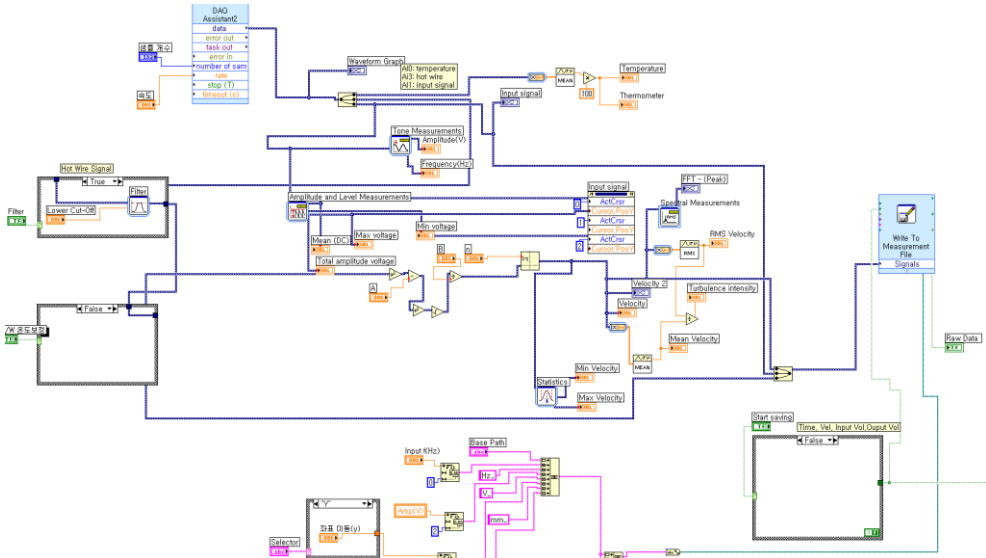


Fig. 2.7 Labview display (block diagram)

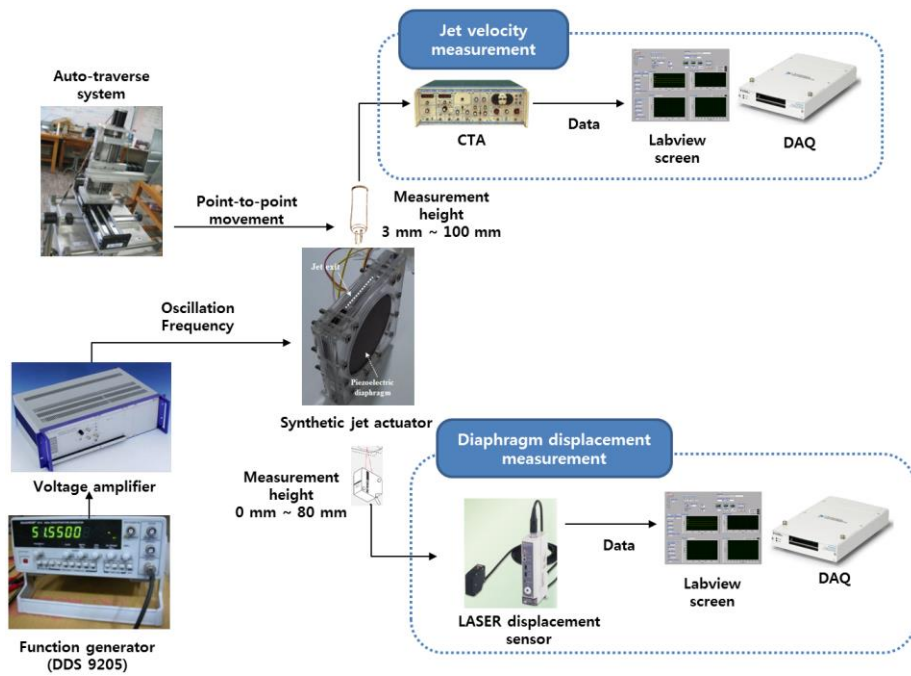


Fig. 3.1 Data acquisition setup in the quiescent condition

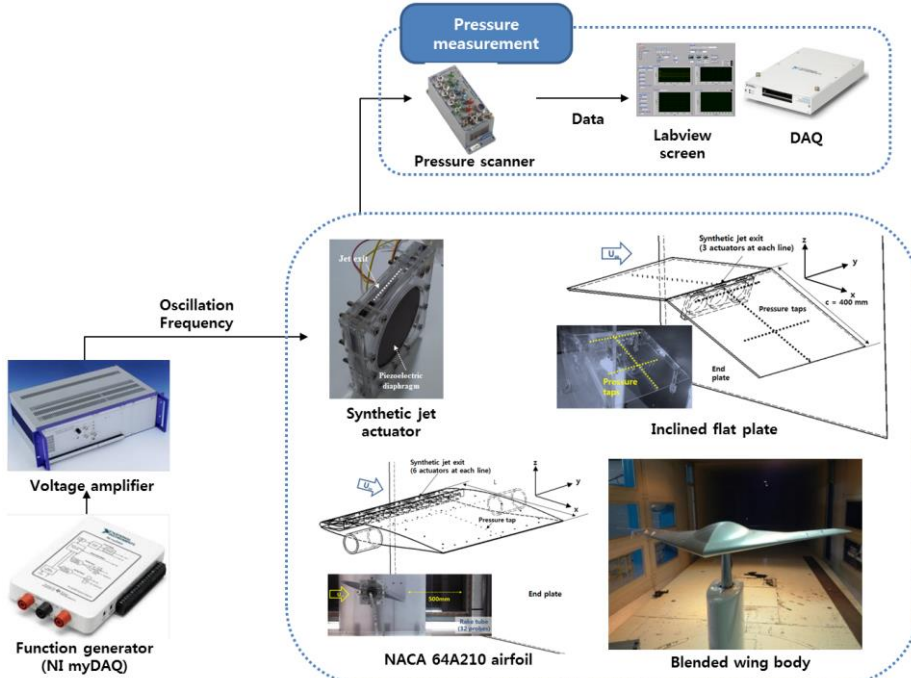
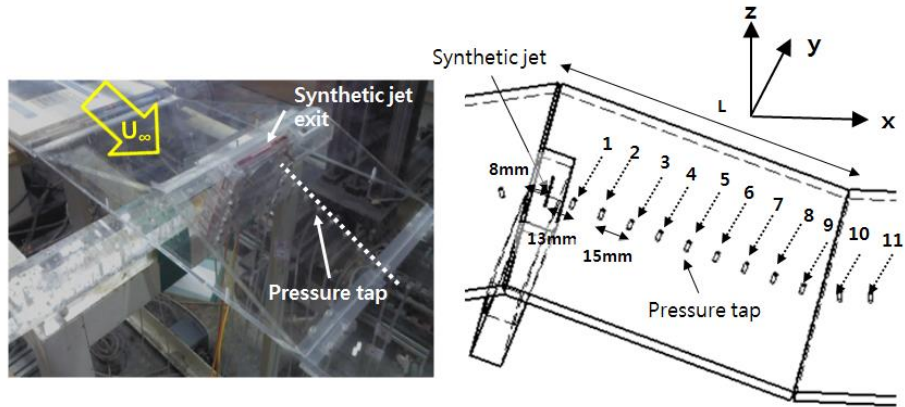
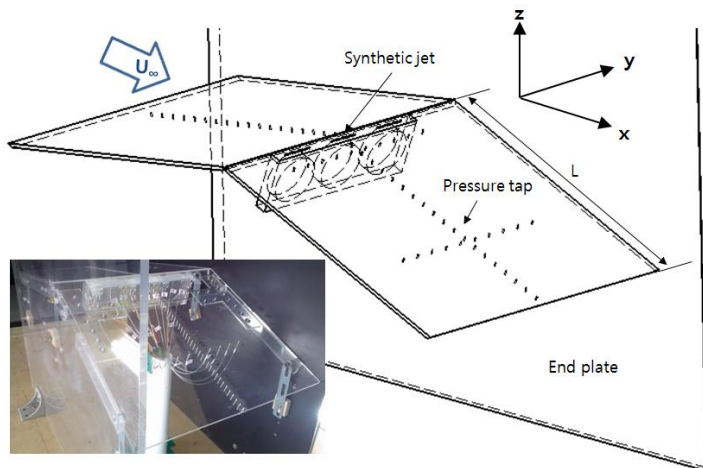


Fig. 3.2 Data acquisition setup in the cross flow condition



**Fig. 3.3 Inclined flat plate setup for the design parameters of circular exit array**



**Fig. 3.4 Inclined flat plate setup for the synthetic jet array and oscillation phase**

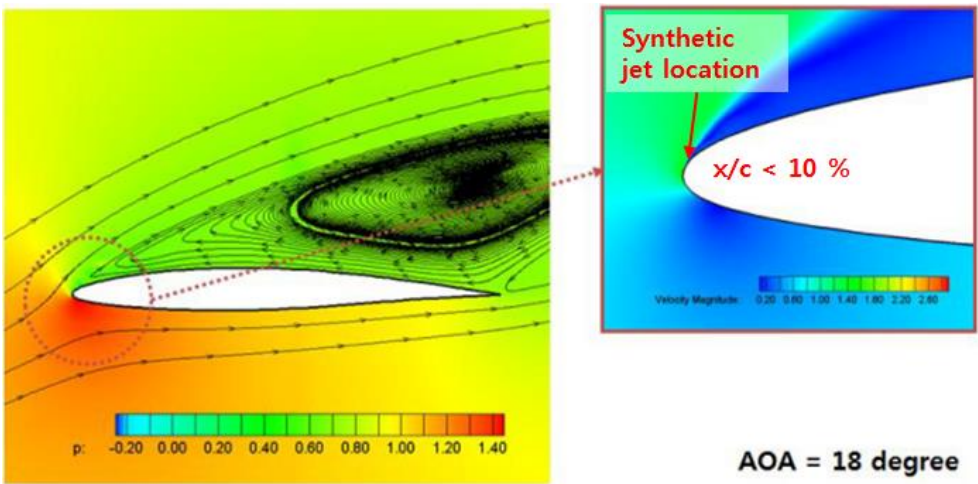


**Fig. 3.5 Computed results and synthetic jet location [64]**

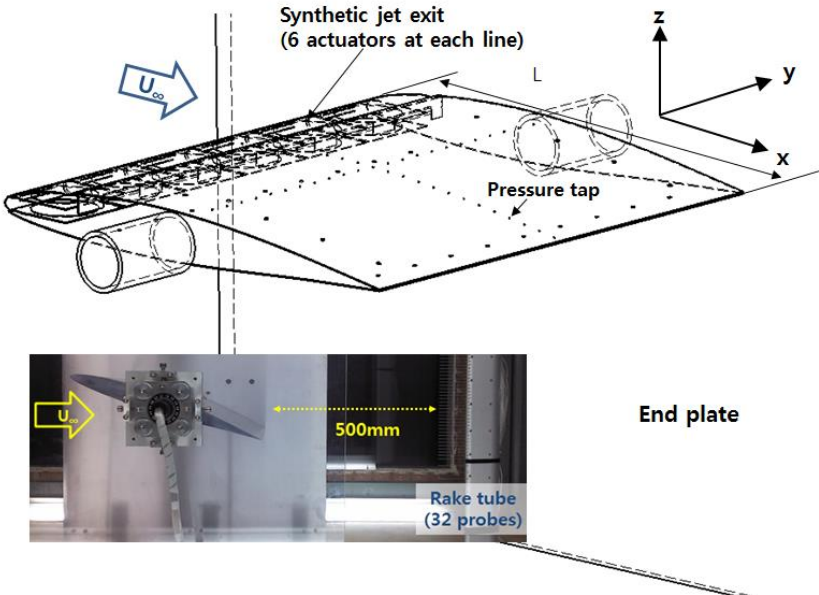


**Fig. 3.6 NACA 64A210 airfoil test setup**

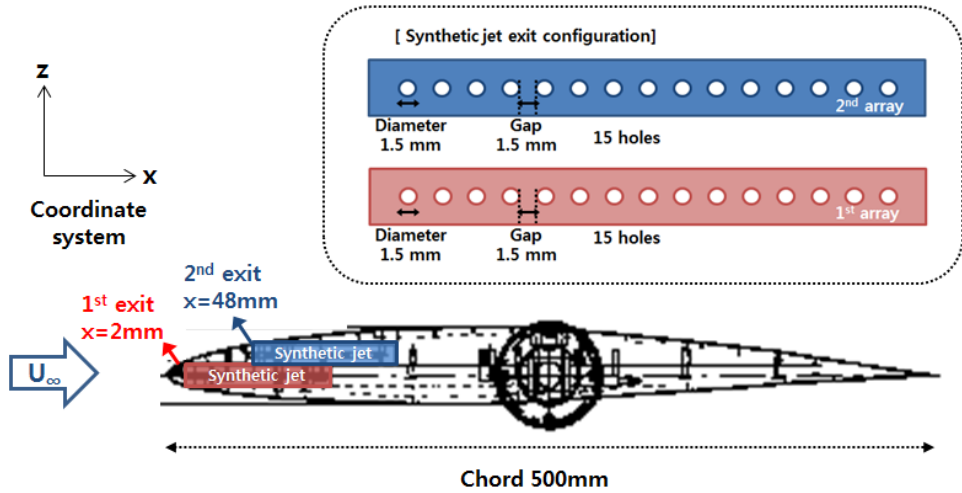


Fig. 3.7 Schematic of NACA 64A210 airfoil model

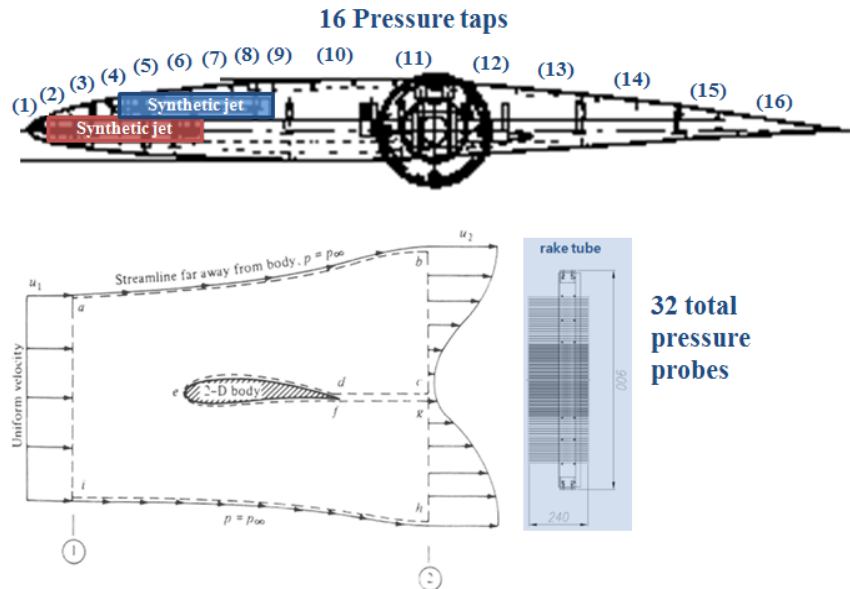
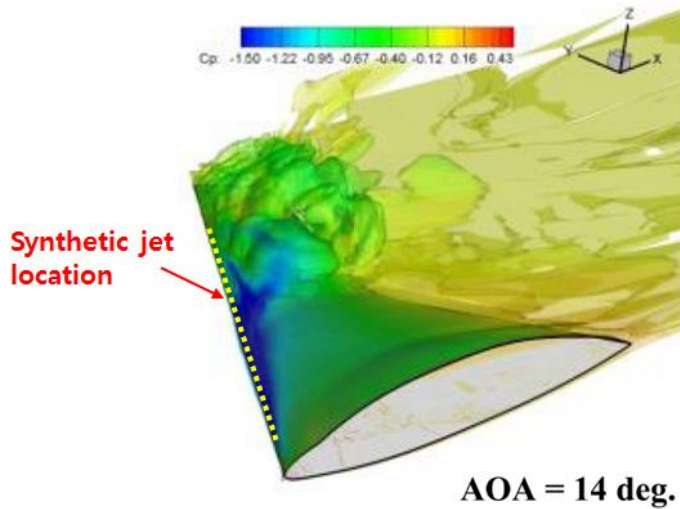
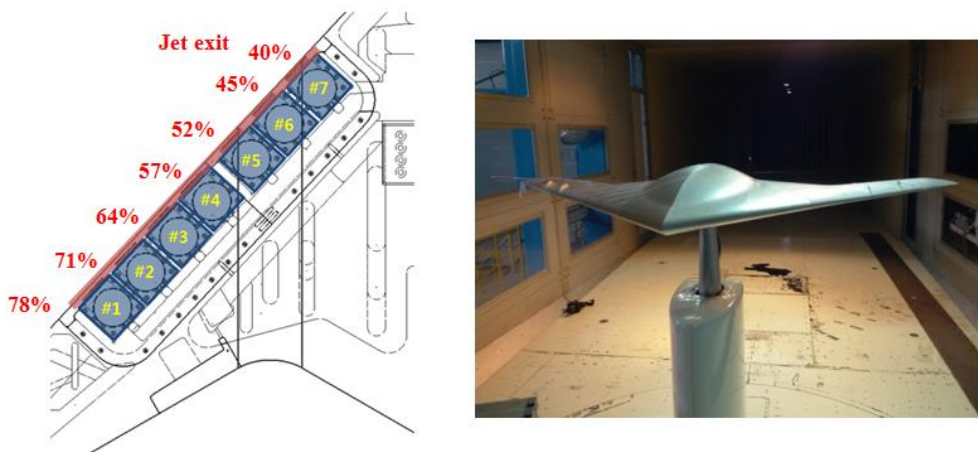


Fig. 3.8 Methods for pressure data acquisition



**Fig. 3.9 Computed results and synthetic jet location [64]**



**Fig. 3.10 Wind tunnel test setup of 3-D wing configuration**

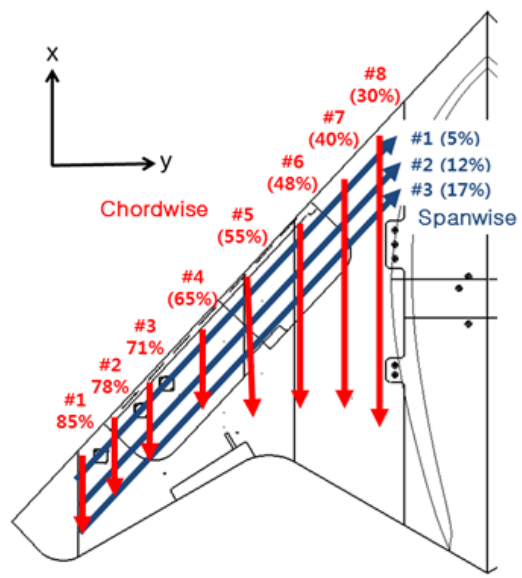
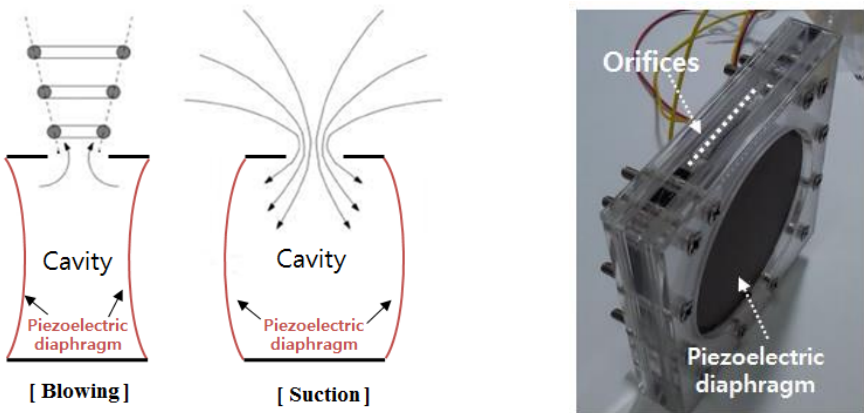
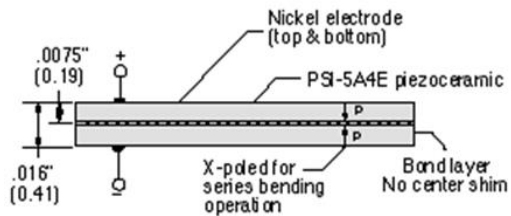
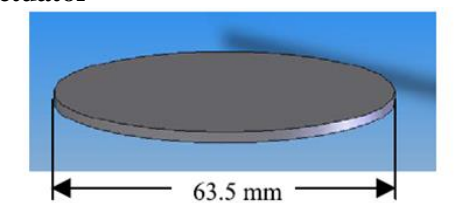


Fig.3.11 Location of pressure taps of 3-D wing configuration



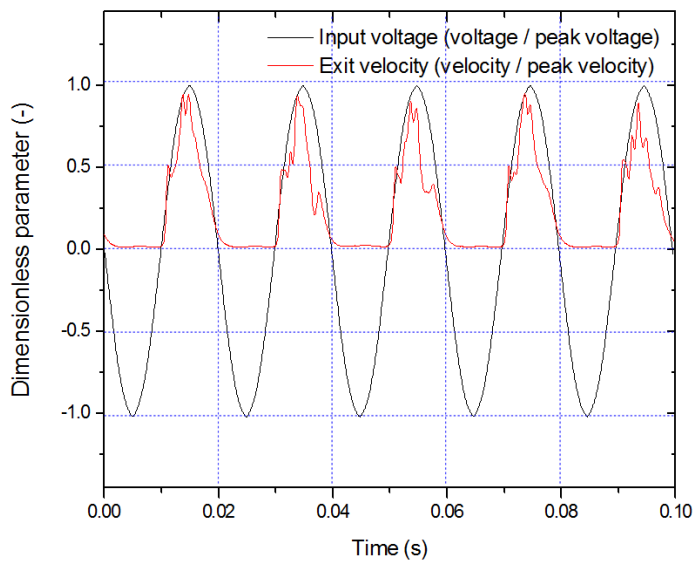
a) Principle of dual-diaphragm actuator

b) Manufactured synthetic jet

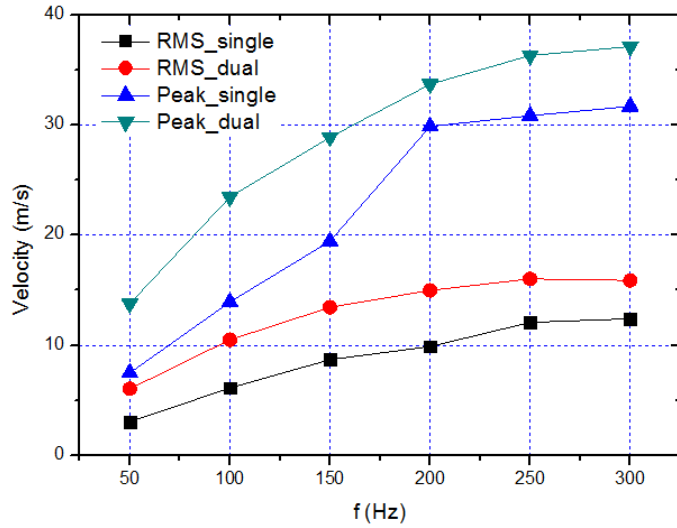


c) Bimorph piezoelectric disk

Fig. 4.1 Synthetic jet performance test (exit type 1-1)



a) Jet velocity profile ( $f = 50$  Hz)



b) Jet velocity depending on diaphragm type

Fig. 4.2 Synthetic jet performance test (exit type 1-1)

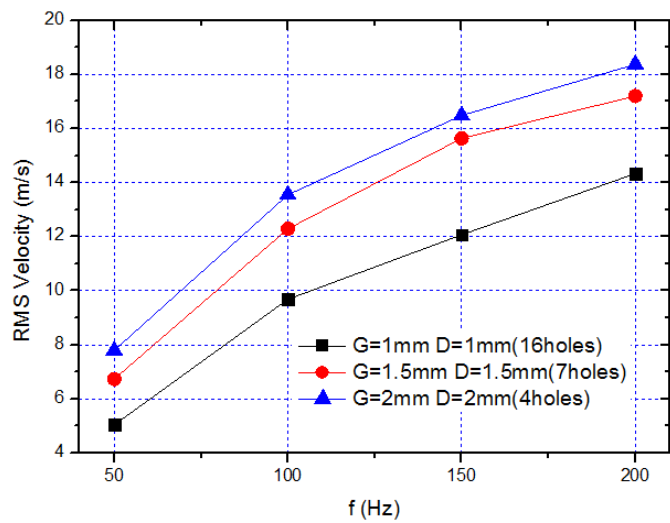


Fig. 4.3 RMS jet velocity (exit types 1-1, 1-2, and 1-3)

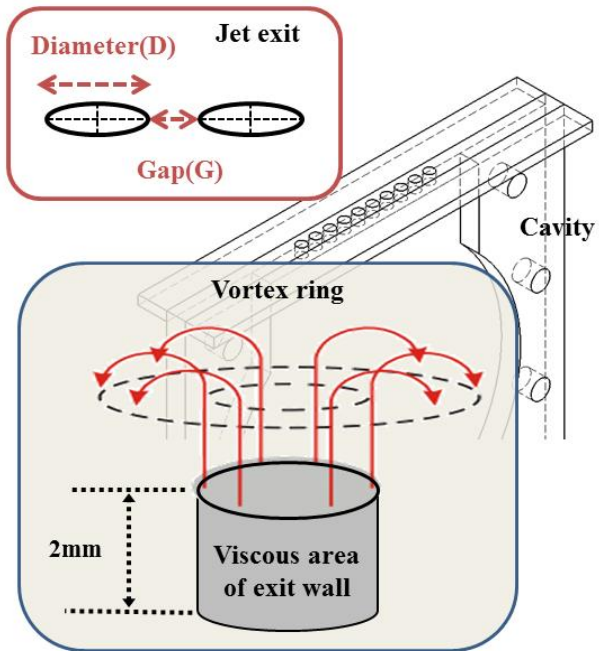
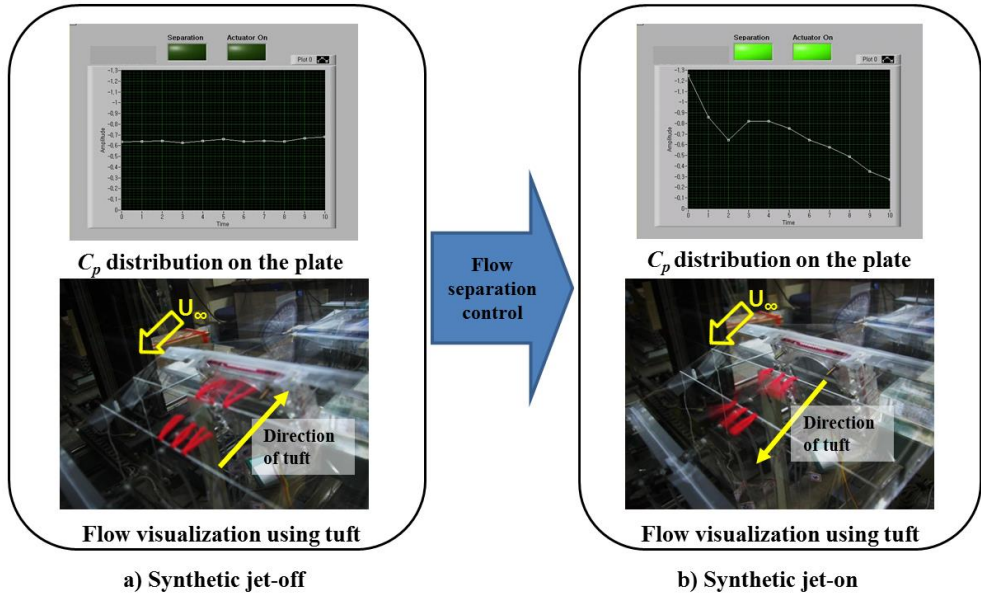
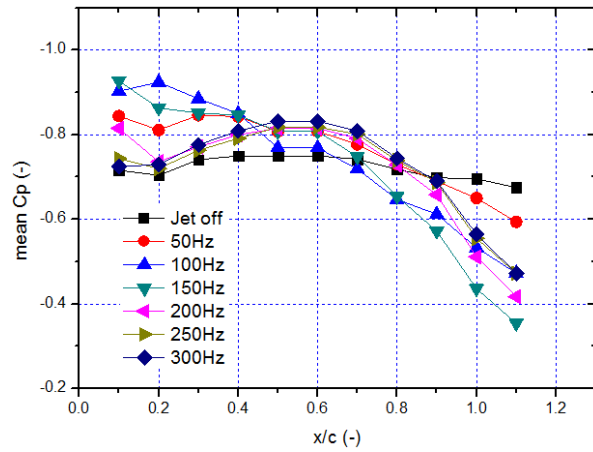


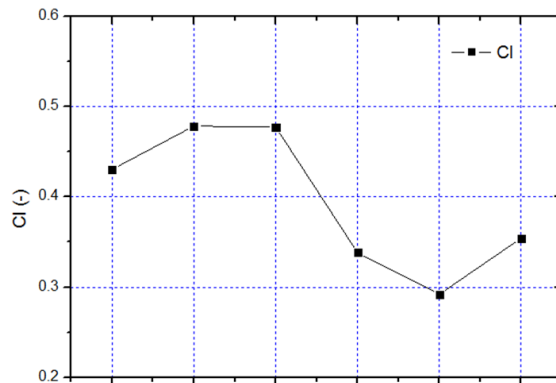
Fig. 4.4 Viscous area of exit wall surface



**Fig. 4.5 Effect of synthetic jet actuation ( $U_{\infty} = 10 \text{ m/s}$ ,  $f = 120 \text{ Hz}$ )**



a)  $C_p$  distribution on the rear plate



$f$	50	100	150	200	250	300
$C_\mu (\%)$	0.110	0.331	0.543	0.674	0.771	0.757
$F^+(-)$	0.75	1.5	2.25	3	3.75	4.5

b)  $C_l$  of the rear plate

Fig. 4.6 Aerodynamic forces depending on oscillation frequency ( $f = 50\text{-}300$  Hz)

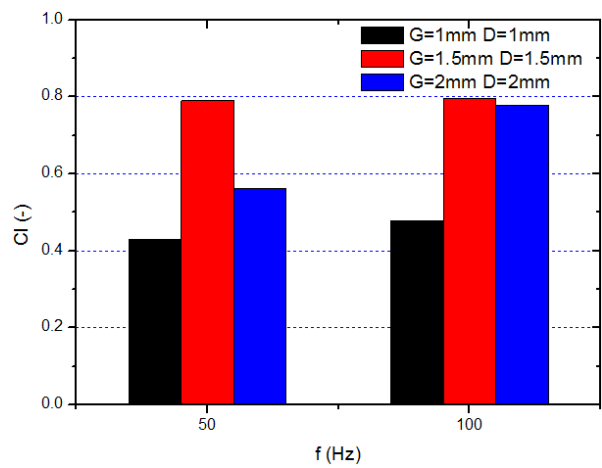
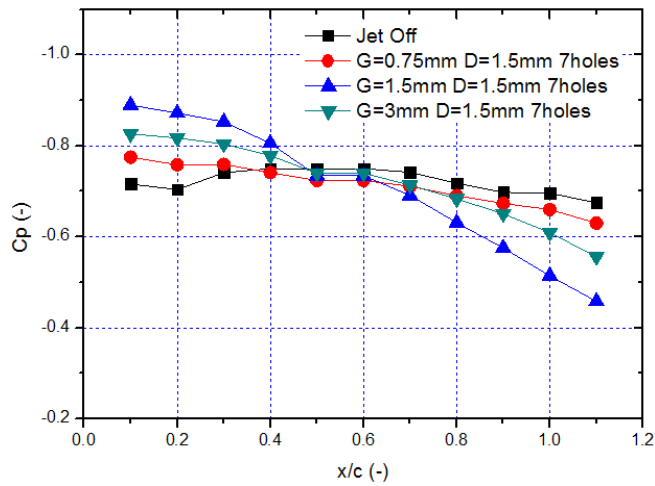
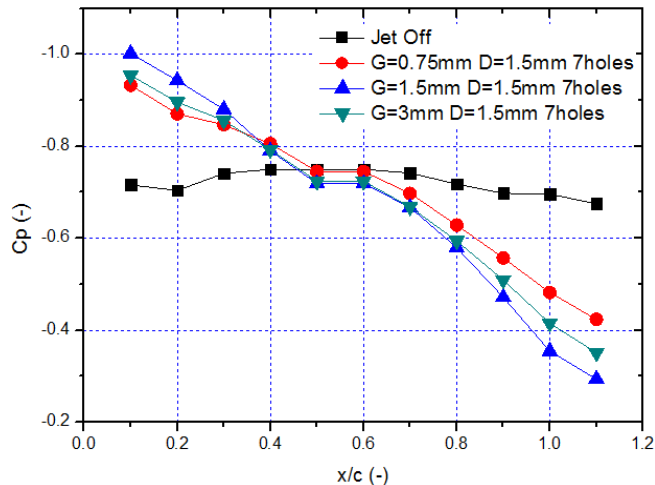


**Fig. 4.7 Lift coefficient on the rear plate (exit types 1-1, 1-2, and 1-3)**

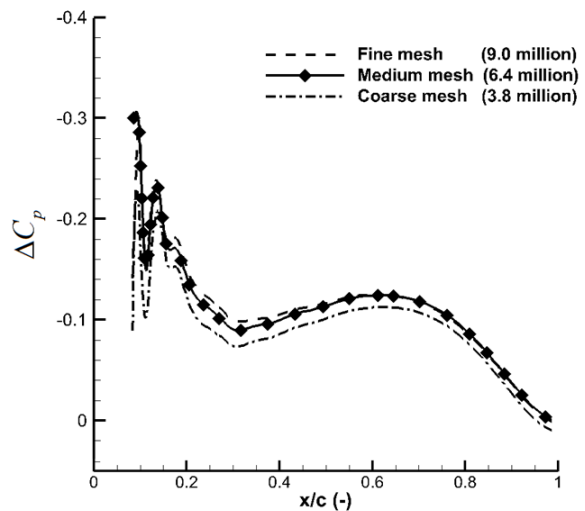


a)  $C_\mu = 0.109, F^+ = 0.75$

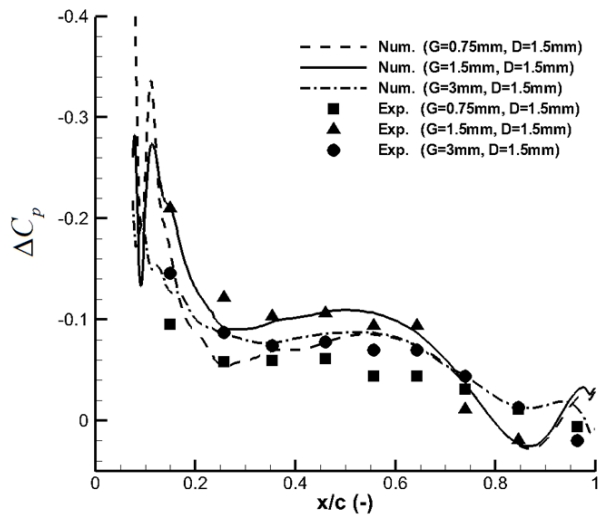


b)  $C_\mu = 0.331, F^+ = 1.5$

**Fig. 4.8**  $C_p$  distribution on the rear plate (exit types 2-1, 2-2, and 2-3)

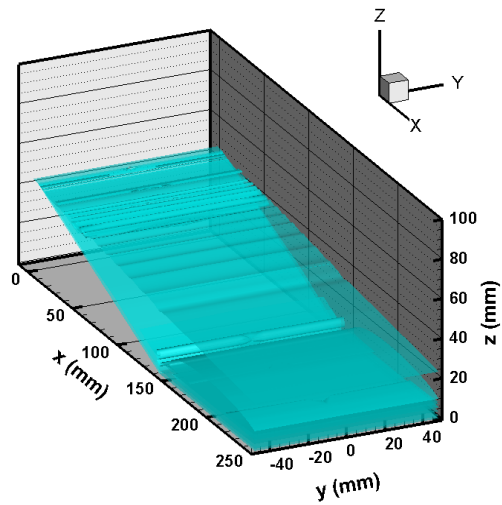


a) Computational grids sensitivity test (exit type 2-2)

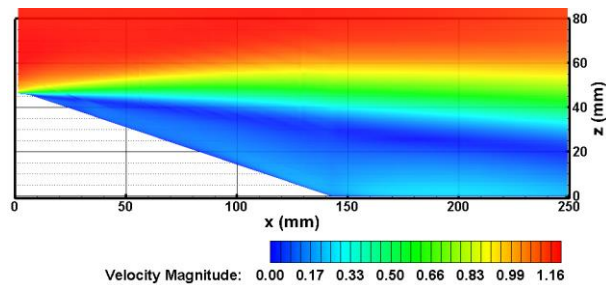


b) Code validation (exit types 2-1, 2-2, and 2-3)

Fig. 4.9 Validation of numerical simulation

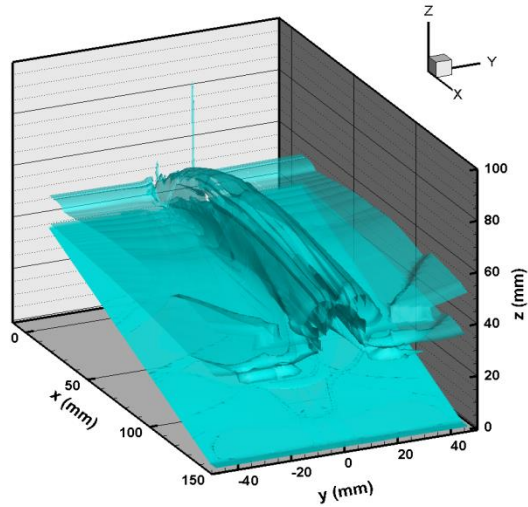


a) Phase-averaged iso- vorticity surface contours

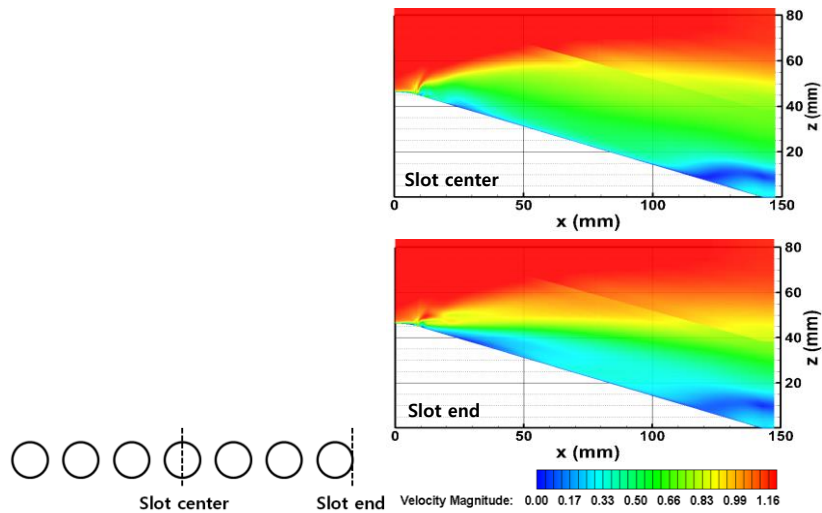


b) Velocity magnitude contours at x-z plane

Fig. 4.10 Synthetic jet-off

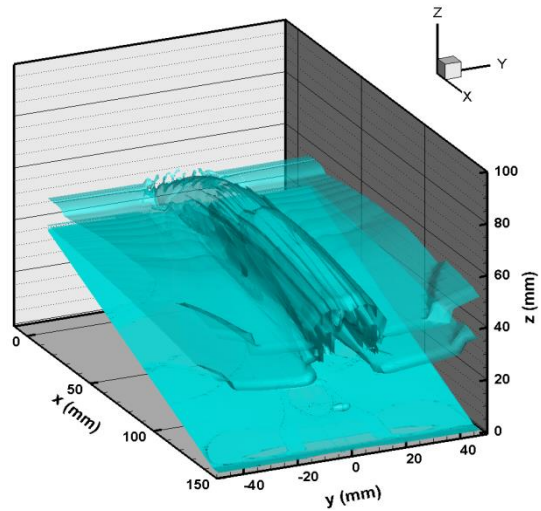


a) Phase-averaged iso- vorticity surface contours

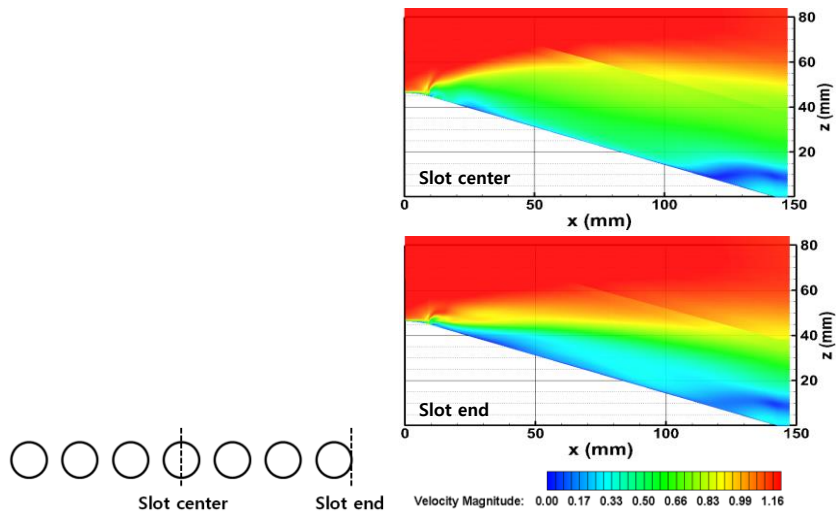


b) Velocity magnitude contours at x-z plane

Fig. 4.11 Exit type 2-1 ( $G = 0.75 \text{ mm}$ ,  $D=1.5\text{mm}$ )

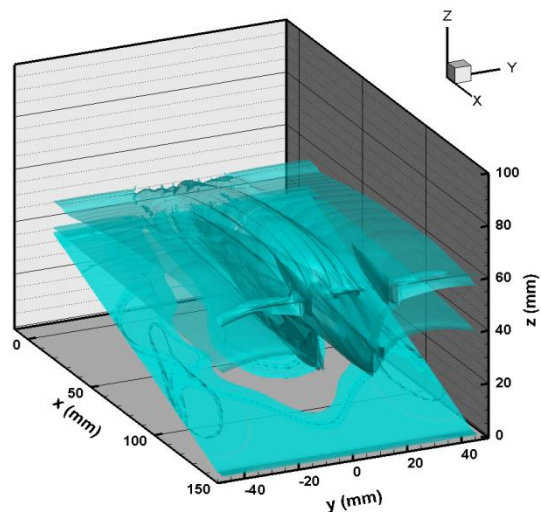


a) Phase-averaged iso- vorticity surface contours

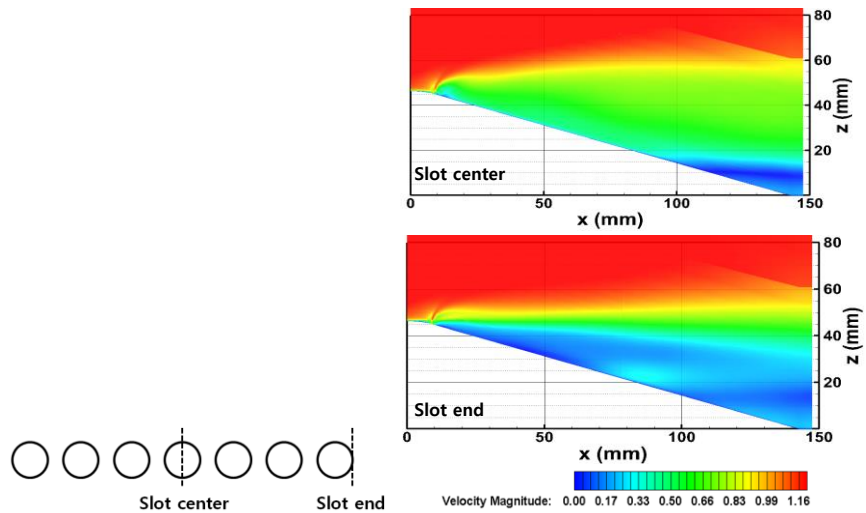


b) Velocity magnitude contours at  $x$ - $z$  plane

**Fig. 4.12 Exit type 2-2 ( $G = 1.5$  mm,  $D=1.5$ mm)**

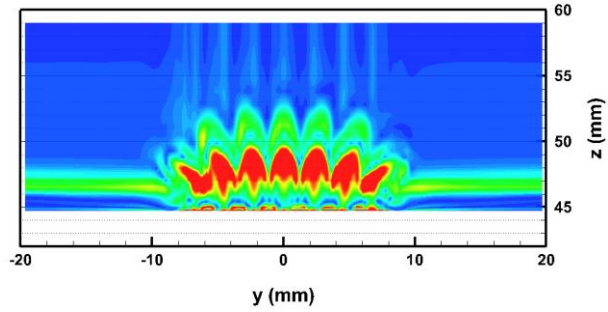


a) Phase-averaged iso- vorticity surface contours

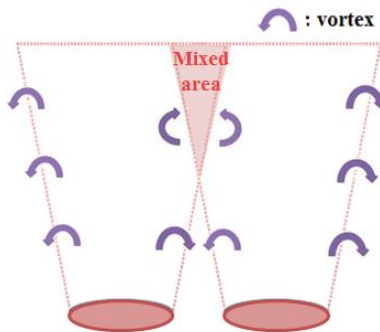


b) Velocity magnitude contours at  $x$ - $z$  plane

Fig. 4.13 Exit type 2-3 ( $G = 3$  mm,  $D=1.5$ mm)

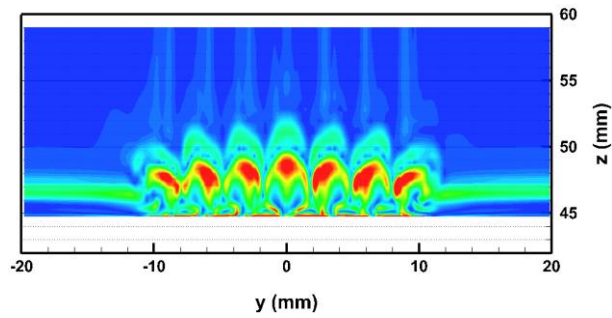


a) Vorticity magnitude

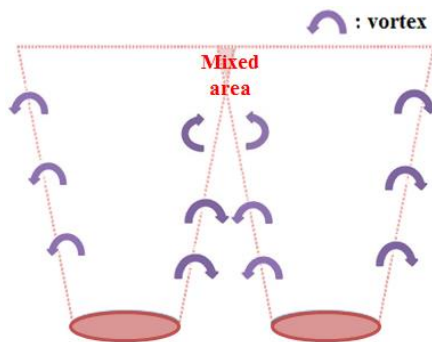


b) Vortex formation schematics

**Fig. 4.14** Phase-averaged vorticity magnitude contours at jet exit and vortex formation schematics (Exit type 2-1 with  $G = 0.75$  mm and  $D=1.5$ mm)

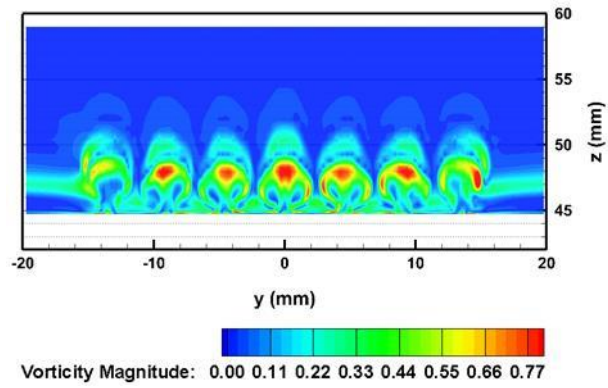


a) Vorticity magnitude

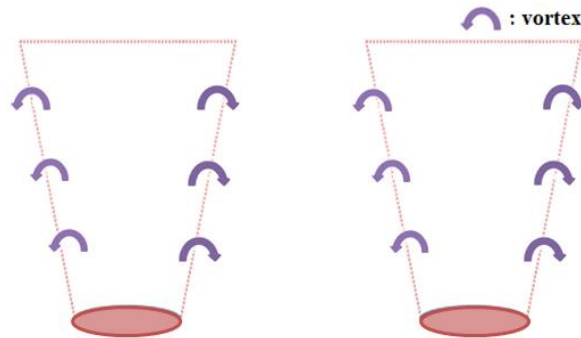


b) Vortex formation schematics

**Fig. 4.15** Phase-averaged vorticity magnitude contours at jet exit and vortex formation schematics (Exit type 2-2 with  $G = 1.5$  mm and  $D=1.5$ mm)



a) Vorticity magnitude



b) Vortex formation schematics

**Fig. 4.16** Phase-averaged vorticity magnitude contours at jet exit and vortex formation schematics (Exit type 2-3 with  $G = 3$  mm,  $D=1.5$ mm )

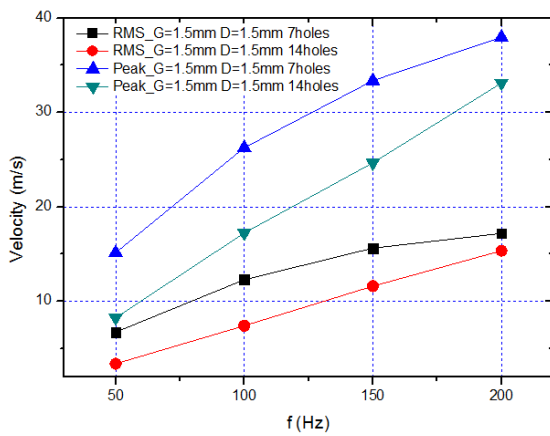
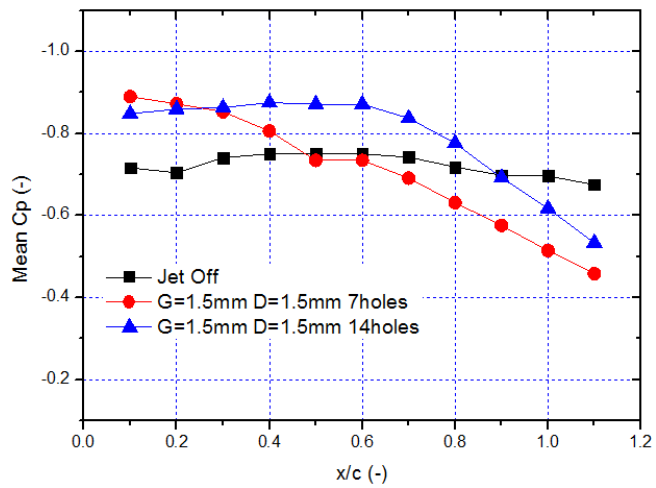
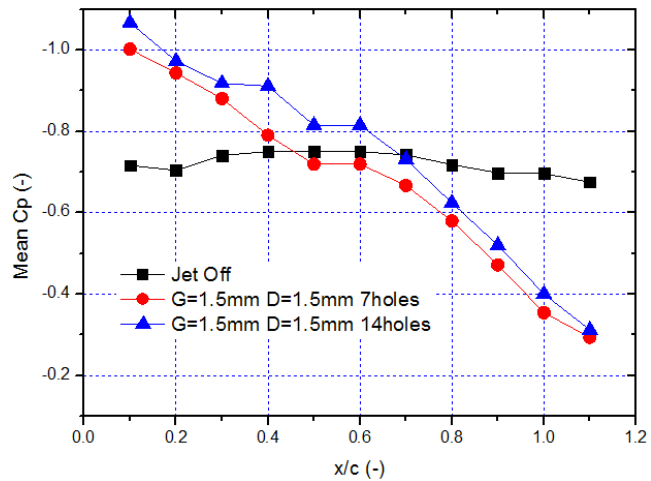


**Fig. 4.17 Jet velocity in the quiescent condition (exit type 2-2 and 3)**

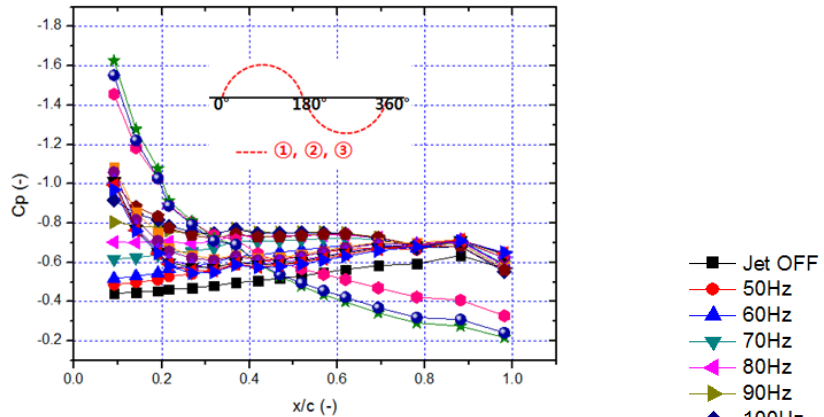


a)  $f = 50 \text{ Hz}$

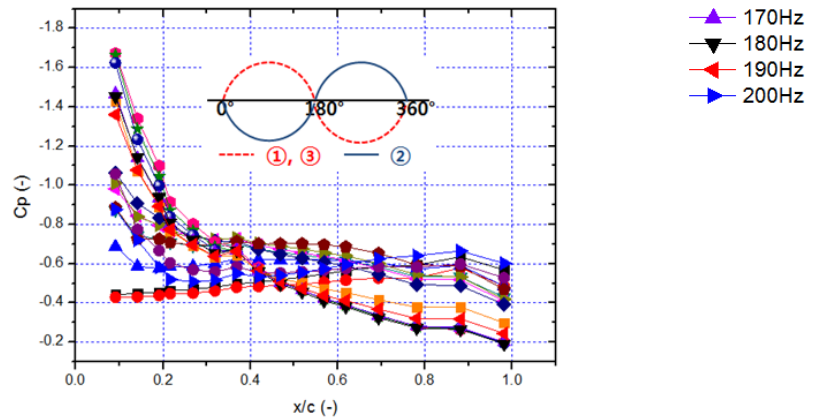


b)  $f = 100 \text{ Hz}$

**Fig. 4.18**  $C_p$  distribution on the rear plate (exit types 2-2 and 3)

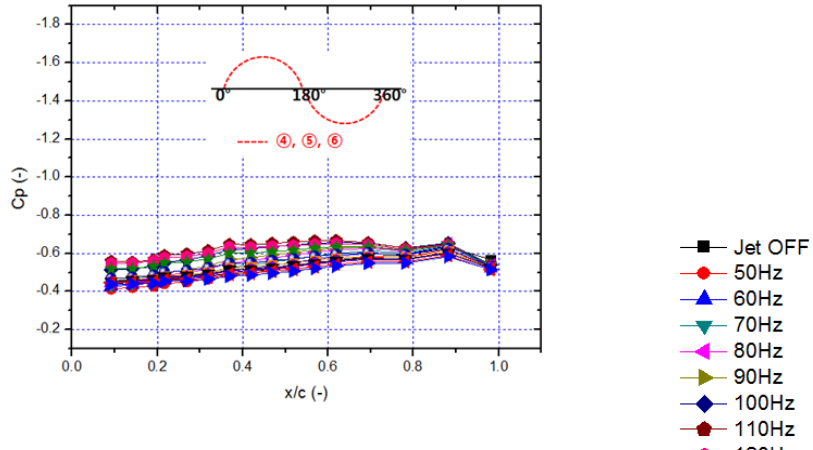


a) Identical phase of all actuators

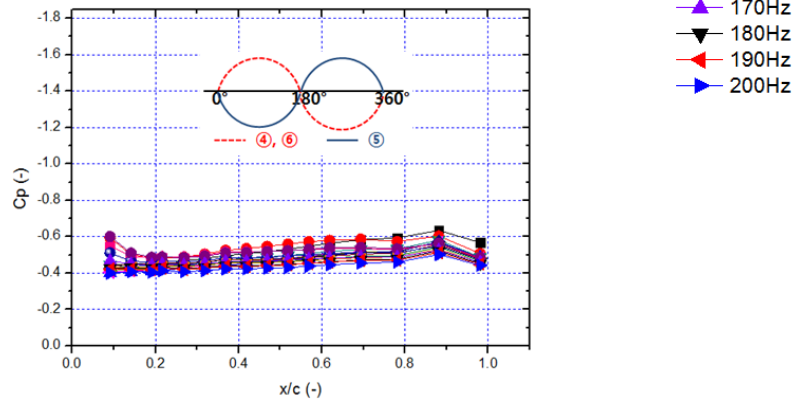


b)  $180^\circ$  phase difference along the spanwise

Fig. 4.19  $C_p$  distribution on the rear plate (1<sup>st</sup> single array,  $x = 8$  mm)

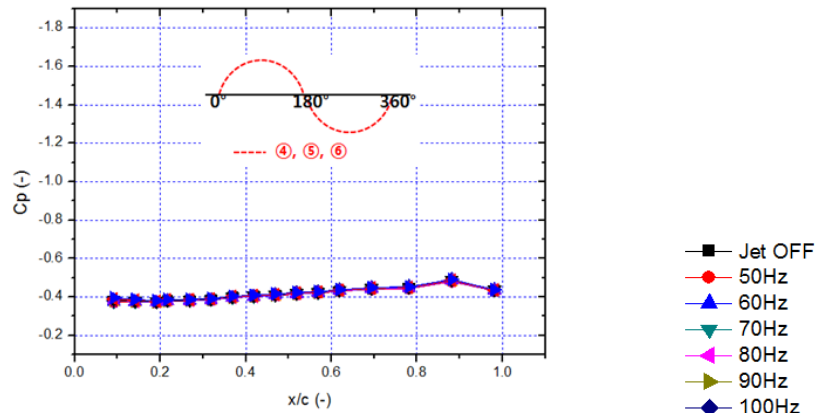


a) Identical phase of all actuators

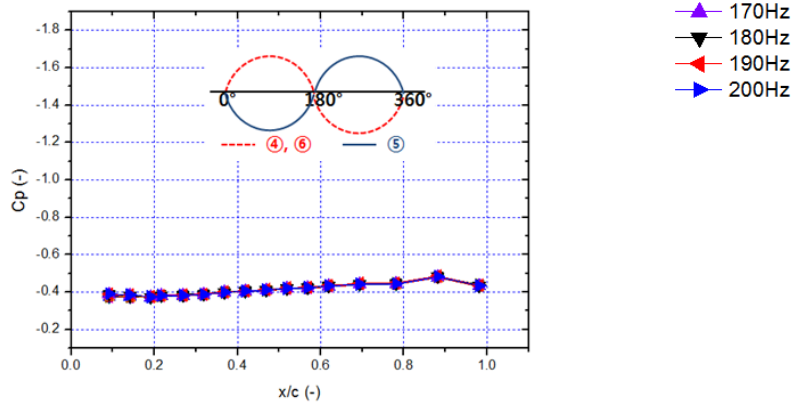


b)  $180^\circ$  phase difference along the spanwise

**Fig. 4.20**  $C_p$  distribution on the rear plate (2<sup>nd</sup> single array,  $x = 21$  mm)

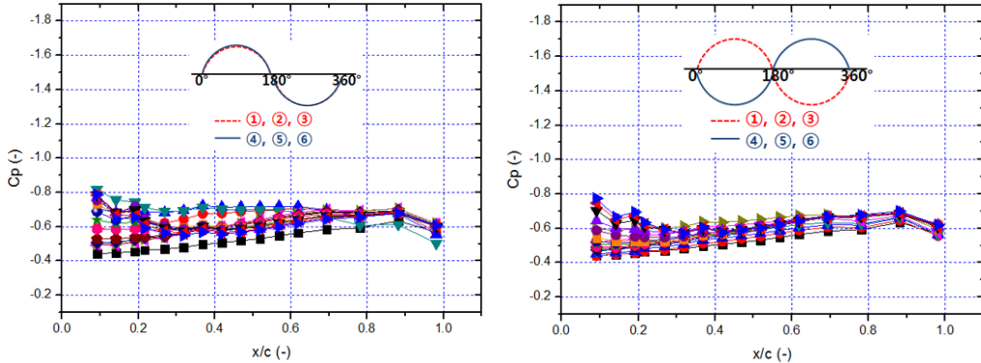


a) Identical phase of all actuators



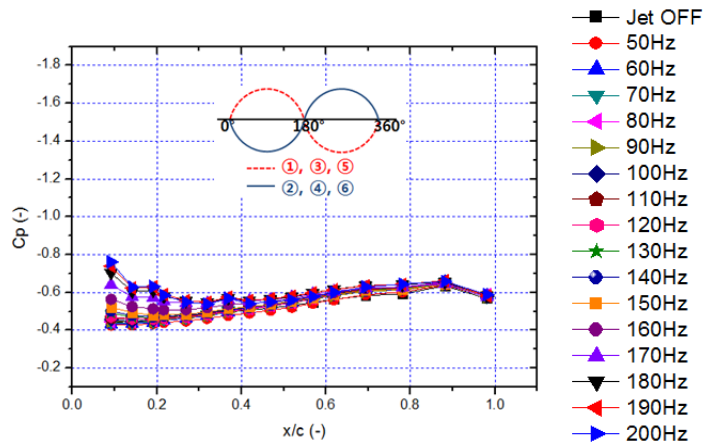
b)  $180^\circ$  phase difference along the spanwise

**Fig. 4.21**  $C_p$  distribution on the rear plate (2<sup>nd</sup> single array,  $x = 50$  mm)



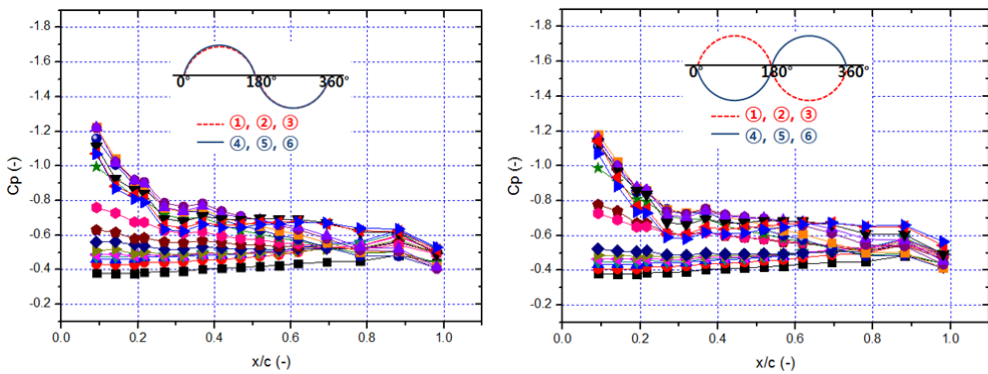
a) Identical phase of all actuators

b)  $180^\circ$  phase difference along the spanwise direction



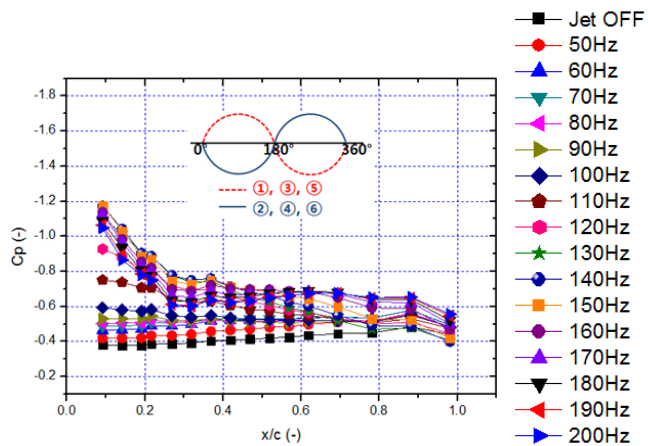
c)  $180^\circ$  phase difference along the chordwise and spanwise direction

Fig. 4.22  $C_p$  distribution on the rear plate (dual array, 13 mm gap)



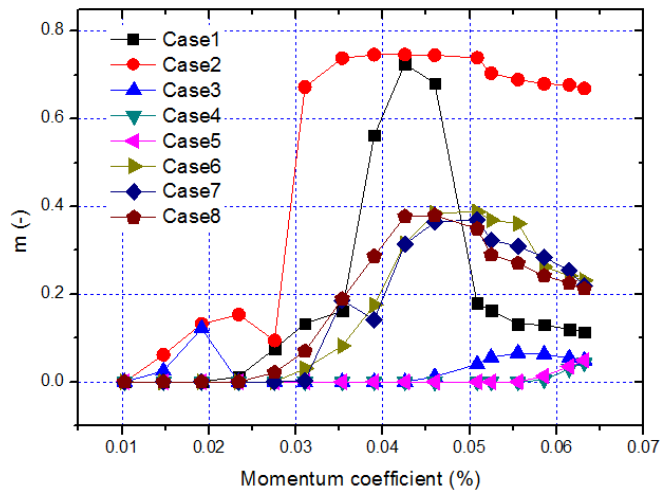
a) Identical phase of all actuators

b)  $180^\circ$  phase difference along the spanwise direction



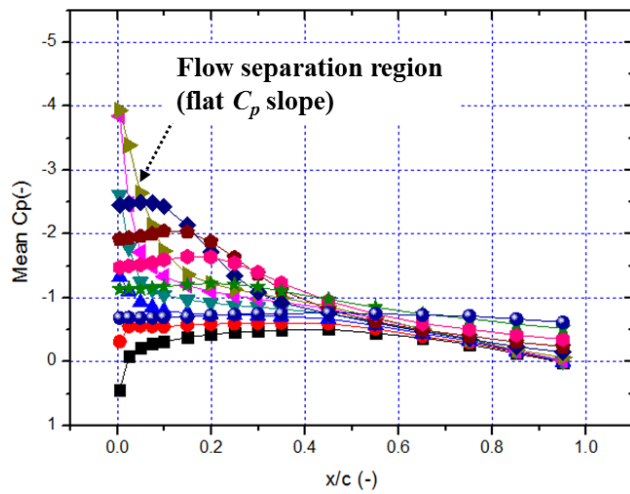
c)  $180^\circ$  phase difference along the chordwise and spanwise direction

Fig. 4.23  $C_p$  distribution on the rear plate (dual array, 42 mm gap)

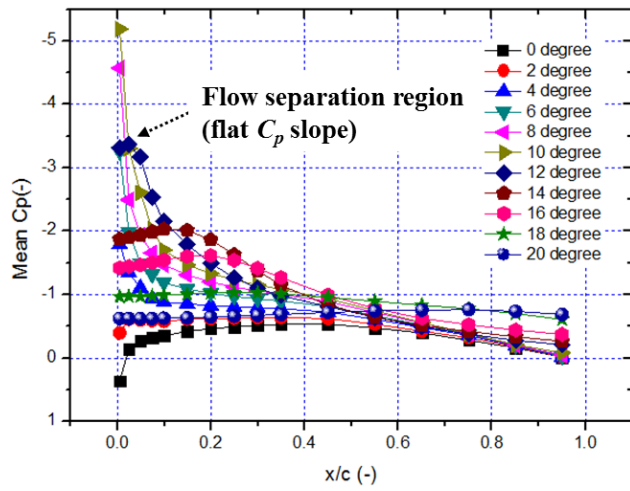


Case	Array type	Phase type
<b>1</b>	Single array	Identical phase of all actuators
<b>2</b>	Single array	<b>180° phase difference along the spanwise direction</b>
<b>3</b>	Dual array (gap 13 mm)	Identical phase of all actuators
<b>4</b>	Dual array (gap 13 mm)	180° phase difference along the chordwise direction
<b>5</b>	Dual array (gap 13 mm)	180° phase difference along the chordwise and spanwise direction
<b>6</b>	<b>Dual array (gap 42 mm)</b>	<b>Identical phase of all actuators</b>
<b>7</b>	Dual array (gap 42 mm)	<b>180° phase difference along the chordwise direction</b>
<b>8</b>	Dual array (gap 42 mm)	<b>180° phase difference along the chordwise and spanwise direction</b>

**Fig. 4.24 Slopes of  $C_p$  curves (m)**



a)  $\text{Re}\# = 6.67 \times 10^5$



b)  $\text{Re}\# = 1.0 \times 10^6$

Fig. 4.25 Mean  $C_p$  on the upper surface of NACA 64A210 (synthetic jet-off)

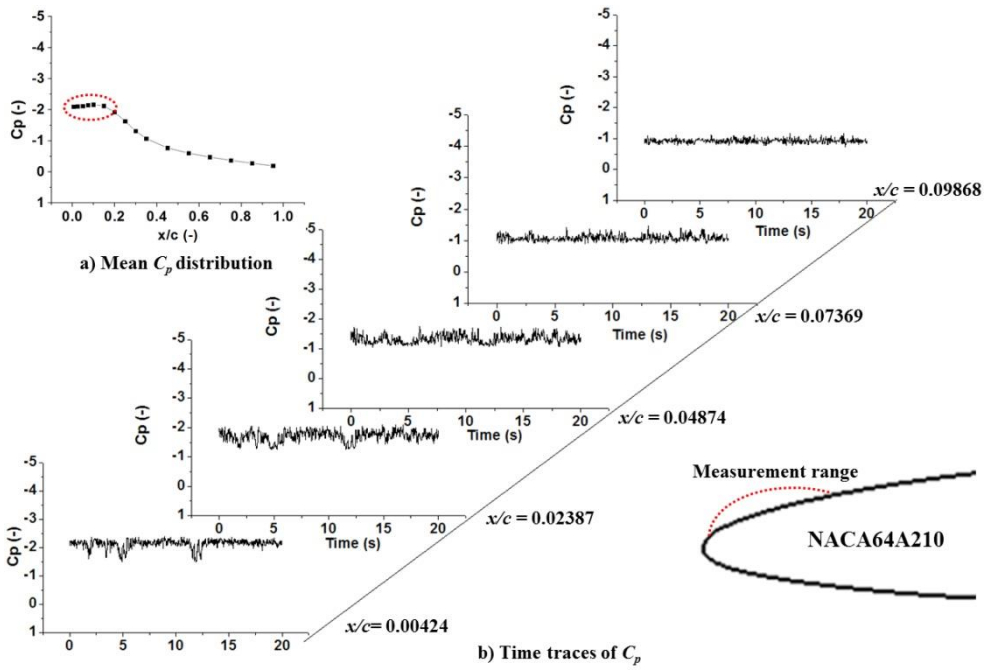
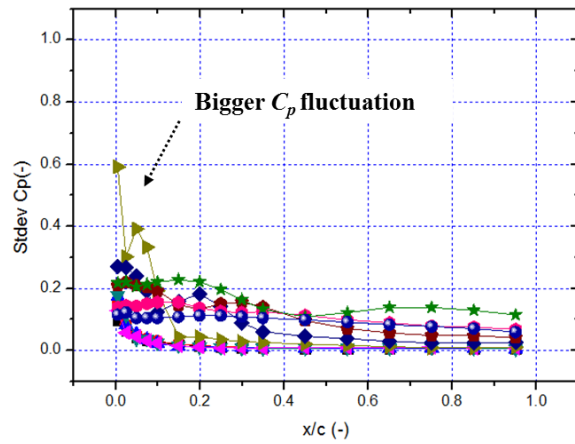
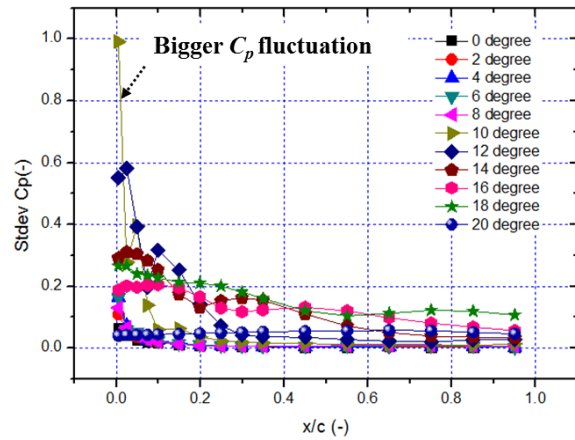


**Fig. 4.26**  $C_p$  distribution near the leading-edge of NACA64A210 ( $\alpha = 12$  degrees,  $Re\# = 6.67 \times 10^5$ )

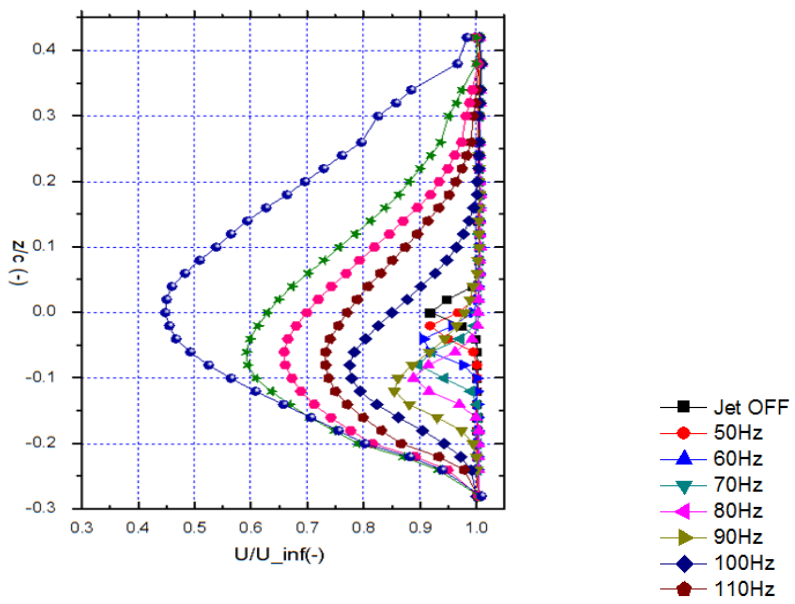


a)  $\text{Re}\# = 6.67 \times 10^5$

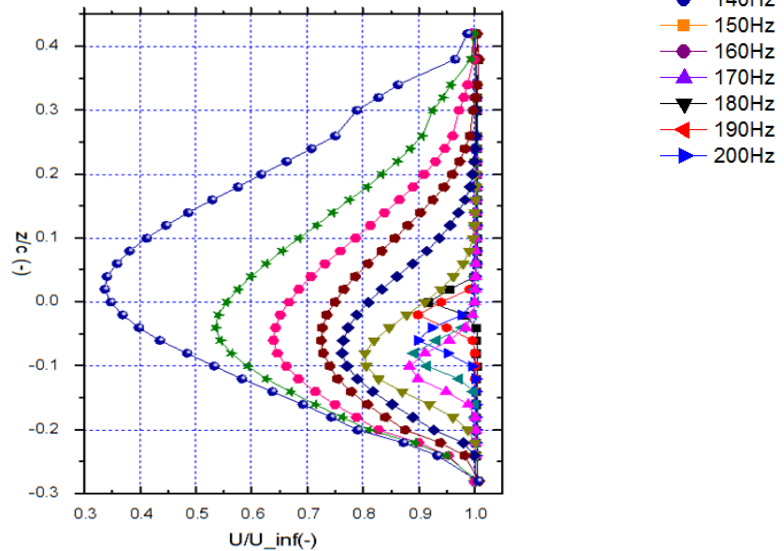


b)  $\text{Re}\# = 1.0 \times 10^6$

**Fig. 4.27 Standard deviation of  $C_p$  on the upper surface of NACA 64A210 (synthetic jet-off)**



a)  $\text{Re}\# = 6.67 \times 10^5$



b)  $\text{Re}\# = 1.0 \times 10^6$

**Fig. 4.28 Wake survey of NACA 64A210 (synthetic jet-off)**

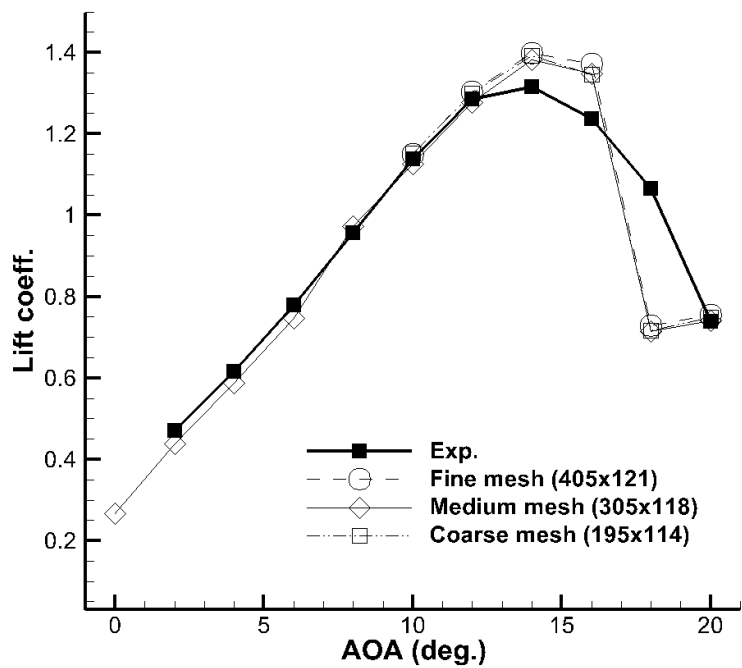
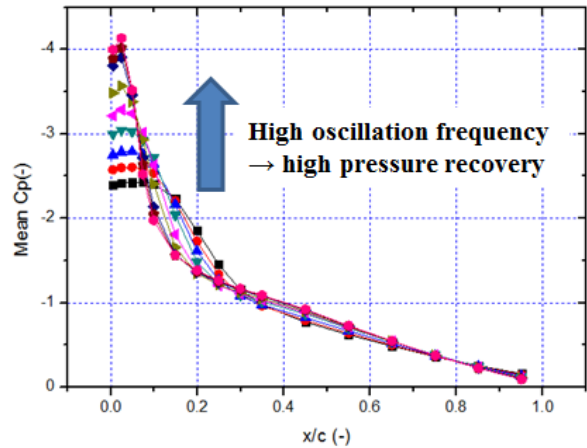
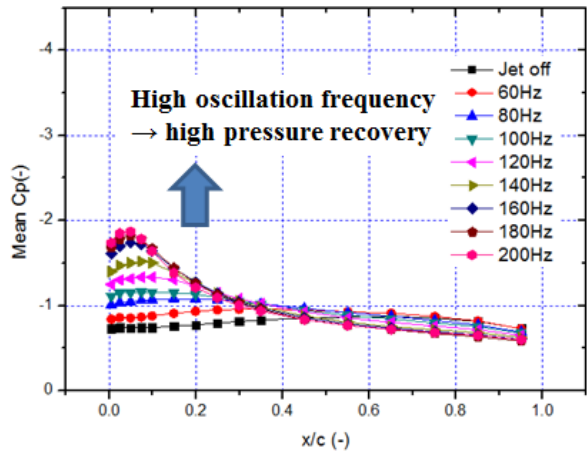


Fig. 4.29 Lift coefficient curve of NACA 64A210 (synthetic jet-off) [83]

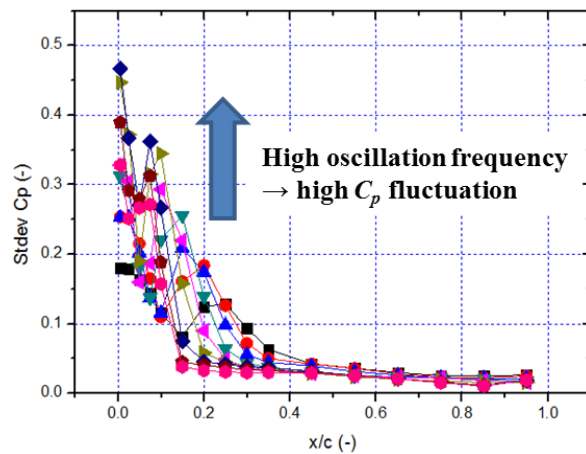


a) Mean  $C_p$  ( $\alpha = 12$  degrees)

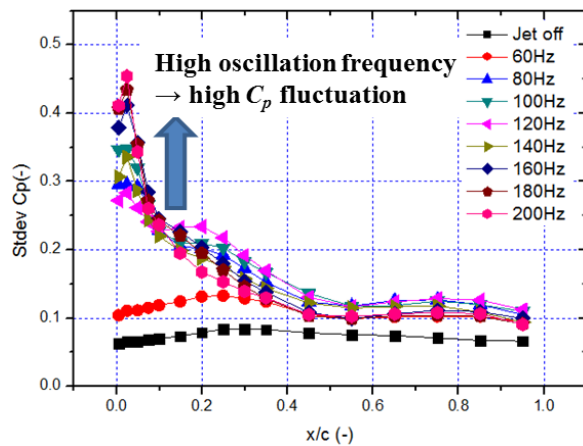


b) Mean  $C_p$  ( $\alpha = 20$  degrees)

Fig. 4.30 Effects of oscillation frequency ( $Re\# = 6.67 \times 10^5$ , 1<sup>st</sup> array actuation)

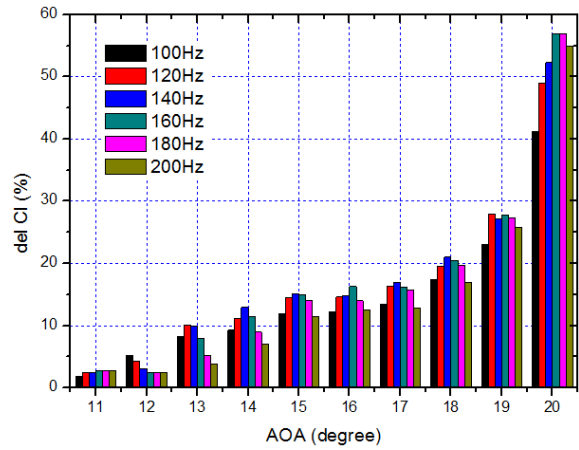


a) Standard deviation of  $C_p$  ( $\alpha = 12$  degrees)

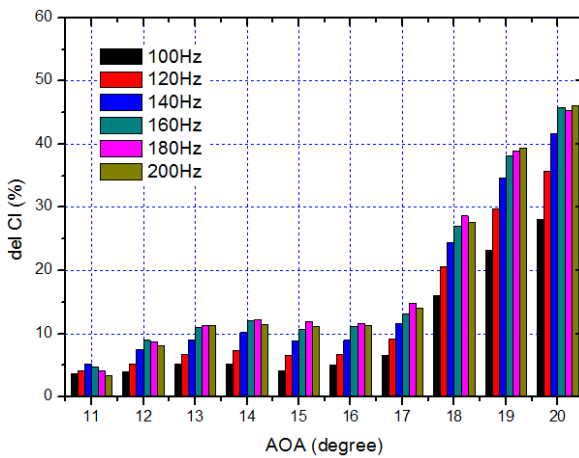


b) Standard deviation of  $C_p$  ( $\alpha = 20$  degrees)

Fig. 4.31 Effects of oscillation frequency ( $Re\# = 6.67 \times 10^5$ , 1<sup>st</sup> array actuation)

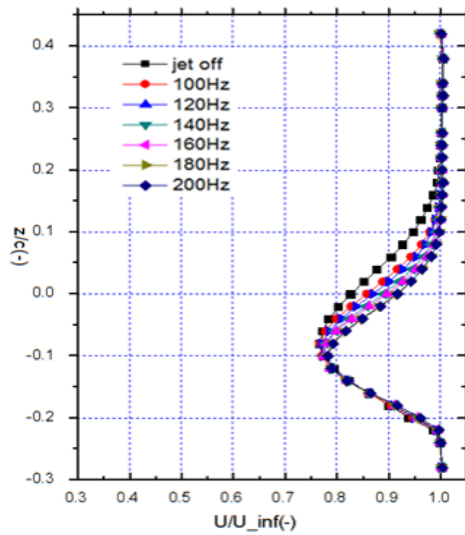


a)  $Re\# = 6.67 \times 10^5$

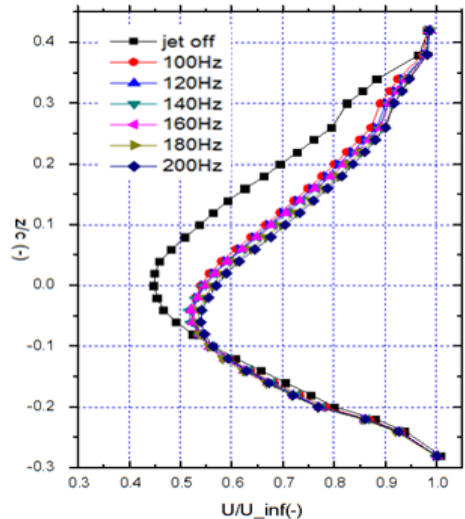


b)  $Re\# = 1.0 \times 10^6$

Fig. 4.32 Increment of lift according to the angle of attack (1<sup>st</sup> array actuation)

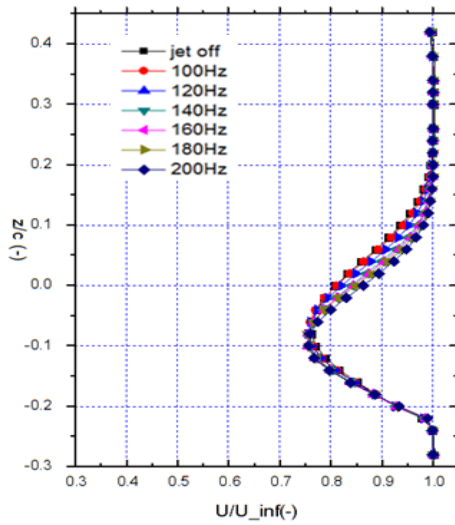


a)  $\alpha = 12$  degrees,  $\text{Re}\# = 6.67 \times 10^5$

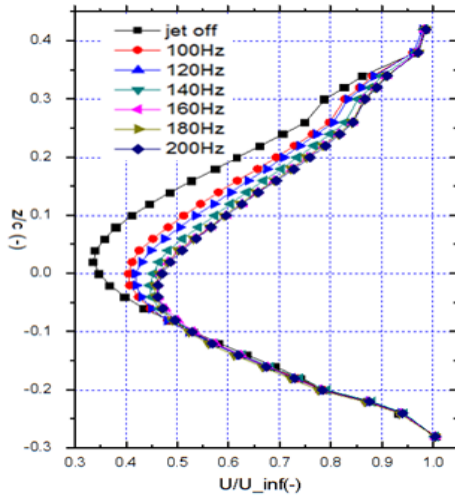


b)  $\alpha = 20$  degrees,  $\text{Re}\# = 6.67 \times 10^5$

**Fig. 4.33 Wake region depending on oscillation frequency (1<sup>st</sup> array actuation)**

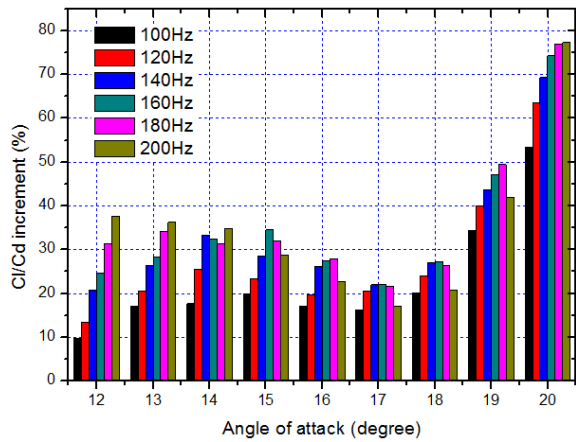


a)  $\alpha = 12$  degrees,  $\text{Re}\# = 1.0 \times 10^6$

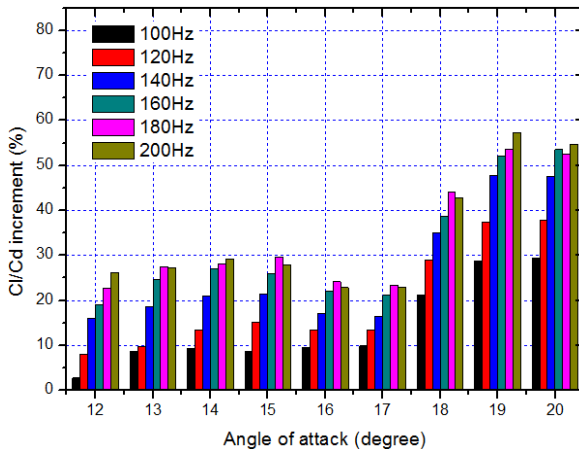


b)  $\alpha = 20$  degrees,  $\text{Re}\# = 1.0 \times 10^6$

**Fig. 4.34 Wake region depending on oscillation frequency (1<sup>st</sup> array actuation)**

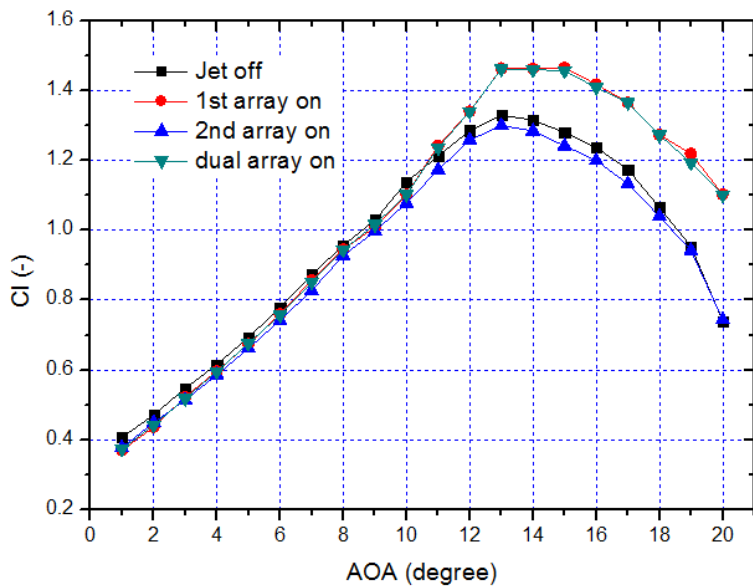


a)  $Re\# = 6.67 \times 10^5$

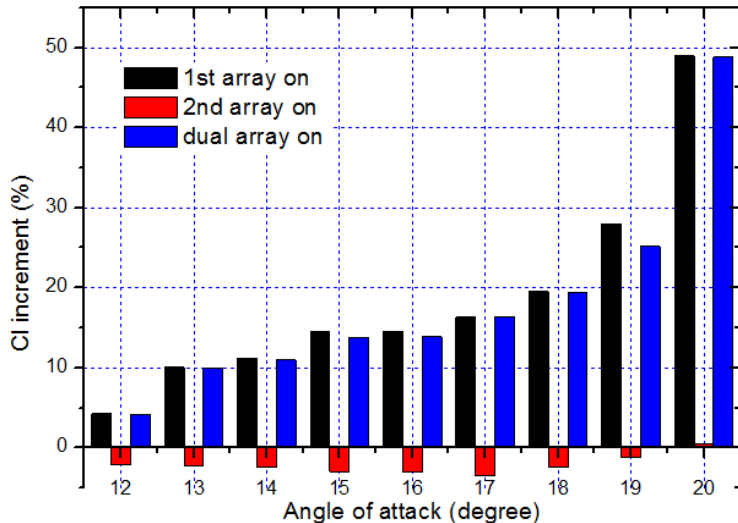


b)  $Re\# = 1.0 \times 10^6$

**Fig. 4.35 Increment of lift-to-drag ratio depending on the angle of attack  
(1<sup>st</sup> array actuation)**

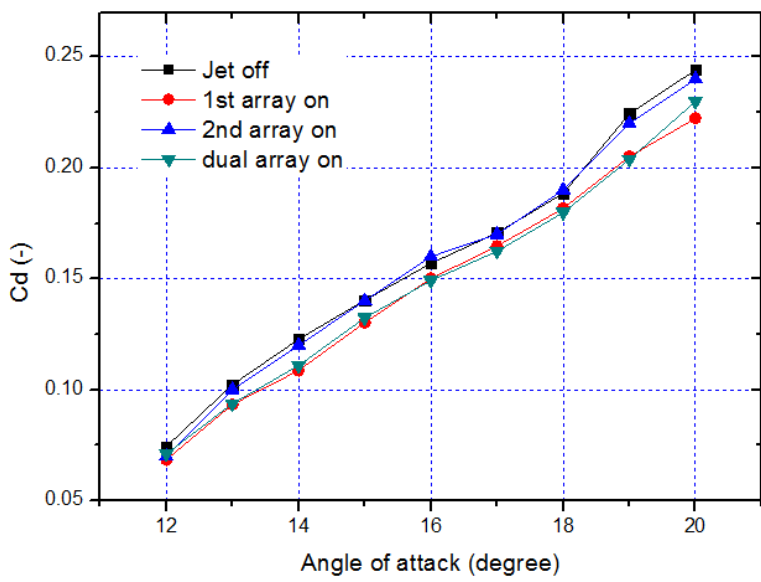


a) Lift coefficient

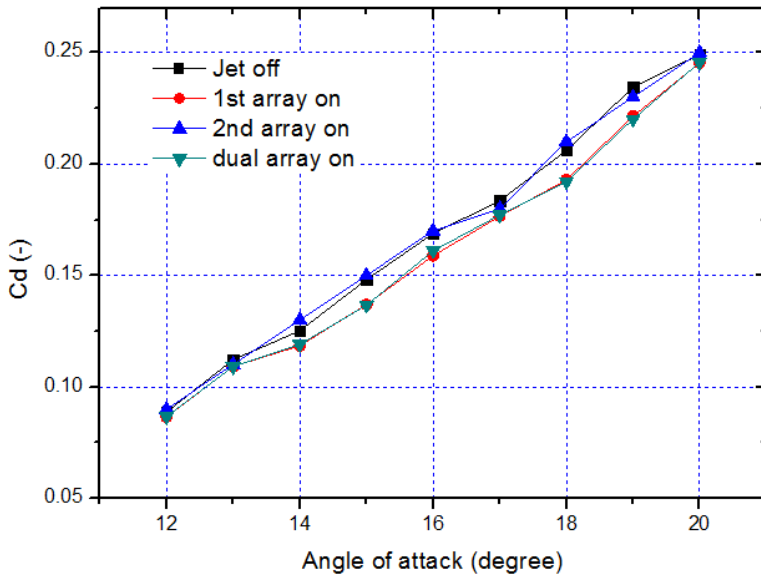


b) Increment of lift coefficient

Fig. 4.36 Lift coefficient depending on array type ( $Re\# = 6.67 \times 10^5$ ,  $f = 120$  Hz)

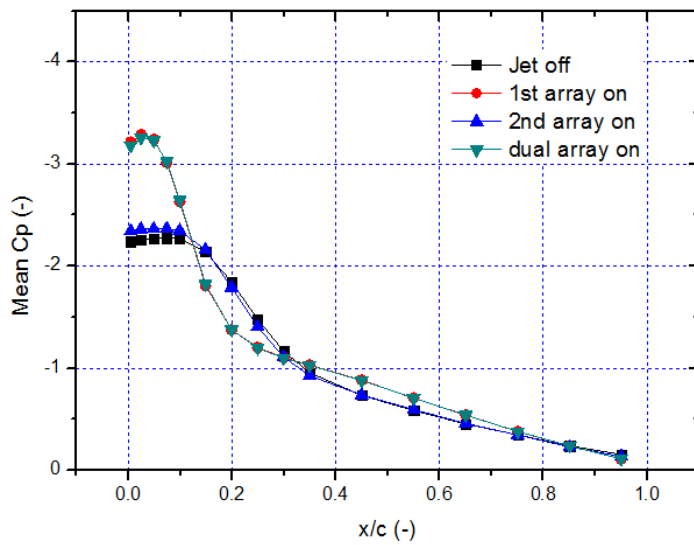


a)  $Re\# = 6.67 \times 10^5$

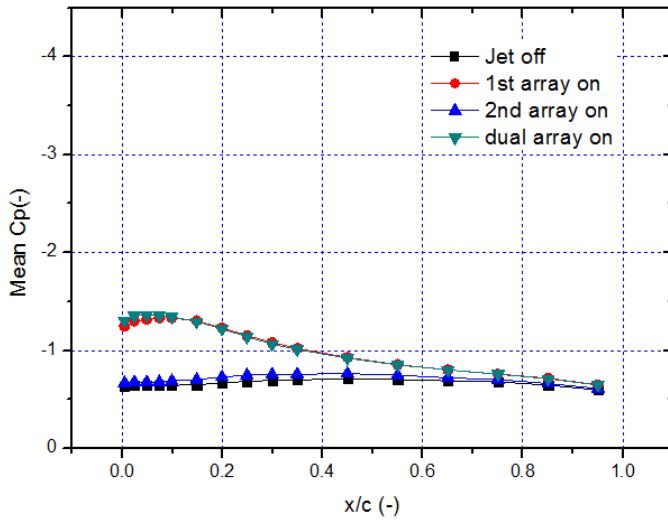


b)  $Re\# = 1.0 \times 10^6$

**Fig. 4.37 Drag reduction by synthetic jet ( $f = 120$  Hz)**

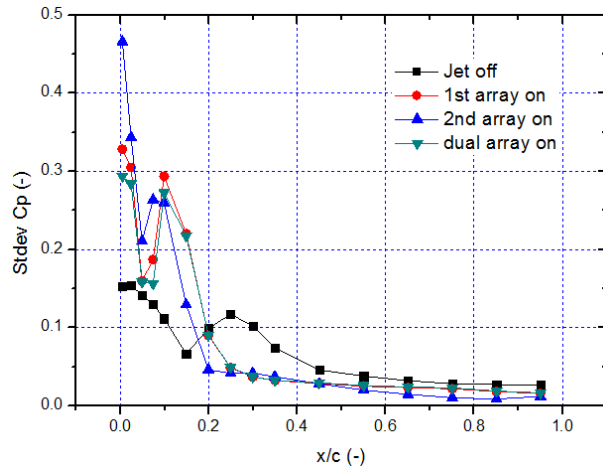


a) Mean  $C_p$  ( $\alpha = 12$  degrees)

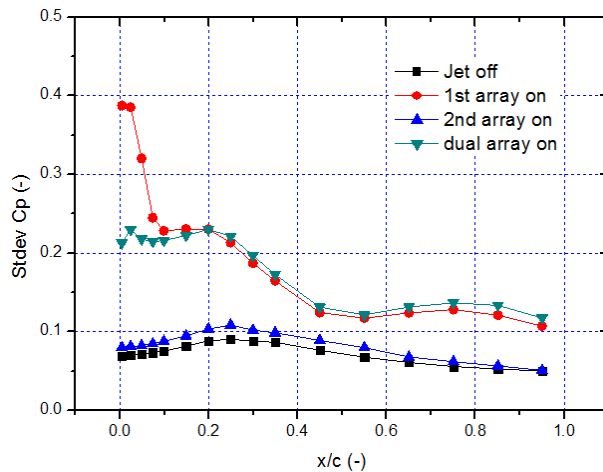


b) Mean  $C_p$  ( $\alpha = 20$  degrees)

**Fig. 4.38**  $C_p$  distribution depending on array type ( $Re\# = 6.67 \times 10^5, f = 120$  Hz)

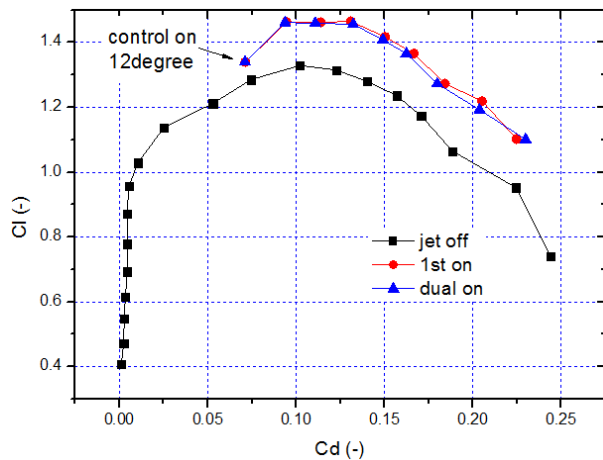


a) Standard deviation of  $C_p$  ( $\alpha = 12$  degrees)

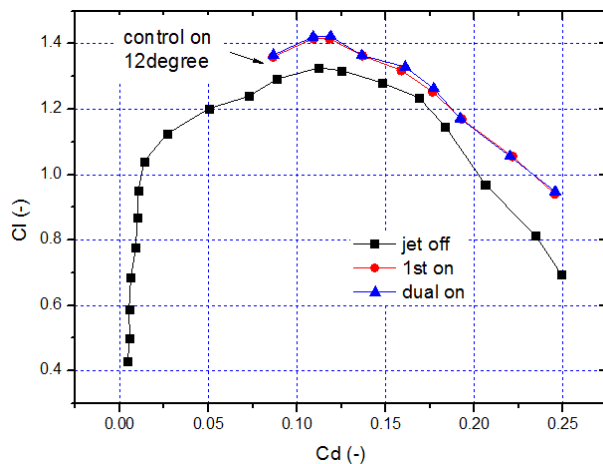


b) Standard deviation of  $C_p$  ( $\alpha = 20$  degrees)

Fig. 4.39  $C_p$  distribution depending on array type ( $Re\# = 6.67 \times 10^5, f = 120$  Hz)



a)  $\text{Re}\# = 6.67 \times 10^5$



b)  $\text{Re}\# = 1.0 \times 10^6$

Fig. 4.40 Drag polar curve of NACA 64A210 ( $f = 120$  Hz)

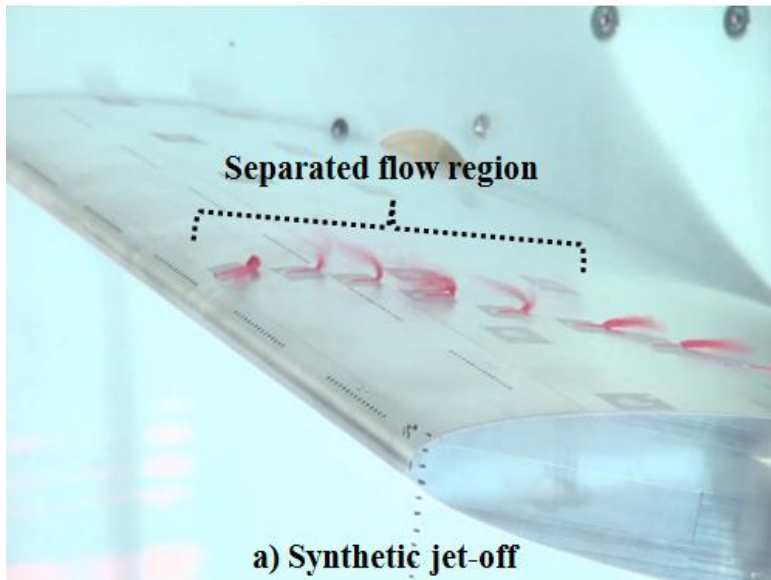


**Fig. 4.41** Tuft visualization of flow separation control ( $\alpha = 12$  degrees,  $Re\# = 6.67 \times 10^5$ ,  $f = 120$  Hz)

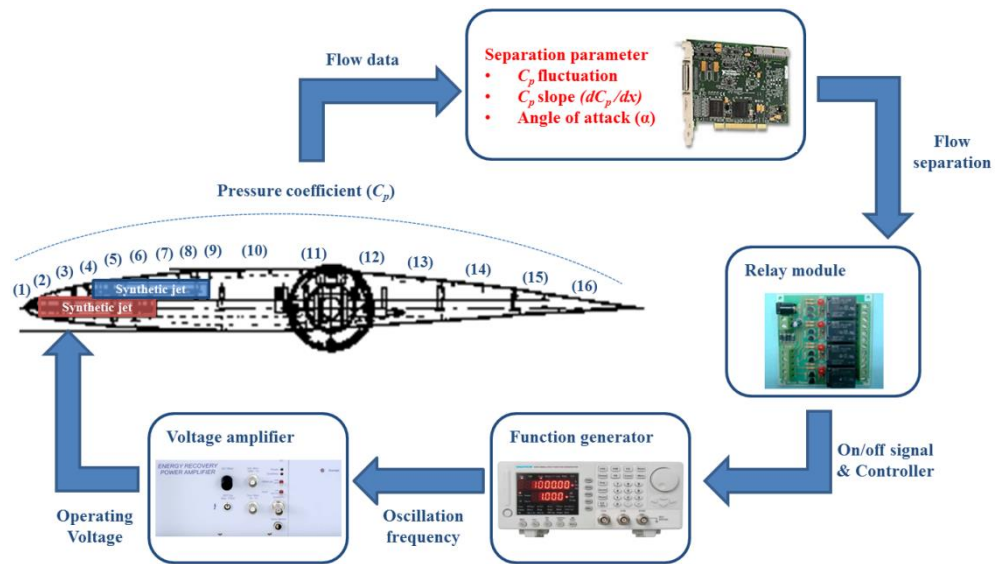


**Fig. 4.42 Schematic of closed-loop control**

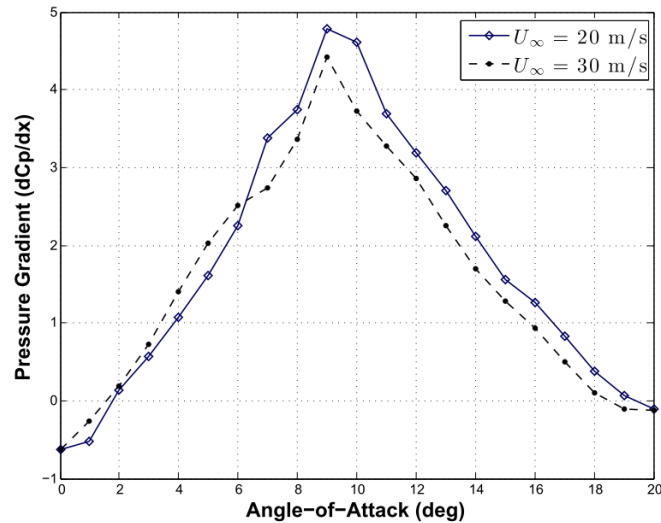


**Fig. 4.43 Pressure gradient according to AOA  
(synthetic jet-off)**

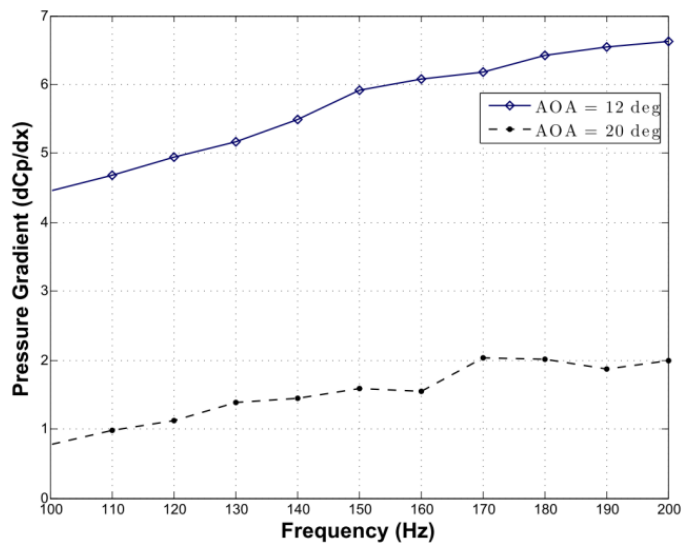
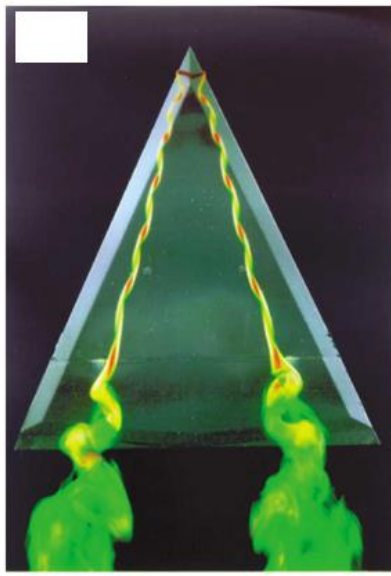
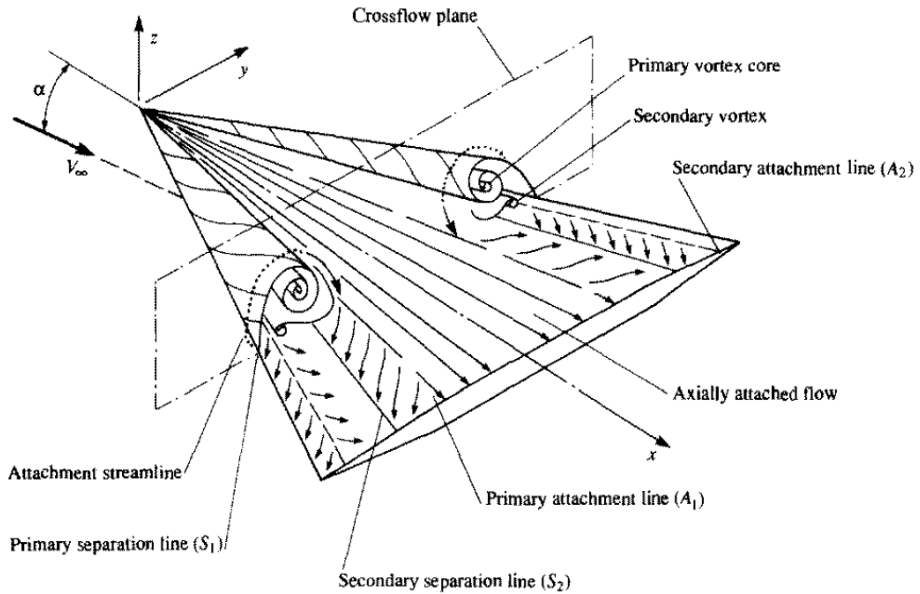


**Fig. 4.44 Pressure gradient according to frequency  
(synthetic jet-on)**



a) Flow visualization by dye emission at the apex [70]



b) Schematic of subsonic flow field over the top of a delta wing [89]

Fig. 4.45 Flow structure on a delta wing

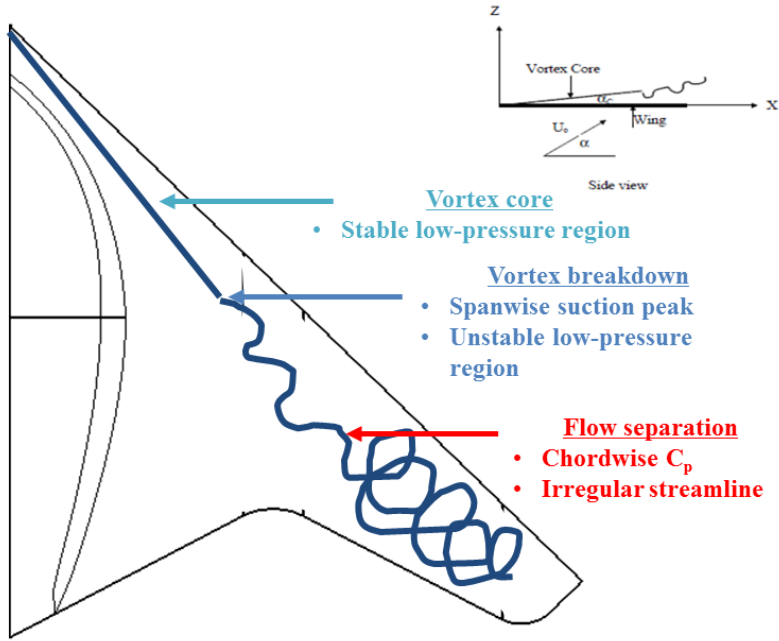


**Fig. 4.46 spatial location of the vortex core and the vortex breakdown location**

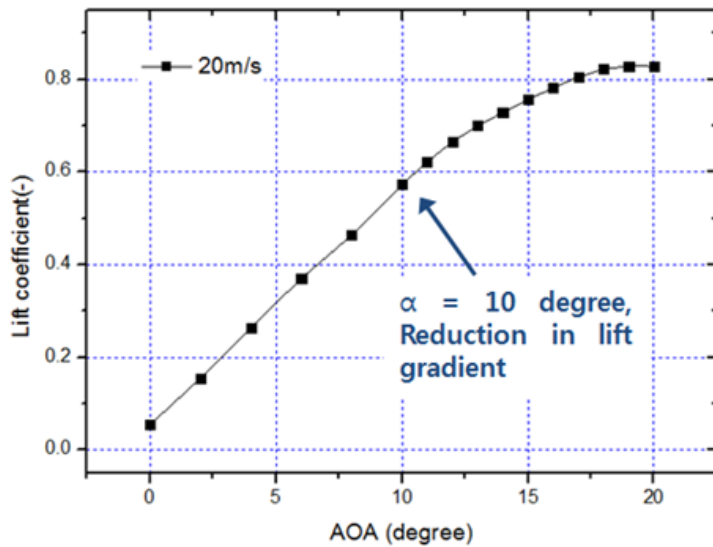


**Fig. 4.47 Lift coefficient curve**

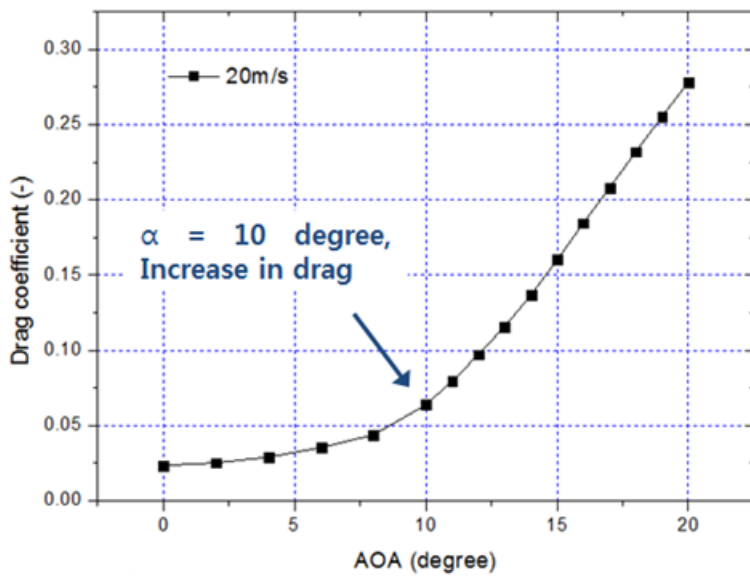


Fig. 4.48 Drag coefficient curve

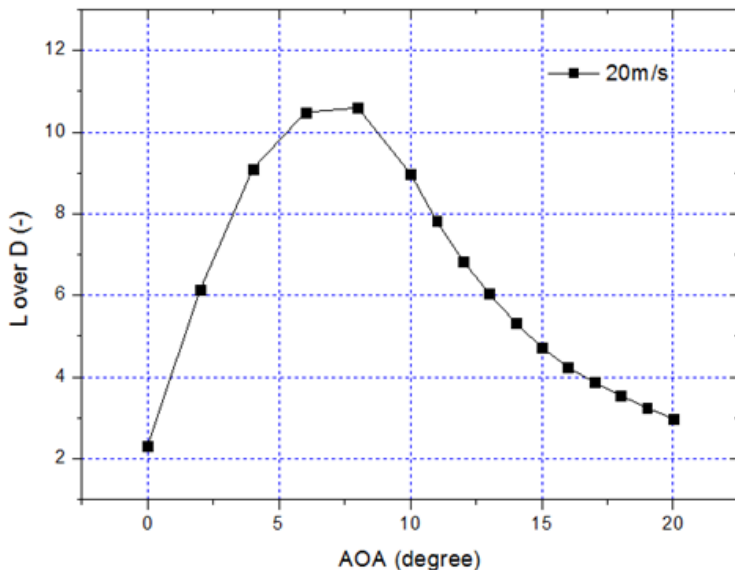


Fig. 4.49 Lift-to-drag ratio curve

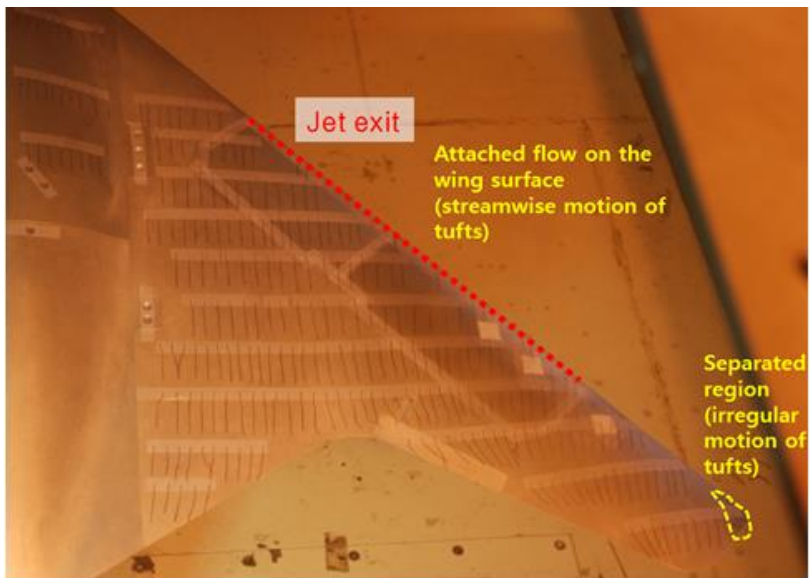


Fig. 4.50 Tufts visualization ( $\alpha = 8$  degrees)

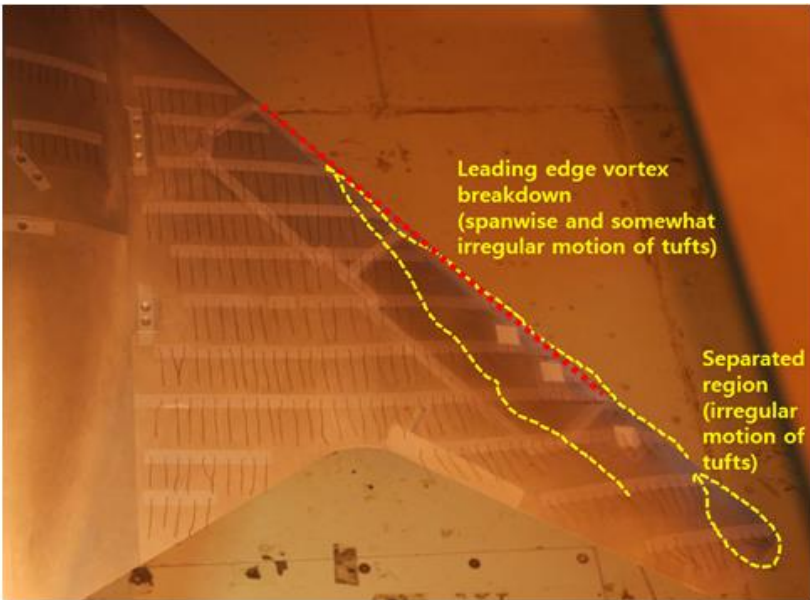
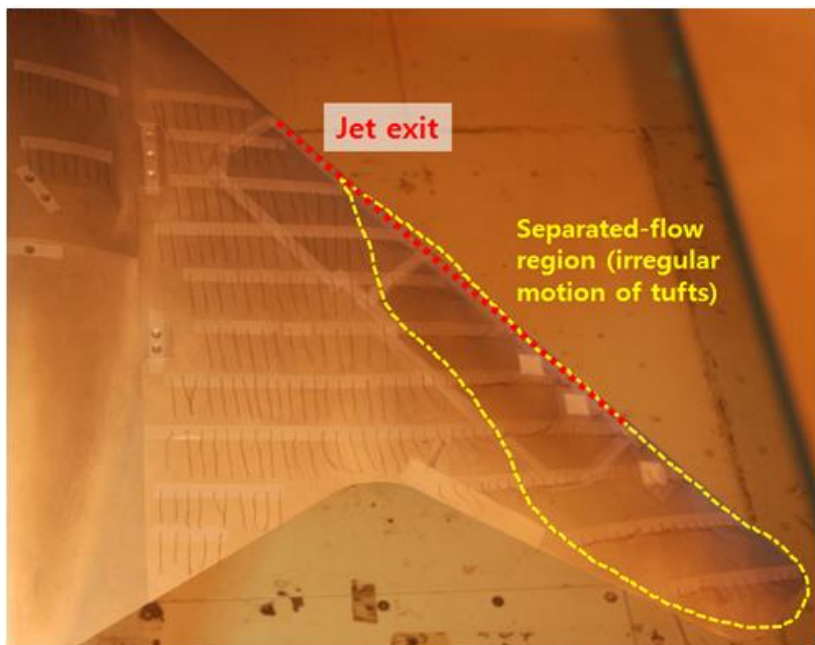
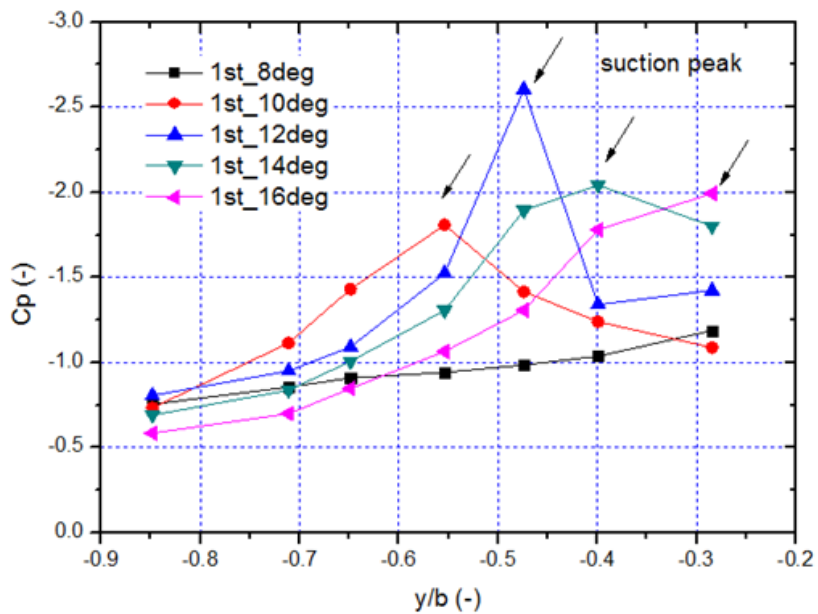


Fig. 4.51 Tufts visualization ( $\alpha = 10$  degrees)



**Fig. 4.52** Tufts visualization ( $\alpha = 12$  degrees)



**Fig. 4.53** Spanwise  $C_p$  distribution (1<sup>st</sup> line)

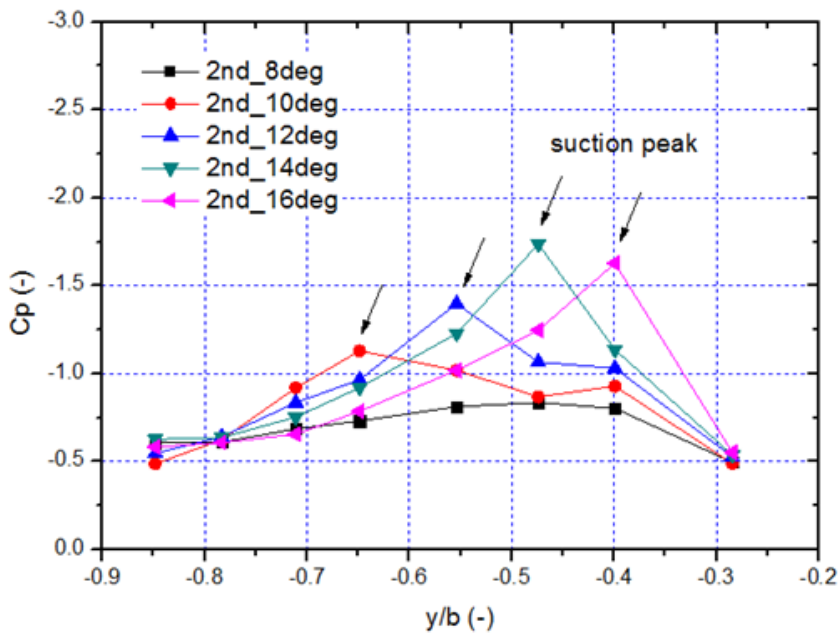


Fig. 4.54 Spanwise  $C_p$  distribution (2<sup>nd</sup> line)

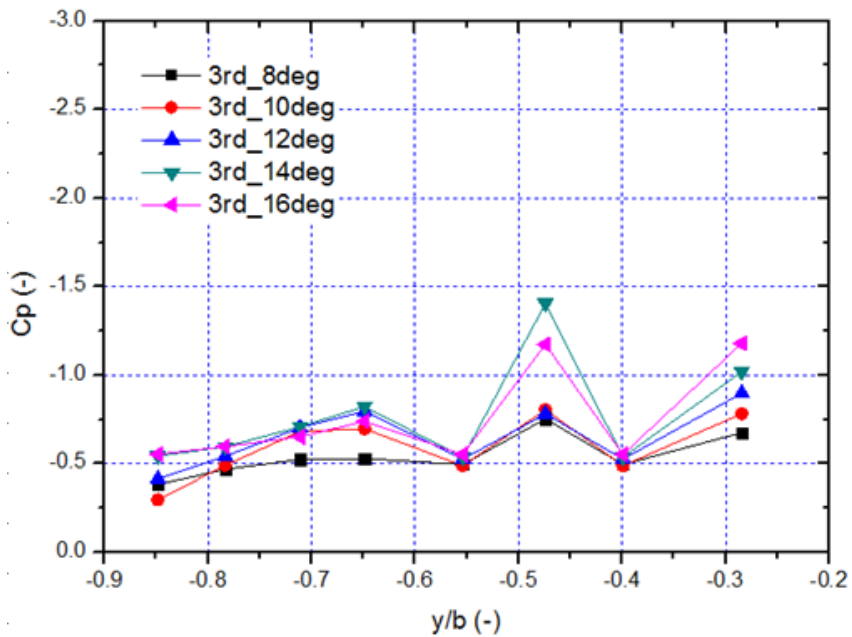
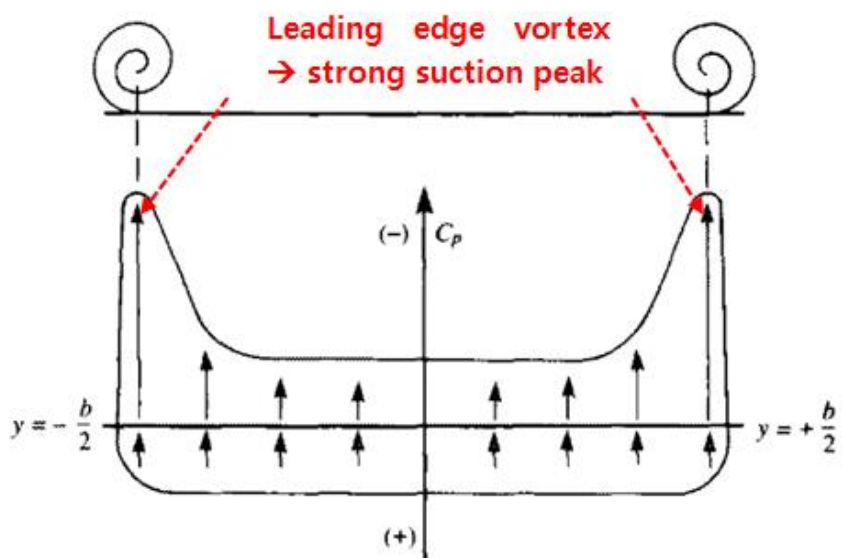
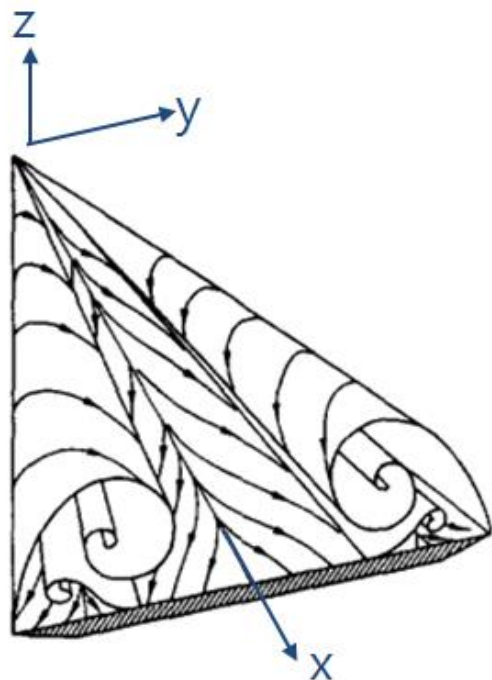
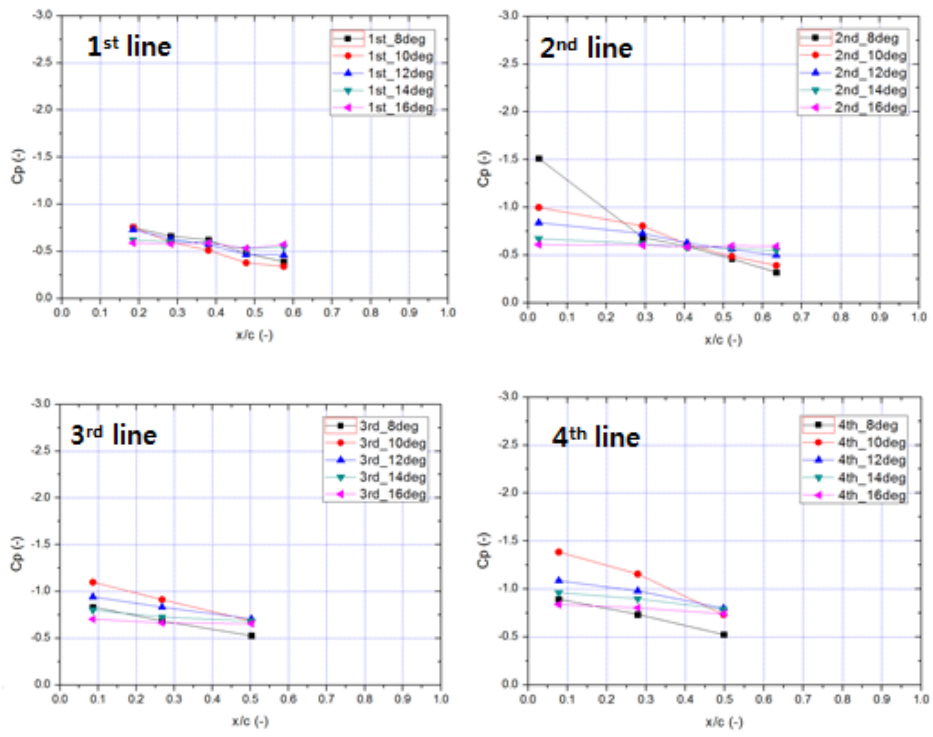


Fig. 4.55 Spanwise  $C_p$  distribution (3<sup>rd</sup> line)



**Fig. 4.56 Spanwise  $C_p$  distribution across a delta wing [89]**



**Fig. 4.57 Chordwise  $C_p$  distribution on the blended wing body (1<sup>st</sup> – 4<sup>th</sup> line)**

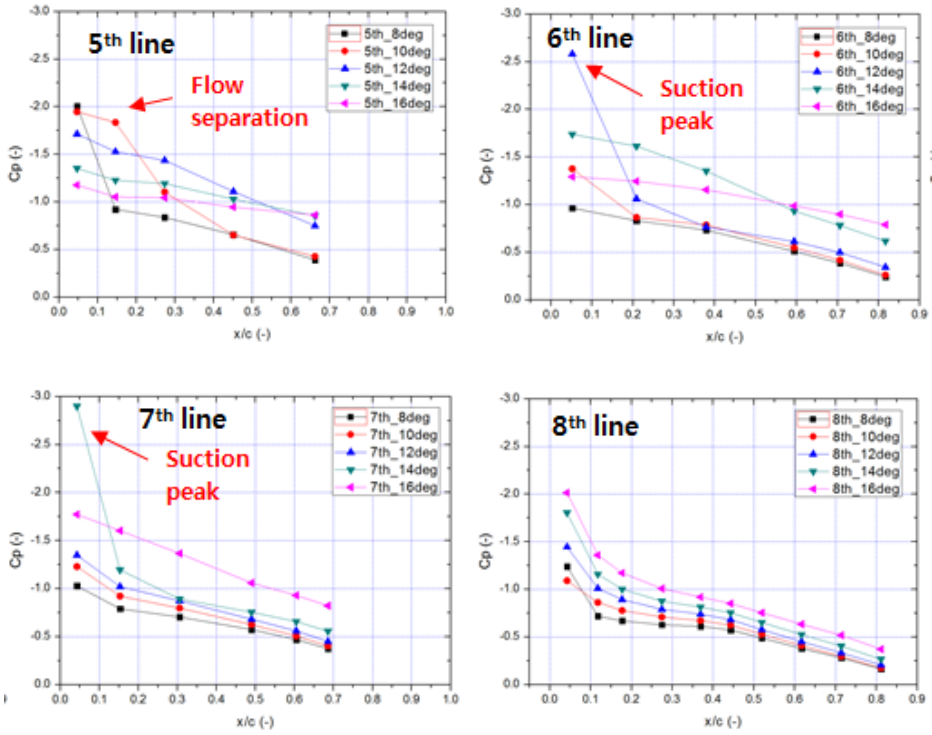
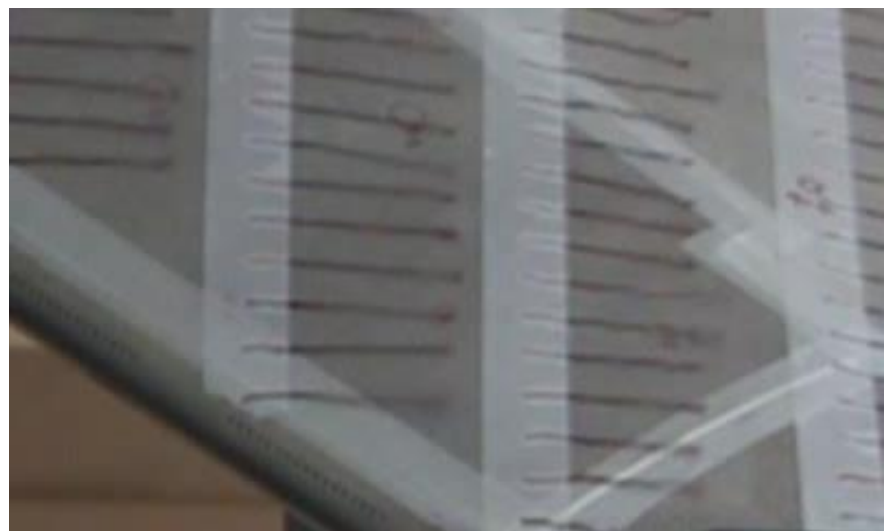


Fig. 4.58 Chordwise  $C_p$  distribution on the blended wing body (5<sup>th</sup> – 8<sup>th</sup> line)



a) Synthetic jet-off



b) Synthetic jet-on

**Fig. 4.59** Tuft visualization of flow separation control ( $\alpha = 12$  degrees,  $Re\# = 1.59 \times 10^6$ ,  $f = 200$  Hz)

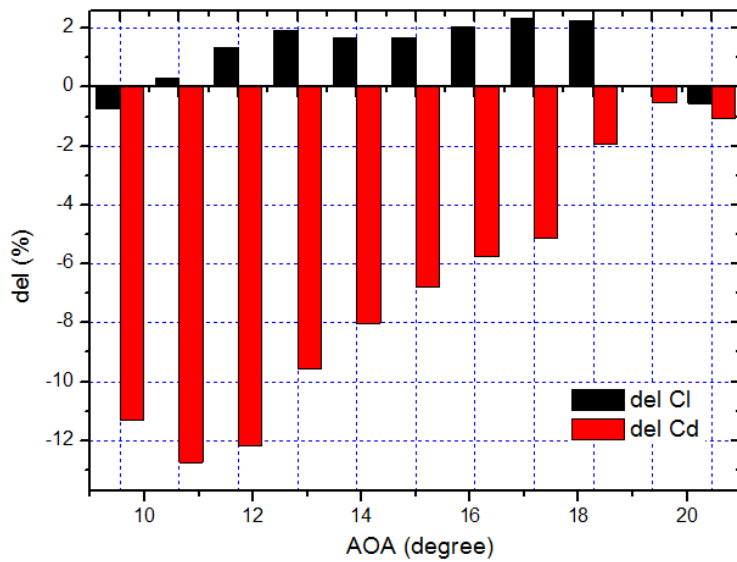


**Fig. 4.60 Increment of  $C_l$  and decrement of  $C_d$  in the stall regime**

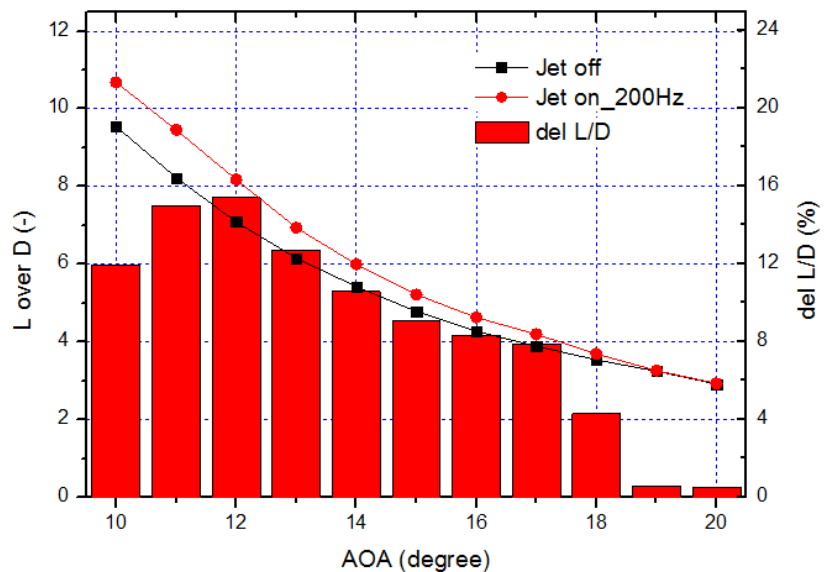


**Fig. 4.61 Comparison of  $C_l/C_d$  curve and increment of  $C_l/C_d$**

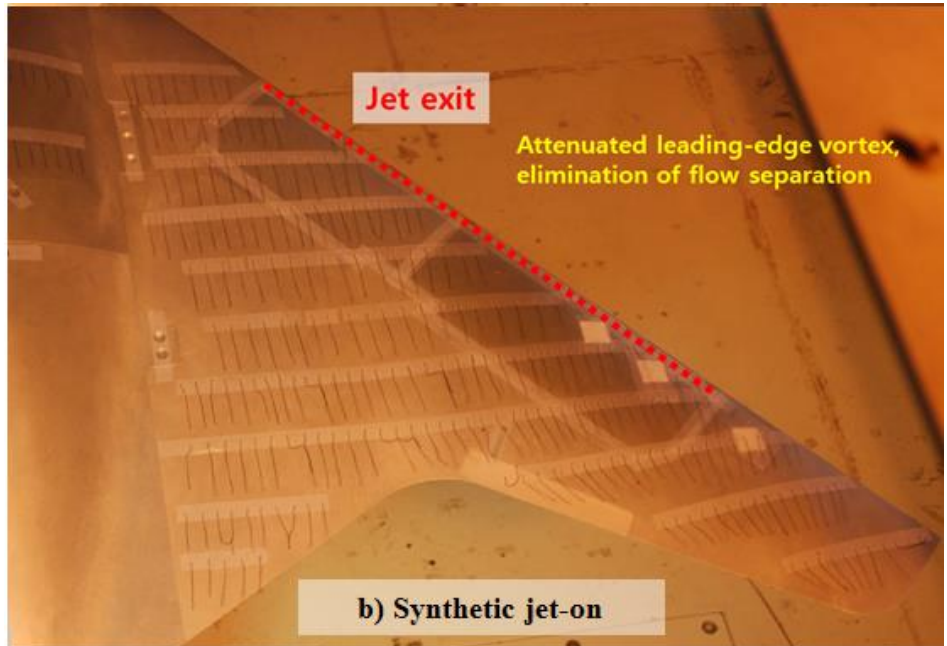
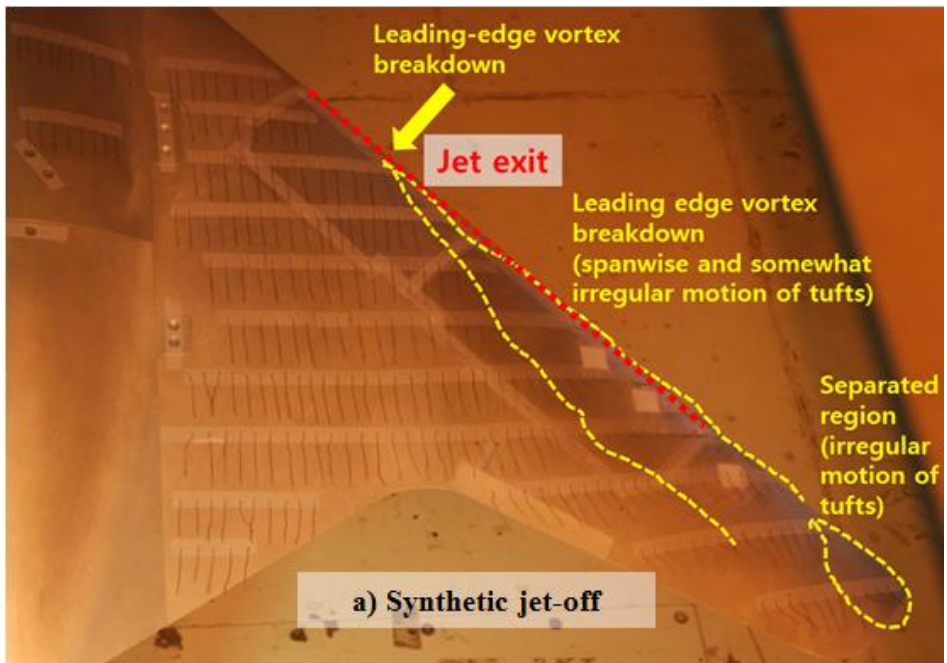


Fig. 4.62 Qualitative effect of synthetic jet ( $\alpha = 10$  degrees)

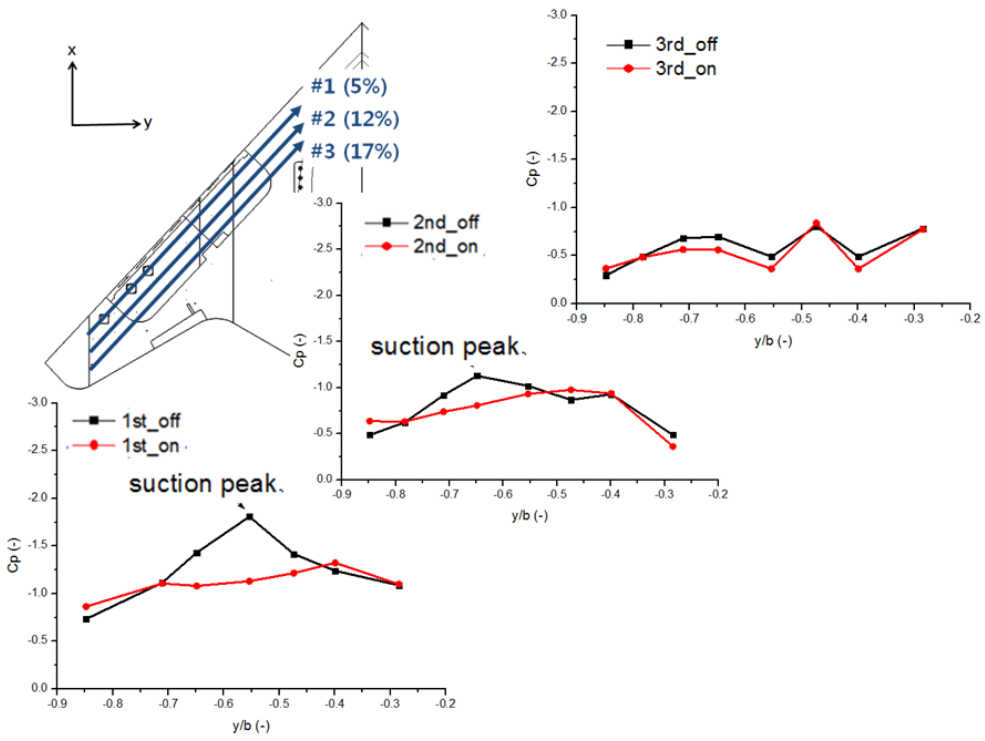
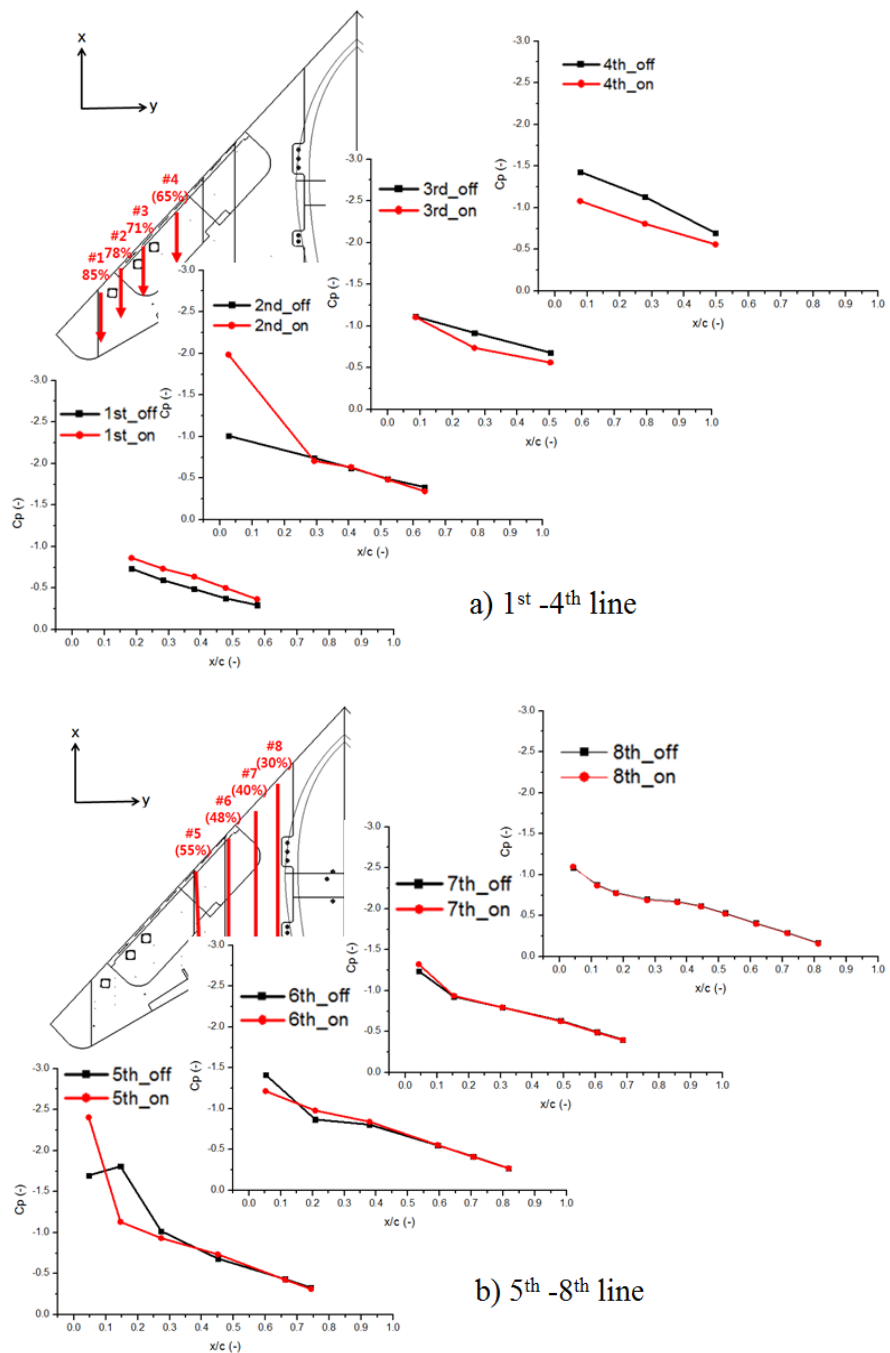


Fig. 4.63 Spanwise  $C_p$  distribution ( $\alpha = 10$  degrees)



**Fig. 4.64 Chordwise  $C_p$  distribution ( $\alpha = 10$  degrees)**

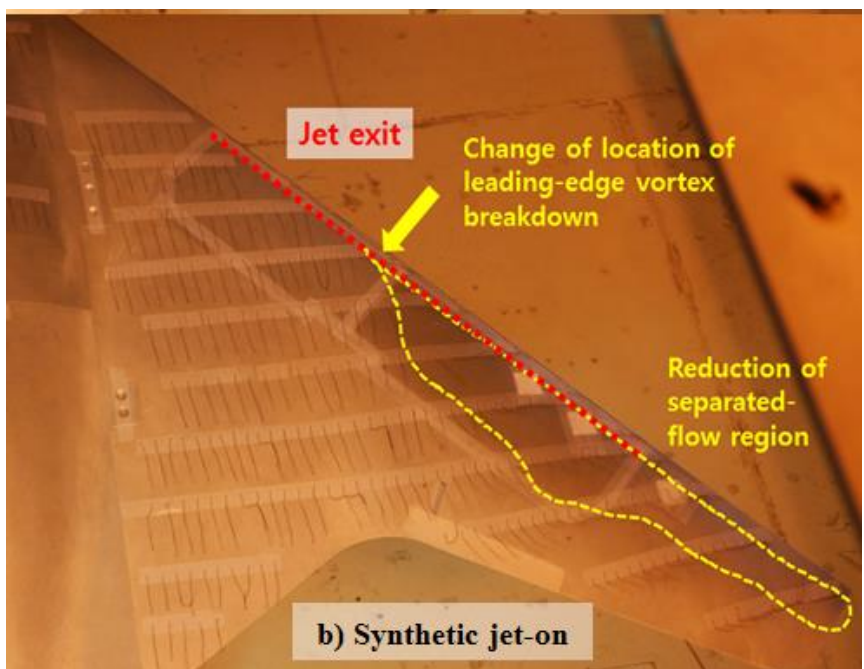
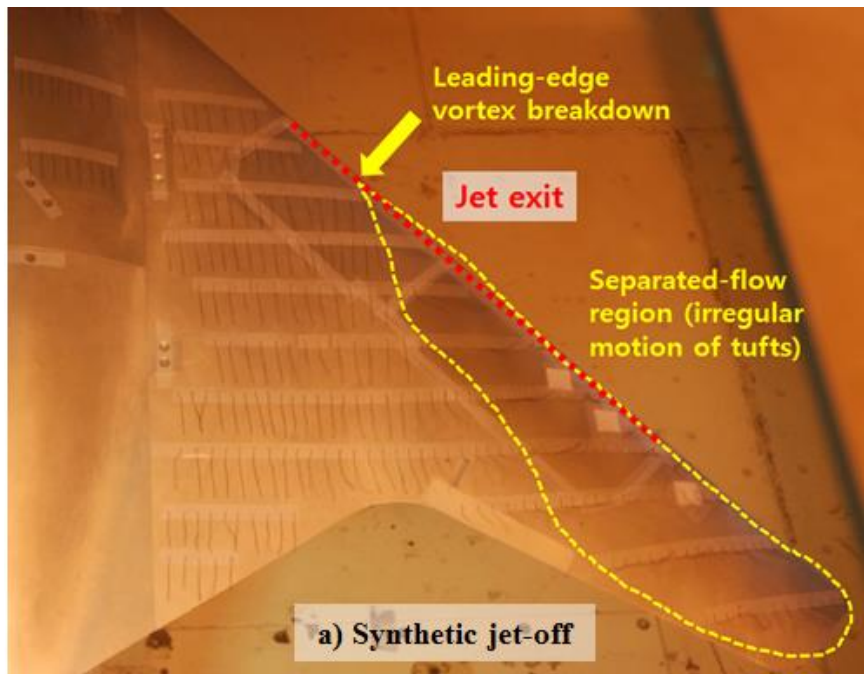


Fig. 4.65 Qualitative effect of synthetic jet ( $\alpha = 12$  degrees)

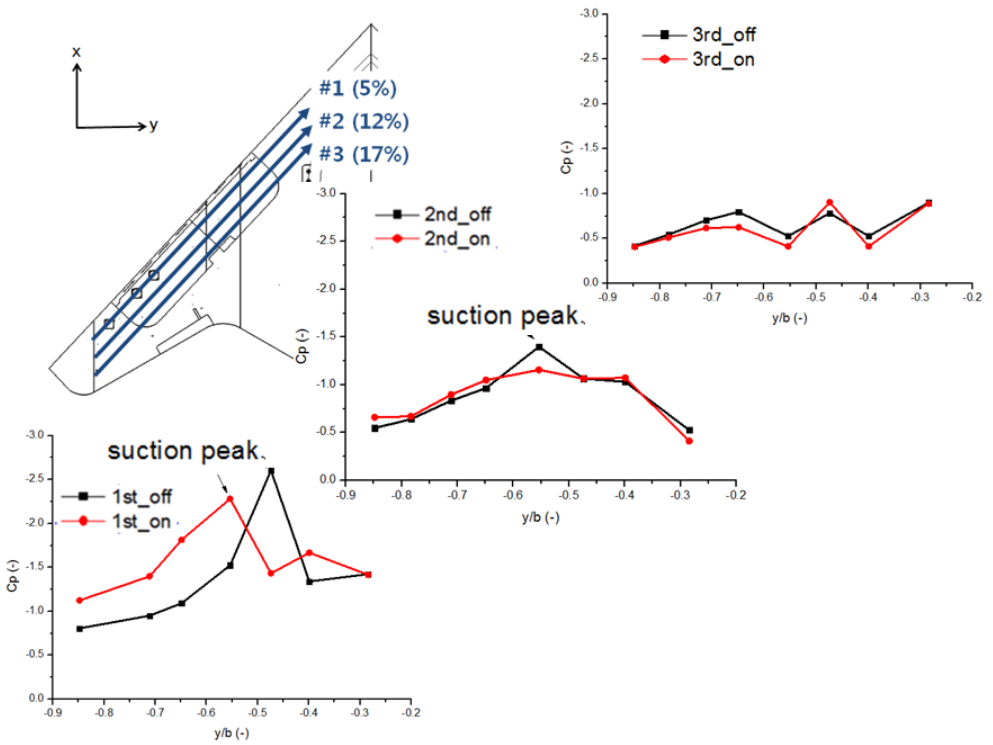
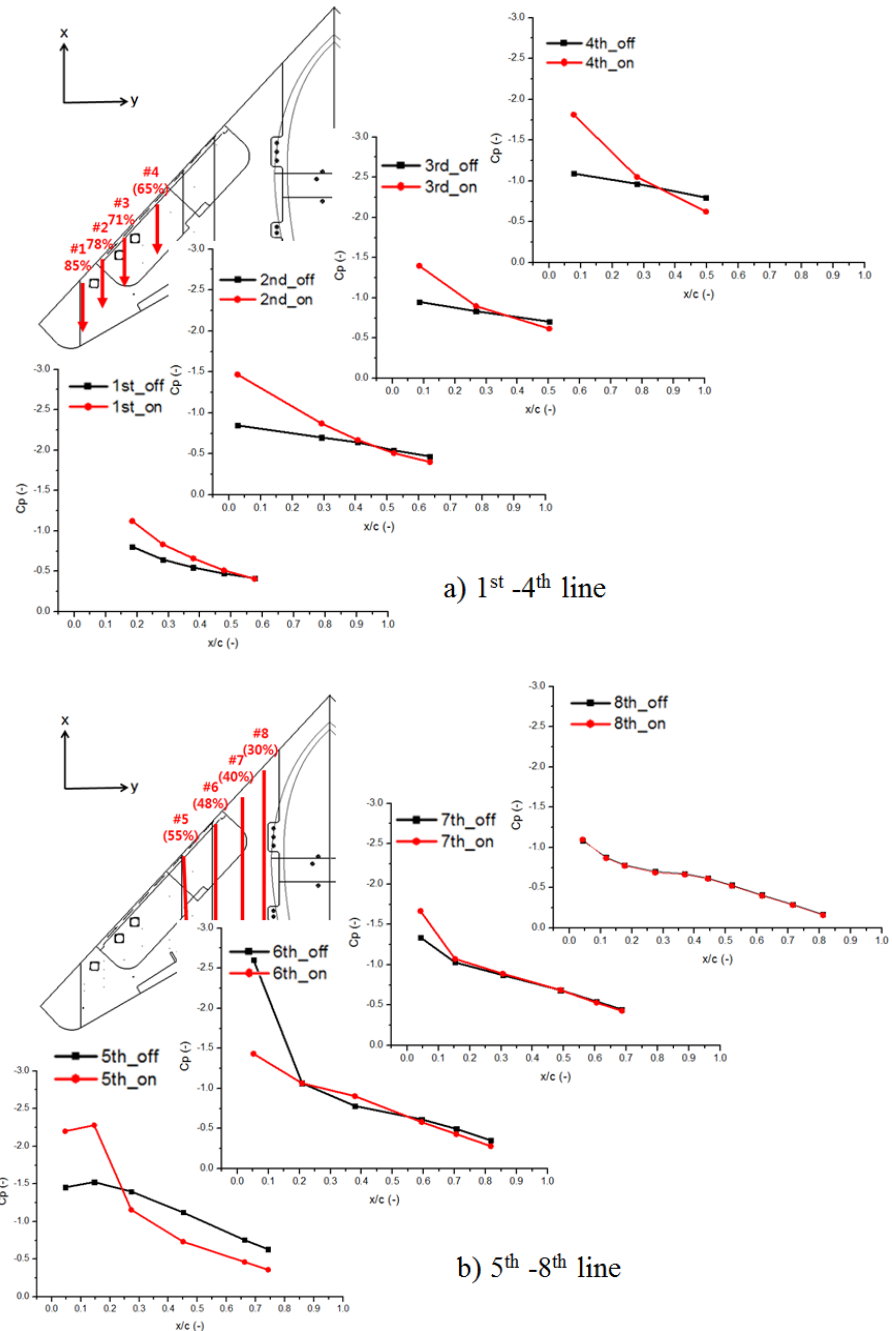


Fig. 4.66 Spanwise  $C_p$  distribution ( $\alpha = 12$  degrees)



**Fig. 4.67 Chordwise  $C_p$  distribution ( $\alpha = 12$  degrees)**

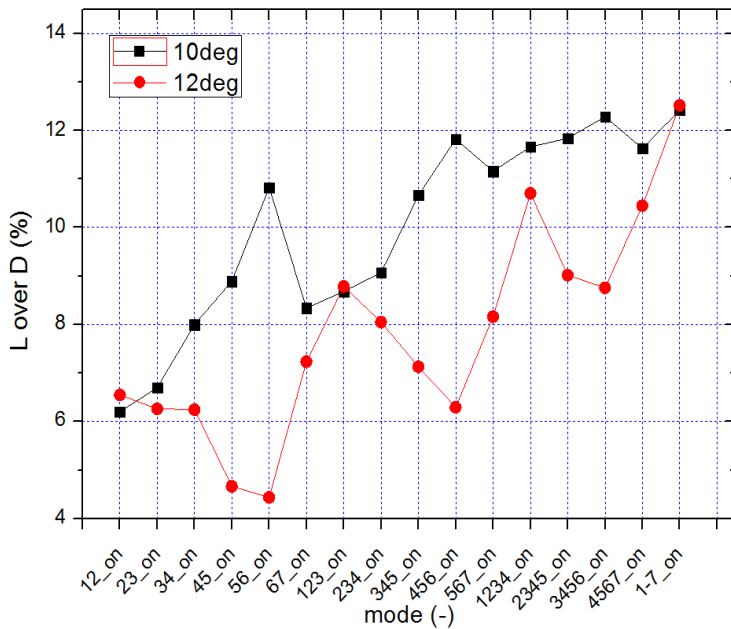


Fig. 4.68 Total increment of  $C/C_d$

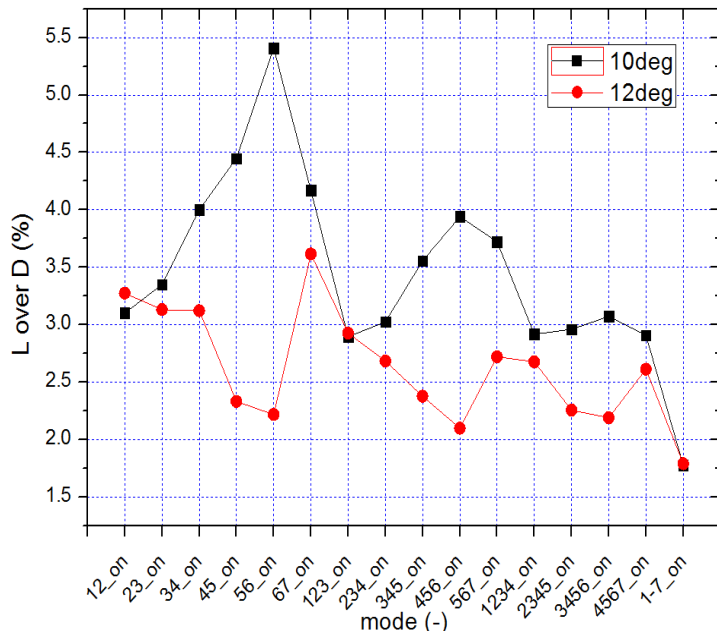
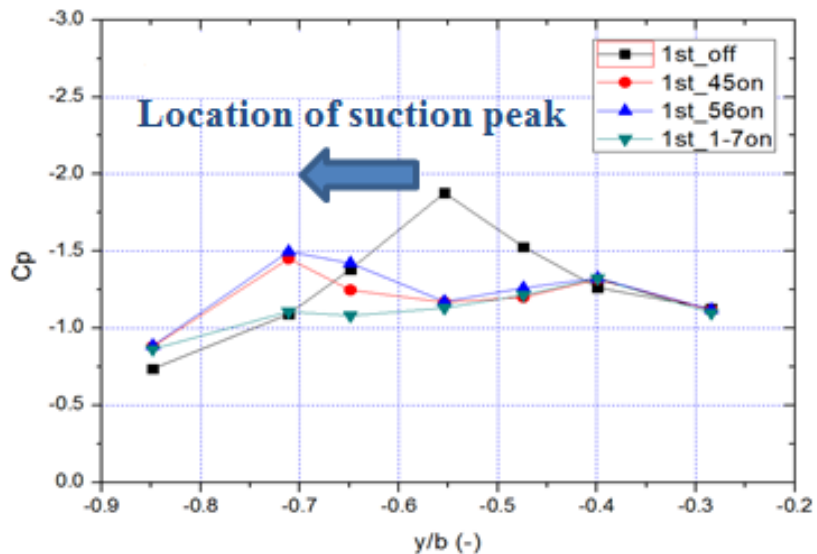
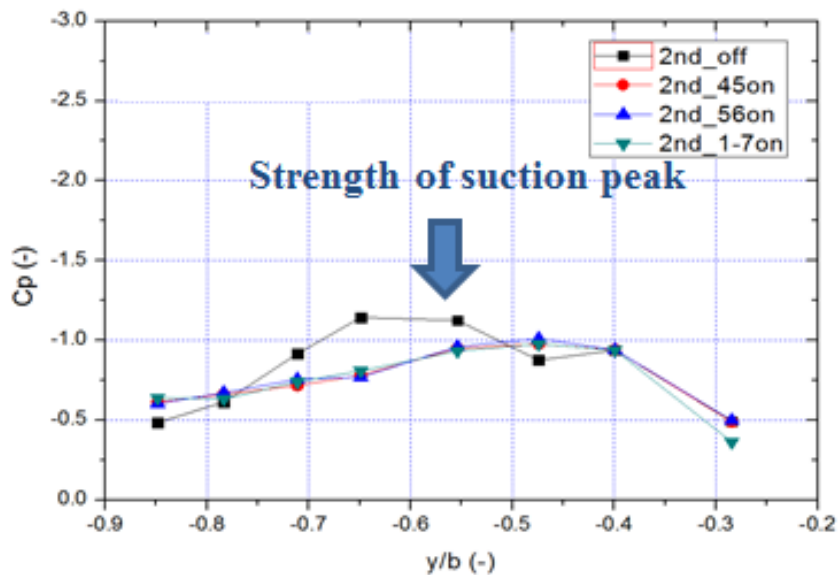


Fig. 4.69 Increment of  $C/C_d$  per module

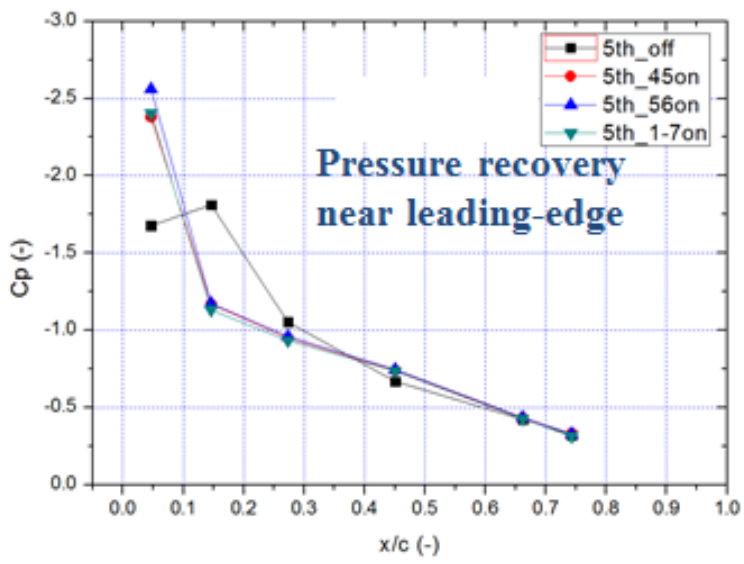


a) 1<sup>st</sup> line

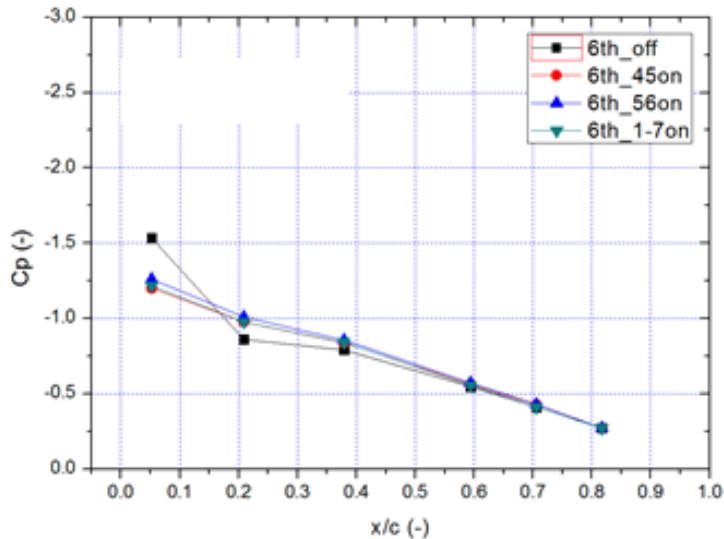


b) 2<sup>nd</sup> line

Fig. 4.70 Spanwise  $C_p$  distribution ( $\alpha = 10$  degrees)

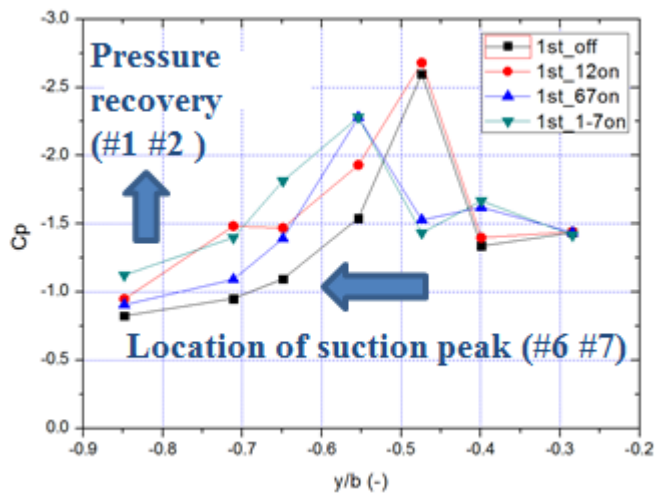


a) 5<sup>st</sup> line

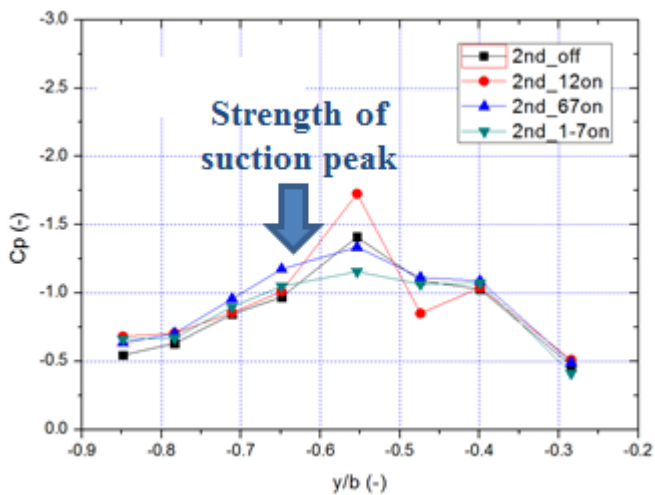


b) 6<sup>th</sup> line

Fig. 4.71 Chordwise  $C_p$  distribution ( $\alpha = 10$  degrees)

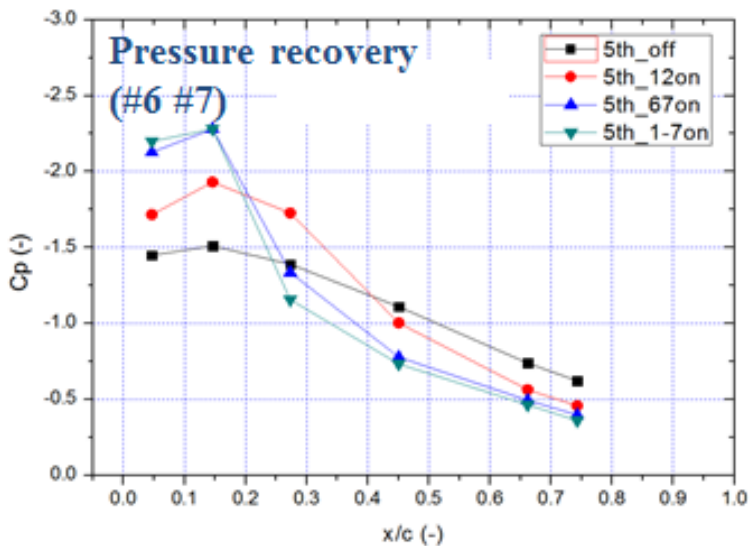


a) 1<sup>st</sup> line

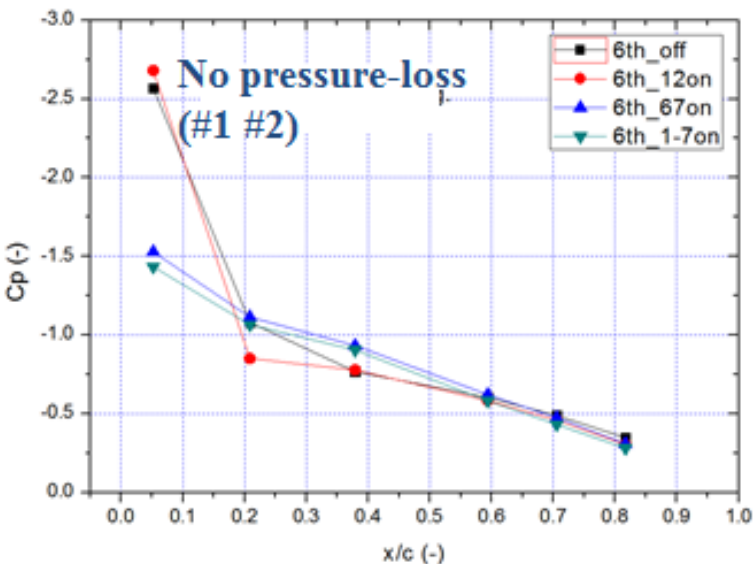


b) 2<sup>nd</sup> line

Fig. 4.72 Spanwise  $C_p$  distribution ( $\alpha = 12$  degrees)



a) 5<sup>st</sup> line



b) 6<sup>th</sup> line

Fig. 4.73 Chordwise  $C_p$  distribution ( $\alpha = 12$  degrees)

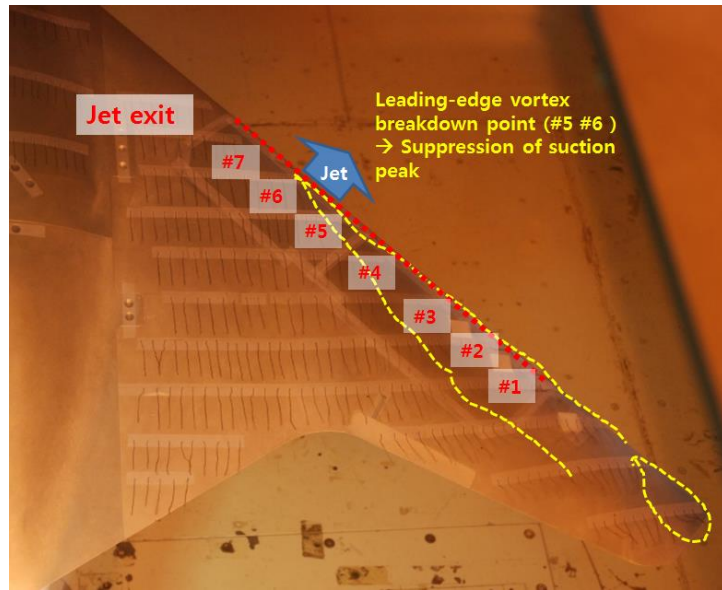


Fig. 4.74 Baseline flow field and synthetic jet location ( $\alpha = 10$  degrees)

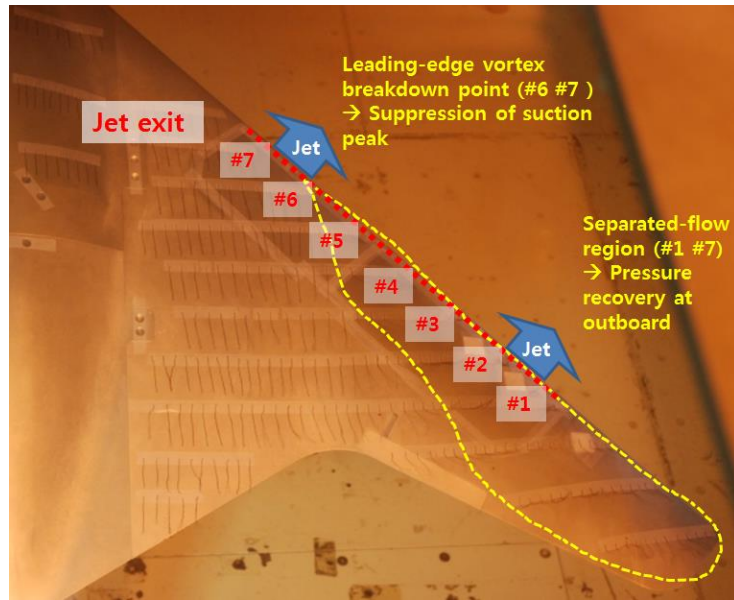


Fig. 4.75 Baseline flow field and synthetic jet location ( $\alpha = 12$  degrees)

**Synthetic jet design methodology**

- Trade-off between jet performance and hardware mass  
→ more efficient synthetic jet system



**Enhanced closed-loop control logic**

- Spanwise and chordwise  $C_p$  distribution (current system: #2 chord line)
- Individual synthetic jet operation according to vortex breakdown location

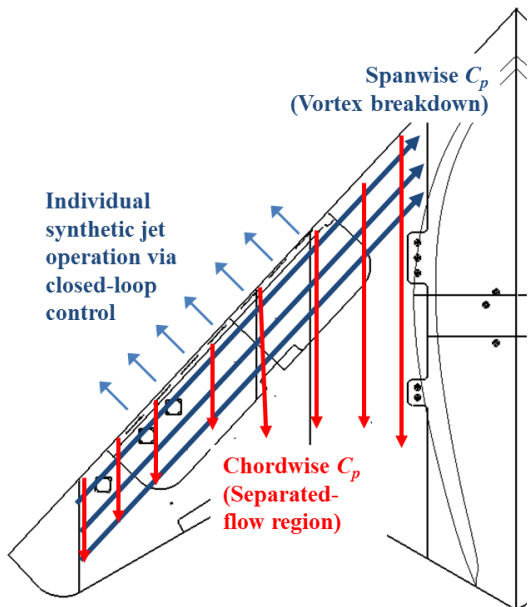


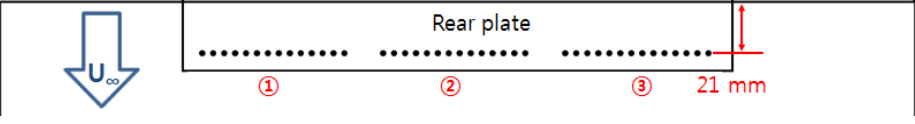
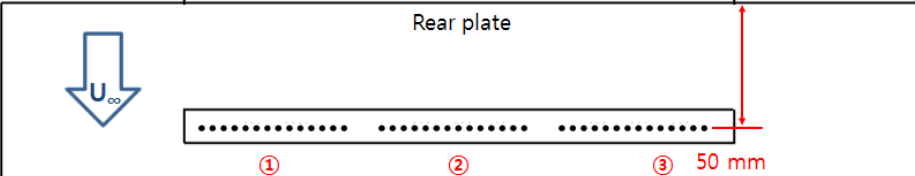
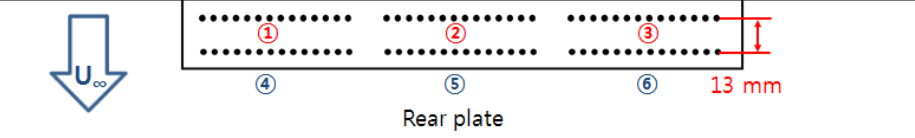
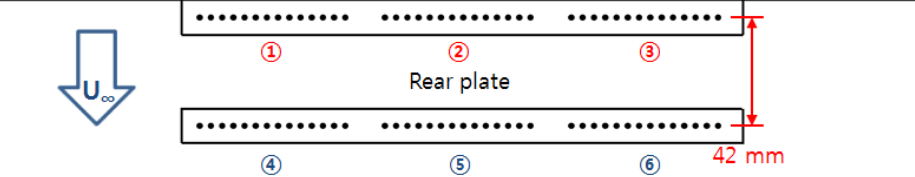
**Fig. 4.76 Possible future research topics**

## Tables

**Table 3.1 Exit configuration and diaphragm actuation mode**

Type	Exit area (mm <sup>2</sup> )	Exit perimeter (mm)	Exit configuration	Mode
1-1	12.57	50.27	 16 holes	Single or dual diaphragm
1-2	12.57	32.99	 7 holes	
1-3	12.57	25.13	 4 holes	
2-1	12.57	32.99	 7 holes	
2-2	12.57	32.99	 7 holes	
2-3	12.57	32.99	 7 holes	
3	25.14	65.98	 14 holes	

**Table 3.2 Types of synthetic jet array**

Type	Synthetic jet array (top view on the rear plate)	Array type
1		Single array
2		Single array
3		Single array
4		Dual array (13mm gap)
5		Dual array (42mm gap)

**Table 3.3 Types of synthetic jet oscillation**

Type	Oscillation phase	Comments
1		<b>Identical phase of all actuators</b>
2		<b>180 degrees phase difference along the chordwise direction</b>
3		<b>180 degrees phase difference along the chordwise and spanwise direction</b>

**Table 4.1 Quantitative comparison of flow control performance**

module	$\alpha = 10$ degrees		$\alpha = 12$ degrees	
	First	Second	First	Second
2	#5#6	#4#5	#6#7	#1#2
3	#4#5#6	#3#4#5	#1#2#3	#5#6#7
4	#3#4#5#6	#2#3#4#5	#1#2#3#4	#4#5#6#7

## References

1. Greenblatt, D. and I.J. Wygnanski, *The control of flow separation by periodic excitation*. Progress in Aerospace Sciences, 2000. **36**(7): p. 487-545.
2. Gad-el-Hak, M. and D.M. Bushnell, *Separation control: review*. Journal of Fluids Engineering, 1991. **113**(1): p. 5-30.
3. Hinze, J.O., *Turbulence* Second edition ed. 1975: McGRAW-HILL.
4. Torenbeek, E. and H. Wittenberg, *Flight Physics: Essentials of Aeronautical Disciplines and Technology, with Historical Notes*. 2009: Springer. 110.
5. Gad-el-Hak, M., *Flow control: passive, active, and reactive flow management*. 1 ed. 2000: Cambridge University Press.
6. Mueller, T.J. and S.M. Batin, *Experimental studies of separation on a two-dimensional airfoil at low Reynolds numbers*. AIAA Journal, 1982. **20**(4): p. 457-463.
7. Mueller, T.J., *The influence of laminar separation and transition on low Reynolds number airfoil hysteresis*. Journal of Aircraft, 1985. **22**(9): p. 763-770.
8. Mane, P., K. Mossi, and R. Bryant, *Experimental design and analysis for piezoelectric circular actuators in flow control applications*. Smart Materials & Structures, 2008. **17**(1).
9. Pollard, A., J.-P. Bonnet, and M. Gad-el-Hak, *Flow control: Current status and future prospects*. Experimental Thermal and Fluid Science, 1998. **16**(1–2): p. 157-164.
10. Tani, I., *Low-speed flows involving bubble separations*. Progress in Aerospace Sciences, 1964. **5**(0): p. 70-103.
11. Gad-el-Hak, M., *Compliant coatings for drag reduction*. Progress in Aerospace Sciences, 2002. **38**(1): p. 77-99.
12. Samaha, M.A., H. Vahedi Tafreshi, and M. Gad-el-Hak, *Effects of hydrostatic pressure on the drag reduction of submerged aerogel-particle coatings*. Colloids and Surfaces A: Physicochemical and Engineering Aspects, 2012. **399**(0): p. 62-70.
13. L, P. *Über Flüssigkeitsbeweugung bei sehr kleinerreibung*. in *Proceedings of Third International Mathematical Congress*. 1904. Heidelberg.
14. HL, D., *Fifty years of boundary layer theory and experiment*. Sciences, 1955: p. 121:375-480.
15. GV, L., *Boundary layer and flow control*. Its principles and application, 1961. **vol. 1**.
16. Schlichting, H. and K. Gersten, *Boundary-layer theory*. 2000: Springer Verlag.

17. MR, H., *History of research on boundary layer control for low drag in UK*. In: Lachmann GV, editor. *Boundary layer and flow control. Its principles and application*, 1961: p. 104-121.
18. Carriere P, E.E., *Theory of flow reattachment by a tangential jet discharging against a strong adverse pressure gradient*. In: Lachmann GV, editor. *Boundary layer and flow control. Its principles and application*, New York: Pergamon Press, 1961. **vol. 1**: p. 209-231.
19. JS., A., *Flow control - the integration of power plant and airframe for future aircraft*. 1952.
20. JS, A., *Design and engineering features of flap blowing installations*. In: Lachmann GV, editor. *Boundary layer and flow control. Its principles and application*, 1961. **vol. 1**(New York: Pergamon Press): p. 463-515.
21. Jabbal, M., S. Liddle, and W. Crowther, *Active flow control systems architectures for civil transport aircraft*. Journal of Aircraft, 2010. **47**(6): p. 1966-1981.
22. Kuchemann, D., *The Aerodynamic Design of Aircraft*. 1978: Pergamon.
23. Faleiro, L., *Beyond the More Electric Aircraft*. Aerospace America, 2005. **Sep.**: p. 35-40.
24. Glezer, A., et al., *Synthetic jet actuator and applications thereof*. 1998, Google Patents.
25. Kim, S. and C. Kim, *Separation control on NACA23012 using synthetic jet*. Aerospace Science and Technology, 2009. **13**: p. 172-182.
26. Gomes, L. and W. Crowther. *Towards a Practical Synthetic Jet Actuator for Industrial Scale Flow Control Applications*. in *IUTAM Symposium on Flow Control and MEMS*. 2008. Springer.
27. Glezer, A. and M. Amitay, *Synthetic jets*. Annual Review of Fluid Mechanics, 2002. **34**(1): p. 503-529.
28. Schubauer, G.B. and H.K. Skramstad, *Laminar-boundary-layer oscillations and transition on a flat plate*. 1948, NATIONAL AERONAUTICS AND SPACE ADMINISTRATION WASHINGTON DC.
29. Seifert, A., et al., *Oscillatory blowing: a tool to delay boundary-layer separation*. AIAA journal, 1993. **31**(11): p. 2052-2060.
30. Glezer, A., *The formation of vortex rings*. Physics of Fluids, 1988. **31**: p. 3532.
31. Amitay, M. and F. Cannelle, *Evolution of finite span synthetic jets*. Physics of Fluids, 2006. **18**: p. 054101.
32. Kim, M., et al., *Flow Control of Tiltrotor Unmanned-Aerial-Vehicle Airfoils Using Synthetic Jets*. JOURNAL OF AIRCRAFT, 2011. **Vol. 48**(No. 3).
33. Amitay, M. and A. Glezer, *Aerodynamic flow control using synthetic jet actuators*, in *Control of Fluid Flow*. 2006, Springer. p. 45-73.
34. Amitay, M., et al., *Aerodynamic flow control over an unconventional airfoil using synthetic jet actuators*. AIAA journal, 2001. **39**(3): p. 361-370.

35. Crook, A., A.M. Sadri, and N.J. Wood, *Development and implementation of synthetic jets for the control of separated flow*. AIAA paper, 1999. **3176**.
36. Bryant, R.G., *LaRC™-SI: a soluble aromatic polyimide*. High Performance Polymers, 1996. **8**(4): p. 607-615.
37. Smith, B.L. and A. Glezer, *The formation and evolution of synthetic jets*. Physics of fluids, 1998. **10**: p. 2281.
38. Gallas, Q., et al., *Optimization of synthetic jet actuators*. 2003: Defense Technical Information Center.
39. Mossi, K. and R. Bryant. *Piezoelectric actuators for synthetic jet applications*. in *MRS Proceedings*. 2003. Cambridge Univ Press.
40. Mossi, K. and R. Bryant, *Pre-stressed Circular Actuators*. Ceramic Transactions, 2003: p. 445-454.
41. Mossi, K., et al., *Boundary condition effects on piezo-synthetic jets*. Integrated Ferroelectrics, 2005. **71**(1): p. 257-266.
42. Zhong, S., et al., *Towards the design of synthetic-jet actuators for full-scale flight conditions - Part 1: The fluid mechanics of synthetic-jet actuators*. Flow Turbulence and Combustion, 2007. **78**(3-4): p. 283-307.
43. Tang, H., et al., *Towards the design of synthetic-jet actuators for full-scale flight conditions - Part 2: Low-dimensional performance prediction models and actuator design method*. Flow Turbulence and Combustion, 2007. **78**(3-4): p. 309-329.
44. Kim, W. and C. Kim, *Separation Control Characteristics of Synthetic Jets Depending on Exit Configuration*. AIAA JOURNAL, 2012. **in press**.
45. Abdou, S. and S. Ziada, *Spanwise Characteristics of High-Aspect-Ratio Synthetic jets*. AIAA JOURNAL, 2006. **44**(7): p. 1516-1523.
46. Oren, L., et al., *Flow Characteristics of Non Circular Synthetic Jets*. 2009, American Institute of Aeronautics and Astronautics, 1801 Alexander Bell Dr., Suite 500 Reston VA 20191-4344 USA.
47. H. Riazi and N.A. Ahmed, *Numerical investigation on two-orifice synthetic jet actuators of varying orifice spacing and diameter*, in *29th AIAA Applied Aerodynamics Conference*. 2011, AIAA: Honolulu, Hawaii.
48. Seifert, A., et al., *Use of piezoelectric actuators for airfoil separation control*. AIAA journal, 1998. **36**(8): p. 1535-1537.
49. Holl, T., B. Gunther, and F. Thiele. *Numerical Investigation of Segmented Actuation Slots for Active Separation Control of a High-Lift Configuration*. in *47th AIAA Aerospace Sciences Meeting Including The New Horizons Forum and Aerospace Exposition*. 2009. Orlando, Florida: AIAA.
50. Ziada, S., *Control of fluid-structure-sound interaction mechanisms by means of synthetic jets*. JSME International Journal Series C, 2003. **46**(3): p. 873-880.
51. Maltby, R., *Flow visualization in wind tunnels using indicators*. 1962, DTIC Document.
52. Seifert, A., A. Darabi, and I. Wyganski, *Delay of airfoil stall by periodic*

- excitation.* Journal of Aircraft, 1996. **33**(4): p. 691-698.
53. Maines, B.H., B.R. Smith, and D. Merrill, *Synthetic Jet Flow Separation Control for Thin Wing Fighter Aircraft*, in *47th AIAA Aerospace Sciences Meeting Including The New Horizons Forum and Aerospace Exposition*. 2009: Orlando, Florida.
54. Liebeck, R., M. Page, and B. Rawdon, *Blended-wing-body subsonic commercial transport*. AIAA paper, 1998. **438**.
55. Roman, D., J. Allen, and R. Liebeck, *Aerodynamic design challenges of the blended-wing-body subsonic transport*. AIAA paper, 2000. **4335**: p. 2000.
56. W, K., *Experimental study on active flow control of synthetic jets depending on exit configuration*. 2011, Seoul National University. p. 20.
57. Jørgensen, F.E., *How to measure turbulence with hot-wire anemometers*. 2002: DANTEC Dynamics.
58. Instrument, N. *NI 625x user manual*. 2009 [cited 2013; Available from: <http://sine.ni.com/nips/cds/view/p/lang/ko/nid/209213>.
59. CORPORATION, D. *9200 Series DDS Function Generator User's Manual* 2009.
60. Instrument, N. *NI myDAQ Device* 2013; Available from: <http://sine.ni.com/nips/cds/view/p/lang/ko/nid/210929>.
61. systems, P. *PZ170E User Manual*. 2011.
62. Systems, P. *Ethernet Intelligent Pressure Scanner, 9116 series*. 2009.
63. Systems, P. *DTC Initium User's manual* 2008.
64. Lee, B., et al., *Separation Control Characteristics of Synthetic Jets with Circular Exit Array*. 2012.
65. Owen, P., L. Klanfer, and A.R.C. LONDON, *On the Laminar Boundary Layer Separation from the Leading-edge of a Thin Aerofoil*. 1953: Defense Technical Information Center.
66. Loftin, L., *Theoretical and experimental data for a number of NACA 6A-series airfoil sections*. 1947.
67. Kim, M., et al., *Flow Control of Tiltrotor Unmanned-Aerial-Vehicle Airfoils Using Synthetic Jets*. Journal of aircraft, 2011. **48**(3): p. 1045-1057.
68. Scholz, P., et al. *Leading-edge Separation Control by Means of Pulsed Jet Actuators*. in *AIAA Flow Control Conference, San Francisco, California*. 2006.
69. Kim, M., B. Lee, and C. Kim. *Computational Study on Flow Control Characteristics of Synthetic Jets over a Blended Wing Body Configuration*. in *2013 Asia-Pacific International Symposium on Aerospace Technology*. 2013. Takamatsu, Japan Japan Society for Aeronautical and Space Sciences (JSASS).
70. Delery, J.M., *Aspects of vortex breakdown*. Progress in Aerospace Sciences, 1994. **30**(1): p. 1-59.
71. Amitay, M. and A. Glezer, *Role of actuation frequency in controlled flow reattachment over a stalled airfoil*. AIAA journal, 2002. **40**(2): p. 209-216.

72. Chaudhari, M., et al., *Frequency response of a synthetic jet cavity*. Experimental Thermal and Fluid Science, 2009. **33**(3): p. 439-448.
73. Chaudhari, M., B. Puranik, and A. Agrawal, *Heat transfer characteristics of synthetic jet impingement cooling*. International Journal of Heat and Mass Transfer, 2010. **53**(5–6): p. 1057-1069.
74. Yang, A.-S., *Design analysis of a piezoelectrically driven synthetic jet actuator*. Smart Materials and Structures, 2009. **18**(12): p. 125004.
75. Zhou, J., H. Tang, and S. Zhong, *Vortex Roll-Up Criterion for Synthetic Jets*. AIAA JOURNAL, 2009. **47**(5): p. 1252-1262.
76. Honami, S. and M. Motosuke. *Vortex Interaction of In-line Synthetic Jets Injected at Different Phase in Low Reynolds Number Cross Flow*. in *6th AIAA Flow Control Conference*. 2012. New Orleans, Louisiana: AIAA.
77. Jabbal, M., *Development of Design Methodology for Synthetic Jet Actuator Array for Flow Separation Control Applications* in *6th AIAA Flow Control Conference*. 2012, AIAA: New Orleans, Louisiana.
78. J. Lee, C. Kim, and K. Kim, *Design of Flapping Airfoil for Optimal Aerodynamic Performance in Low-Reynolds Number Flows*. AIAA Journal, 2006. **Vol. 44**(No. 9): p. pp. 1960-1972.
79. Kral, L.D., et al., *Numerical simulation of synthetic jet actuators*. AIAA paper, 1997. **1824**: p. 1997.
80. Honami, S. and M. Motosuke, *Vortex Interaction of In-line Synthetic Jets Injected at Different Phase in Low Reynolds Number Cross Flow*. 2012.
81. B. L. Smith, M. A. Trautman, and A. Glezer, *Controlled Interactions Synthetic Jets of Adjacent synthetic jet*, in *37th AIAA Aerospace Sciences Meeting and Exhibit 1999*: Reno, NV
82. Holman, R., et al., *Interaction of adjacent synthetic jets in an airfoil separation control application*. AIAA paper, 2003. **3709**.
83. Lee, B., et al., *Closed-loop Active Flow Control of Stall Separation using Synthetic Jets*. 2013.
84. Smith, D.R., et al., *Modification of Lifting body aerodynamics using synthetic jet actuators*. AIAA JOURNAL, 1998. **98-0209**.
85. McCullough, G.B., D.E. Gault, and U.S.N.A.C.f. Aeronautics, *Examples of three representative types of airfoil-section stall at low speed*. 1951: National Advisory Committee for Aeronautics.
86. Sivellis, C., *Experimental and calculated characteristics of three wings of NACA 64-210 and 65-210 airfoil sections*. Technical Note NACA TN, 1947. **1422**.
87. Choi, B., *Effective Model-Free and Model-Based Strategies for Closed-Loop Flow Separation Control*. 2013, Seoul National University.
88. Mitchell, A.M. and J. Délery, *Research into vortex breakdown control*. Progress in Aerospace Sciences, 2001. **37**(4): p. 385-418.
89. Anderson, J.D., *Fundamentals of aerodynamics*. Vol. 2. 2001: McGraw-Hill New York.

90. Lucca-Negro, O. and T. O'doherty, *Vortex breakdown: a review*. Progress in Energy and Combustion Science, 2001. **27**(4): p. 431-481.
91. Benjamin, T.B., *Some developments in the theory of vortex breakdown*. J. Fluid Mech, 1967. **28**(1): p. 65-84.
92. Ringleb, F.O., *Separation control by trapped vortices*. Boundary Layer and Flow Control, 1961. **1**: p. 265-294.

## **Acknowledgments**

This research was supported by Defense Acquisition Program Administration and Agency for Defense Development (UC100031JD). The author also appreciates the administrative help from the Korea Aerospace Research Institute.

## 국문초록

본 논문은 원형 출구 synthetic jet의 유동 제어 특성에 관한 실험적인 연구를 다루고 있다. 원형 출구 배열을 가진 압전소자 구동 방식의 synthetic jet의 특성에 관해 다양한 조건에서 실험을 수행했다. 구동 주파수, 입력 전압, 출구 면적 등을 일정하게 하고 향상된 성능의 원형 출구 배열을 찾기 위해 단계적인 실험을 수행했다. 비교 실험은 정적 유동 조건, 꺾인 평판 위에서 유동 박리 발생 조건, 2차원 에어포일, 3차원 동체-날개 혼합형 모델에서 각각 수행하였다. 정적 유동 조건에서는 열선 유속계를 활용하여 출구 둘레와 구동 주파수에 따른 유동 특성을 비교했다. 꺾인 평판 위에서 유동 박리 발생 조건에서는 출구 직경, 출구 간격, 배열 형태, 구동 위상차를 변화시키면서 표면 압력 계수를 비교했다. 실험 결과는 정적 유동 조건 및 유동 박리 발생 조건에서 수행된 참고논문의 전산 수치 해석 결과와 비교 분석했다. 다양한 실험 결과 비교를 토대로 원형 출구 배열의 성능을 향상시킬 수 있는 핵심 파라미터와 적절한 설계 범위를 도출할 수 있었고, 이와 같은 설계 파라미터를 적용한 synthetic jet을 적용하여 유동 박리 제어 성능이 향상되는 것을 확인할 수 있었다. 향상된 설계 파라미터를 적용한 synthetic jet 시스템은 2차원 에어포일과 3차원 동체-날개 혼합형 모델에 적용하여 유동 박리 제어 성능을 검증했다. 다양한 조건에서 실험 결과를 비교한 결과, 향상된 설계 파라미터를 적용한 synthetic jet 시스템이 실속 조건의 유동 박리를 효과적으로 제어하는 성능을 확인할 수 있었다.

---

**키워드** : Synthetic jet, Active flow control, Circular exit array, Flow separation

**학번** : 2011 – 30789